Humboldt-Universität zu Berlin

DISSERTATION

Ultrafast Two-Dimensional Infrared Spectroscopy of Hydrogen-bonded Base Pairs and Hydrated DNA

zur Erlangung des akademischen Grades doctor rerum naturalium (Dr. rer. nat.)

Mathematisch-Naturwissenschaftlichen Fakultät I

Ming Yang

Dekan: Prof. Stefan Hecht PhD

Gutachter/in: 1. Prof. Dr. Thomas Elsaesser

2. Prof. Dr. Oliver Benson

3. Prof. Dr. Sundstrom

Datum der Einreichung: 05.04.2012

Datum der Promotion: 18.07.2012

Zusammenfassung

Die Struktur von DNS Molekülen und ihre Wechselwirkung mit Wasser werden seit langer Zeit heiß diskutiert. In der vorliegenden Arbeit wird nichtlineare Spektroskopie zur Untersuchung dieser Systeme angewendet.

Oligomere, die aus 23 alternierenden Adenin-Thymin-Basenpaaren bestehen und eine Doppelhelix bilden, wurden mit Hilfe von 2D IR Spektroskopie für verschiedene Hydratisierungsgrade untersucht. Für DNS-Filme bei 0% relativer Feuchte (r.F.) erlauben die transienten Spektren eine Unterscheidung der NH Streckschwingung von Thymin (ν(NH)), der symmetrischen und asymmetrischen NH_2 Streckschwingung von Adenin ($\nu_s(NH_2)$ and $\nu_a(NH_2)$) sowie die Bestimmung der jeweiligen Linienprofile. Die Spektren zeigen eine homogene Verbreiterung für die $\nu(NH_T)$ wohingegen die $\nu_s(NH_2)$ and $\nu_a(NH_2)$ eine ausgeprägte und zeitunabhängige inhomogene Verbreiterung zeigen, welche auf Unordnungen in der DNS-Struktur hinweisen. Außerdem kann Energietransfer von der $\nu_a(NH_2)$ zur ν(NH) beobachtet werden. Bei Erhöhung der r.F. hat die erhöhte Anzahl von Wassermolekülen nur einen geringen Einfluss auf die Positionen und Linienprofile der NH Streckschwingungen. Dadurch wird nahegelegt, dass die spektrale Dynamik vom DNS Molekül selbst und nicht vom umgebenen Wasser bestimmt ist. Im Gegensatz dazu zeigt die OH Streckmode der Wasserhülle um die DNS spektrale Diffusion auf einer 500 fs Zeitskala.

Guanosin-Cytidin(GC)-Basenpaare wurden in Chloroformlösung untersucht, um die Wechselwirkung zwischen Basenpaaren zu verstehen. Dabei wurden die NH Schwingungen in einer local mode Darstellung betrachtet, die zwei freie NH Gruppen von G und C und drei wasserstoffverbrückte NH Gruppen beeinhaltet. Die Kopplungen und Relaxationsdynamik der NH Streckanregungen wurden mit Femtosekunden-Pump-Probe und 2D IR Experimenten studiert. Die Ergebnisse zeigen eine Verringerung der Lebensdauer mit der Bildung von Wasserstoffbrücken sowie Energietransfer zwischen zwei wasserstoffverbrückten NH Streckschwingungen.

Schlagwörter: 2D IR Spektroskopie, hydratisierte DNS, Wasserstoffbrücken, Basenpaare in Lösung

Abstract

The structure of DNA molecule and the interactions with its surrounding water is a hot topic for long time. In this thesis, we employ the nonlinear spectroscopy, including femtosecond pump-probe and two-dimensional infrared (2D IR) experiment, to study the vibrational dynamics of the systems.

Double-stranded DNA short oligomers containing 23 alternating adenine-thymine base pairs were studied at different hydration levels by femtosecond 2D IR spectroscopy. For a DNA film at 0% relative humidity, the transient spectra enable a separation of the NH stretching mode of thymine from the symmetric and asymmetric NH_2 stretching modes of adenine and determine the individual line shapes. For the NH stretch of thymine, the spectra demonstrate an essential homogeneous broadening, whereas for the symmetric and asymmetric NH_2 stretches a pronounced and time-independent inhomogeneous broadening suggests a disorder in DNA structure. An energy transfer from the asymmetric NH_2 stretch of adenine to the NH stretch of thymine is also observed. When the relative humidity increases, the increased water molecules have limited influence on the positions and line shapes of NH stretching frequencies, suggesting the spectral dynamics governed by DNA rather than water fluctuations. In contrast, the OH stretching mode of water shell around hydrated DNA undergoes a spectral diffusion on a 500 fs time scale, which is slower than the neat water.

The guanosine-cytidine (GC) base pairs in chloroform solution were investigated to understand the interactions within base pairs. A local mode representationof NH stretching mode is adopted, consisting two free NH groups of G and C and three hydrogen bonded NH groups. The coupling and relaxation dynamics of the NH stretching excitations are studied by femtosecond pump-probe and 2D IR experiments. The results demonstrate a lifetime shortening upon the formation of hydrogen bonds, and an energy transfer between two hydrogen-bonded NH stretches.

Keyword: 2D IR spectroscopy, hydrated DNA, hydrogen bonds, base pairs in solution

Contents

1 Introduction

1.1 Hydrogen Bonds

Hydrogen bonding is one of the fundamental types of chemical bonding and exists widely in the nature. A hydrogen bond involves two groups, A−H and B, consisting of three atoms A, B and H, where H is the hydrogen atom and A, B are usually electronegative atoms like fluorine, nitrogen or oxygen. The hydrogen bond occurs when H and B atoms attracted to each other, and the distance between them becomes less than the van der Waals radii of H and B atoms in isolation [1]. This interaction is first of all an electrostatic attraction of two groups; moreover, the shortened distance between H and B is often accompanied by an increasing role of the covalent character [2-6] due to the charge density changes. Usually, a hydrogen-bonded system is denoted as A−H···B, where the "···" represents the hydrogen bond. The A−H group is referred to as the donor group as it 'donates' the hydrogen atom, and B is referred to as the acceptor group because it 'accepts' the hydrogen atom. A hydrogen bond is weaker than covalent bonds and stronger than van der Waals interactions. The energy of hydrogen bonds varies in the 1-50 kJ/mol range, depending on the local geometry as well as the type and strength of interaction between the acceptor and donor groups [2]. This interaction is strong enough to determine the structure of many molecular systems, such as water, ice [3] and macromolecule systems such as deoxyribonucleic acid (DNA) [4] and proteins. On the other hand, it is weak enough to be broken and re-formed when necessary, giving the system some structural flexibility related to its function, e.g. for the replication of DNA [5].

One interesting and extremely important example of a hydrogen-bonded system in nature is water [6, 7]. Each water molecule can form up to four hydrogen bonds with neighboring water molecues, by donating and accepting two hydrogen atoms (Figure 1-1 left). This ability is responsible for the abnormally high melting point, compared to other hydrides of group VI elements, and for the tetrahedral geometry of each water molecule in normal ice [8] (Figure 1-1 right), a structure that tends to persist also in the liquid. In the liquid state, in comparison, one water molecule participates on average in 3.5 hydrogen bonds [9]. In order to form the four hydrogen bonds in ice, the water molecules are less capable in packing themselves in such an efficient way, thereby reducing the number of closest neighbors from 12 to 4, giving a peak density at 4ºC instead of continuously increasing with decreasing temperature like most other liquids. This decrease in density when water is frozen to ice is responsible for making

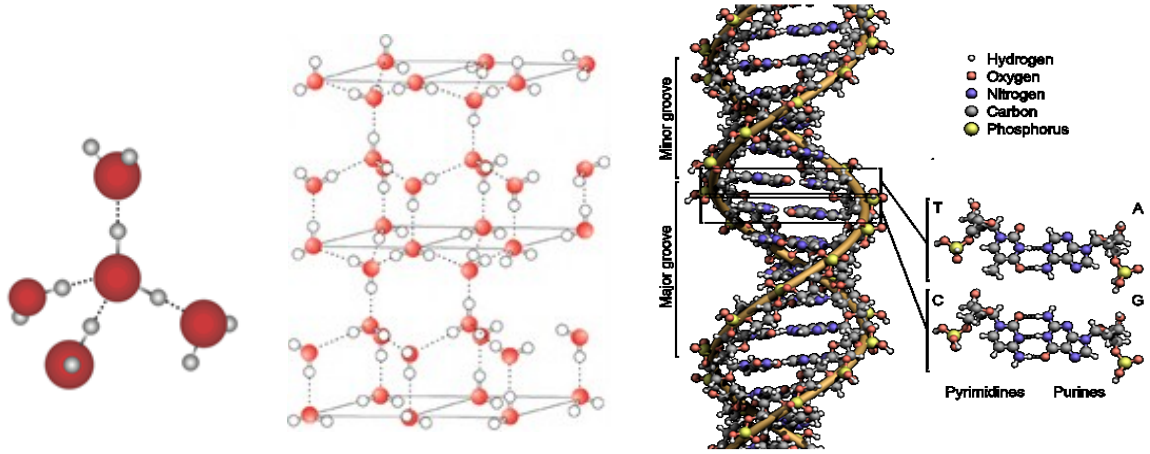

Figure 1-1: Illustration of tetrahedral arrangement of hydrogen bonds between water molecules (left) and crystallized ice with tetrahedral geometry (middle). Structure of DNA double helix (right) and Watson-crick geometry of two kinds of nucleobase pairs taken from (wiki)

ice float on the surface of water and preventing the water underneath from being frozen; thus aquatic lives are also protected from being frozen and are able to survive under the protection of the ice cover during extremely cold weather. Consequently, water, with its anomaly, is extremely important for lives to flourish on Earth.

Hydrogen bonds play a key role for the structure and function of many biomolecules, such as DNA (Figure 1-1 right). DNA has the structure of a double helix [4, 10]. It is composed of two long strands of simple units called nucleotides. A nucleotide contains segments of backbone which hold the chain together, and the nucleobase which forms hydrogen bonds with the nucleobase in the other strand of the helix. The nucleobase pairs in Watson-Crick geometry in the double helix contain two or three hydrogen bonds depending on the type of the nucleobase pair, and make the structure rather rigid. Surrounding water molecules are also bound to DNA through hydrogen bonds. These water molecules are important in maintaining the tertiary structure of DNA, for example A-DNA or B-DNA [11, 12]. However, when DNA replication is started, the DNA double strand helix unwinds itself and separates into two single strands by breaking all hydrogen bonds in between. Each single strand serves as a template and recreates a complementary sequence by forming hydrogen bonds with free nucleotides in the solution, thus forming a duplication of the original strand. This process, which is a critical pre-condition for life, is only possible due to the flexibility of structure brought about by the moderate strength of hydrogen bonds.

In the last few decades, people have devoted much time and effort to understanding hydrogen bonded systems and remarkable progress has been achieved. Employing x-ray diffraction,

neutron diffraction, nuclear magnetic resonance (NMR) and other techniques, the positions of atoms and interactions between atoms have been studied and the structures of macromolecular systems have been derived. However, these techniques, except for NMR, give mostly time averaged results and provide no information about the time evolution or non-equilibrium properties of hydrogen-bonded systems, while the NMR gives a time resolution of the order of picoseconds or longer. In order to properly understand the functioning of hydrogen bonded systems, it is also important to understand the dynamics of hydrogen bonds, for example the energy flow and proton transfer which occurs on sub-picosecond to nanosecond timescale.

1.2 Vibrational Spectroscopy and Hydrogen Bonds

Vibrational spectroscopy has been an important tool in understanding hydrogen bonded systems since the 1930's [13-15]. Using vibrational spectroscopy to study local excitations of hydrogen bonded systems, insight can be gained into local interactions and microscopic dynamics. Based on the frequency position of the stretching vibration of the hydrogen donor group A-H, a classification of hydrogen bonds has been derived. In general, the attractive interaction between A-H and B leads to a redshift of the stretching frequency, compared to a free A-H group. The following scheme applies to O-H···O bonds:

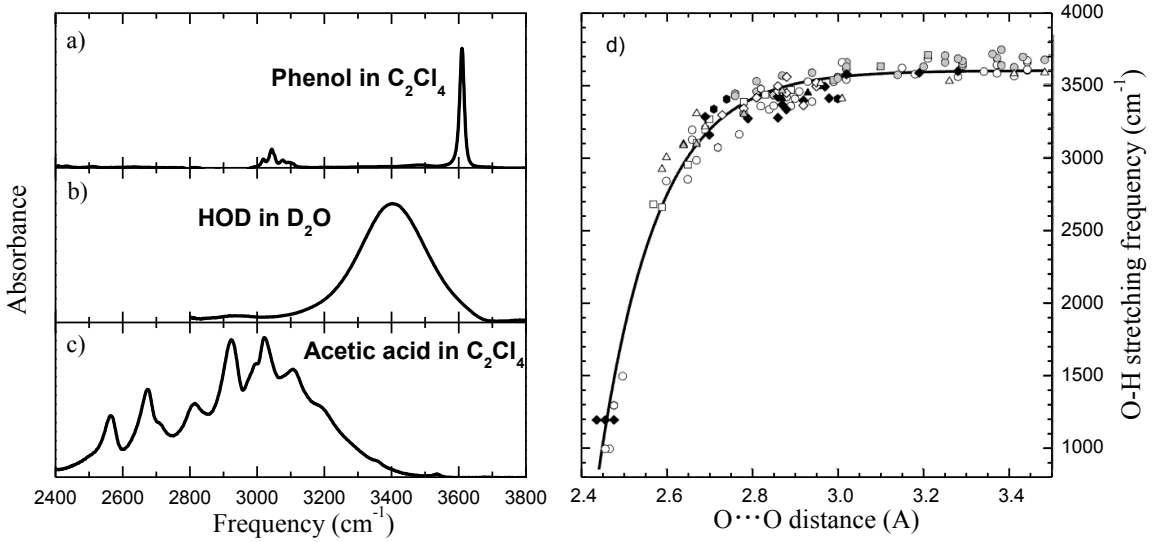

Figure 1-2: Infrared absorption spectra of OH stretching of (a) the free OH group of phenol in C_2Cl_4; (b) weak hydrogen bonded OH of HOD in D_2O; (c) Medium-strong hydrogen bonded OH of cyclic acetic acid dimer in C_2Cl_4. d) Empirical relation between O-H stretching frequency and O···O distance in O−H···O system taken from Ref. (13) . The symbols are the absorption peak of various compounds in solid state. The empirical relation is shown as solid line.

a) Weak hydrogen bonds. When the O···O distance is between 2.8 and 3.0 Å, hydrogen bonds are considered being weak. The best known, and most widely studied, example of a weak hydrogen bonded system is water. The absorption of the OH stretching mode of HOD in D_2O (Figure 1-2(b)) is red-shifted and broadened compared to the stretching mode of free OH of phenol in C_2Cl_4 (Figure 1-2 (a)). For a weak hydrogen bonded system, the red shift is about 100-300 cm^{-1} and the Full Width of Half Maximum (FWHM) of the band is of the order of 200-600 cm^{-1}.

b) Medium-strong hydrogen bonds. Hydrogen bonds are considered medium-strong when the O···O distance is between 2.6 and 2.8 Å. The cyclic acetic acid dimer in C_2Cl_4 (Figure 1-2 (c)) is a representative example. In this situation, the red-shift increases to 300-1000 cm^{-1} and the FWHM of the band is of the order of 1000 cm^{-1}. Moreover, there appears a fine structure of the absorption band.

c) When the O···O distance decreases to be less than 2.6 Å, hydrogen bonds are regarded as strong. The mechanisms involved are beyond the scope of this thesis.

The red-shift of the band is mostly due to a reduction of the force constant of the A-H stretching oscillator and an increase of the anharmonicity of the potential energy surface along the stretching coordinate (Figure 1-3 left). When a hydrogen bond is formed, the acceptor group approaches the donor group and lowers the energy of the ν=1 state of the stretching oscillator, therefore causing a red-shift of the ν=0→1 vibrational transition. The shortening of the distance between two groups is proportional to the increase of the anharmonicity of the oscillator, thus being indicated by the red-shift of the oscillating frequency. The relation between the O···O distance and vibrational frequency has been identified empirically for solid

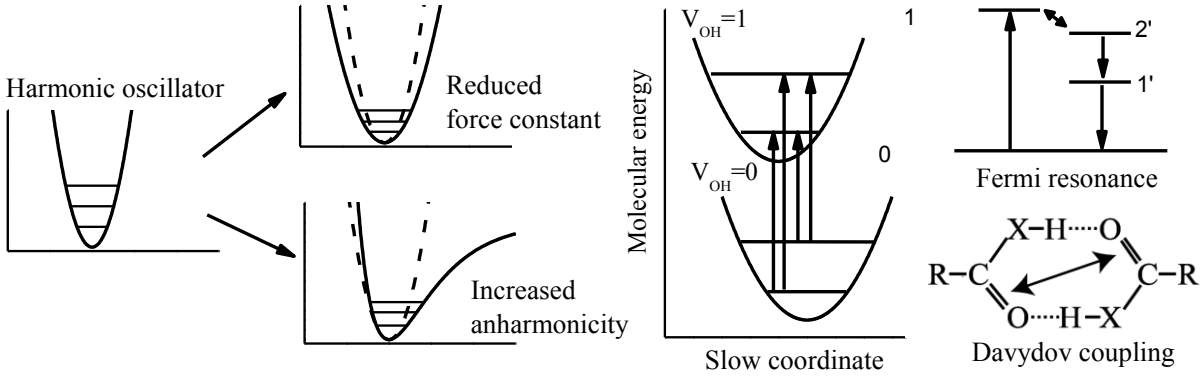

Figure 1-3: Consequences of hydrogen bonding: red-shift because of reduction of force constant and increased anharmonicity (left), Frank-Condon progressions (center), Fermi resonance (top right) and Davydov coupling (bottom right).

state systems with different O···O distances [13-16], as shown in Figure 1-2 (d). It shows an observable red-shift when the O···O distance is less than 3 Å, above which the trend is almost flat, i.e., there is no significant red-shift. However, this relation cannot be applied to liquids with a strong fluctuating hydrogen bond structure. For example, MD simulations of water and HOD in D_2O show that the OH stretching frequency is also affected by the angle of bending hydrogen bonds [17].

The strong broadening of the fundamental stretching transition is mainly attributed to the following mechanisms, (i) solvent-solute interaction leads to a faster dephasing and results in spectral broadening; (ii) coupling between the OH stretching mode at high frequency and hydrogen bond modes at low frequencies leads to a Frank-Condon progression which displays a line separation of the high frequency mode by one individual quanta of the low frequency mode (Figure 1-3 middle); (iii) the inhomogeneous distribution of hydrogen bonds, especially in liquids, also leads to a distribution in frequency in order of several hundreds of wavenumbers, (iv) Fermi resonances between the ν_{OH}=1 state and overtones or combination tones of modes at lower frequencies cause an additional splitting of the OH stretching mode in order of several tens of wavenumbers and provides an extra energy relaxation pathway (Figure 1-3 top right); (v) Davydov coupling between different resonant oscillators in a system with multi hydrogen bonds leads to additional splitting in order of a few wavenumbers (Figure 1-3 bottom right). The latter two mechanisms contribute mainly to the fine-structure appearing in medium strong hydrogen bonded system.

As shown above, dynamics of the hydrogen-bonded system are reflected in the lineshapes of steady-state absorption. However, calculation of the mechanisms (i) to (v), which are of similar relevance for the overall lineshape, makes an analysis of dynamics impractical. Therefore, ultrafast spectroscopy, a combination of both time and frequency domain spectroscopic techniques, is a useful tool to study the dynamics of hydrogen bonded systems. Ultrafast spectroscopy addresses the nonlinear response of the system in the time domain at a time scale between a few femtoseconds and tens of picoseconds. In particular, ultrafast nonlinear 2D Fourier-transform Infrared (FTIR) spectroscopy allows for a possibility to figure out whether the inhomogeneous or homogeneous broadening is dominating, and is able to map coupling or energy transfer between different oscillators.

In this thesis, 2D FTIR spectroscopy is employed to investigate hydrogen bond dynamics in base pairs, both in solution as well as in films consisting of artificial DNA oligomers. We will

first introduce the theoretical background of the methods applied in chapter 2, followed by a description of our experimental setups and data analysis methods in chapter 3. In chapter 4, results for a short oligomer containing alternating adenine-thymine (AT) at different humidity levels will be discussed. Then results and discussion on the Guanosine-Cytidine (GC) base pair in $CHCl_3$ are presented in chapter 5. Finally, this thesis ends with a summary and outlook chapter.

2. Theory of Nonlinear Spectroscopy

For decades, optical spectroscopy has been proven to be a useful tool in studying matter and its interactions. Together with the invention and development of the laser, nonlinear interactions between intense laser pulses and matter started the new era of nonlinear spectroscopy. In this section, principles of nonlinear spectroscopy applied in my work are introduced.

2.1 Nonlinear Polarization and Density Matrix Formalism

When the incident light field **E**(**r**,t) interacts with matter, a polarization **P**(**r**,t) is generated. In general, **P**(**r**,t) depends in a nonlinear fashion on **E**(**r**,t). This behavior is frequently approximated as a power expansion:

$$\begin{aligned}\mathbf{P}(\mathrm{r},\mathrm{t}) &= \mathbf{P}^{(1)}(\mathbf{r},t) + \mathbf{P}^{(1)}(\mathbf{r},t) + \mathbf{P}^{(1)}(\mathbf{r},t) + \cdots \\ &= \chi^{(1)} \cdot \mathbf{E}(\mathbf{r},t) + \chi^{(2)} : \mathbf{E}(\mathbf{r},t)\mathbf{E}(\mathbf{r},t) + \chi^{(3)} : \mathbf{E}(\mathbf{r},t)\mathbf{E}(\mathbf{r},t)\mathbf{E}(\mathbf{r},t)\end{aligned} \tag{2.1}$$

where $\mathbf{P}^{(n)}$ are the n^{th} order polarizations, and $\chi^{(n)}$ are the n^{th} order susceptibility tensors. Then, the polarization becomes the source of the electromagnetic field which is the signal been measured, and it is given by

$$E_s(t) \propto \dot{P}(t) \tag{2.2}$$

In quantum mechanics, the macroscopic polarization is given by the expectation value of the dipole operator μ. For a statistical ensemble, the system's state is often described with density matrix ρ(t), defined as a matrix describing the ensemble average over each possible state of the system. The polarization in the time domain is thus given by

$$P(t) = Tr(\mu(t)\rho(t) = < \mu(t)\rho(t) > \tag{2.3}$$

The temporal evolution of the system can be described in terms of the density matrix $\rho(t)$ which obeys the Liouville-Von Neumann equation:

$$\frac{d}{dt}\rho(t) = -\frac{i}{\hbar}[H, \rho(t)] \tag{2.4}$$

Here H is the Hamiltonian of the system. If we assume the external electromagnetic field is a weak perturbation, then H can be regarded as the sum of Halmiltonian of the unperturbed system H_0 and the time-dependent perturbation H_I(t). In the interaction picture, the Liouville-Von Neumann equation can be written as [18]

$$\frac{d}{dt}\rho_I(t) = -\frac{i}{\hbar}[H_I(t), \rho_I(t)] \tag{2.5}$$

This equation can be solved iteratively by plugging it into itself. For n iterations at times τ_n, it can be expanded as

$$\rho_I(t) = \rho_I(t_0) + \sum_{n=1}^{\infty}\left(-\frac{i}{\hbar}\right)^n \int_{t_0}^{t} d\tau_n \int_{t_0}^{\tau_n} d\tau_{n-1} \dots \int_{t_0}^{\tau_2} d\tau_1 \left[H_I(\tau_n), \left[H_I(\tau_{n-1}), \dots [H_I(\tau_1), \rho_I(t_0)]\right]\right] \tag{2.6}$$

In the systems studied here, the interaction between electromagnetic field and matter is approximated by the electric dipole interaction. The interaction here is brought by an optical light field, thus the Hamiltonian of interaction is given by

$$H_I(t) = -\mu E(t) \tag{2.7}$$

Therefore, by inserting the equation(2.7) into equation(2.6), we get

$$\rho(t) = \rho(t_0) + \sum_{n=1}^{\infty}\left(-\frac{i}{\hbar}\right)^n \int_{t_0}^{t} d\tau_n \int_{t_0}^{\tau_n} d\tau_{n-1} \dots \int_{t_0}^{\tau_2} d\tau_1 E_1 E_1 \dots E_1 \left[\mu(\tau_n), \left[\mu(\tau_{n-1}), \dots [\mu(\tau_1), \rho_I(t_0)]\right]\right] \tag{2.8}$$

Combining this with equation(2.3), the nth order of polarization is given by

$$P^{(n)}(t) = \langle \mu(t) \left(\frac{i}{\hbar}\right)^n \int_{t_0}^{t} d\tau_n \int_{t_0}^{\tau_n} d\tau_{n-1} \dots \int_{t_0}^{\tau_2} d\tau_1 E_1 E_1 \dots E_1 \left[\mu(\tau_n), \left[\mu(\tau_{n-1}), \dots [\mu(\tau_1), \rho(t_0)]\right]\right] \rangle$$
$$= \left(\frac{i}{\hbar}\right)^n \int_{t_0}^{t} d\tau_n \int_{t_0}^{\tau_n} d\tau_{n-1} \dots \int_{t_0}^{\tau_2} d\tau_1 E_1 E_1 \dots E_1 \langle \mu(t) \left[\mu(\tau_n), \left[\mu(\tau_{n-1}), \dots [\mu(\tau_1), \rho(t_0)]\right]\right] \rangle \tag{2.9}$$

Apart from the external fields E_1, E_2 and so on, the rest of the equation depends on the properties of the quantum system. Thus assuming the system is in equilibrium before the interaction hence t_0=-∞ and τ_1=0, the nonlinear response function of the system can be described as

$$S^{(n)}(\tau_1, \tau_2, \dots, \tau_{n-1}, t)$$
$$= \left(\frac{i}{\hbar}\right)^n \Theta(\tau_1)\Theta(\tau_2) \dots \Theta(\tau_{n-1}) \langle \mu(t) \left[\mu(\tau_{n-1}), \left[\mu(\tau_{n-2}), \dots [\mu(0), \rho(-\infty)]\right]\right]\rangle$$
$$= \left(\frac{i}{\hbar}\right)^n \Theta(\tau_1)\Theta(\tau_2) \dots \Theta(\tau_{n-1}) \sum_{i=1}^{2^n} R_i \qquad (2.10)$$

The functions $\Theta(\tau_n)$ enforces the time ordering of the interactions to be $\tau_1<\tau_2<...<\tau_{n-1}<\tau_n<t$. Due to the n times commuters in the response function, the expansion of equation(2.10) results to a sum of 2^n real tensors, which are represented by the response function R_i and correspond to all possible combination of interactions from left or right side.

2.2 Double-sided Feynman Diagrams

For the sake of explicitness, each of the 2^n different parts of the response function (2.10) can be represented by double-sided Feynman diagrams as Liouville space pathways, shown in Figure 2-1.

The state of the system is denoted with the density matrix. It starts in an equilibrium state |a><a| at the bottom of the diagram (the signs of bra and ket are often omitted). Time runs

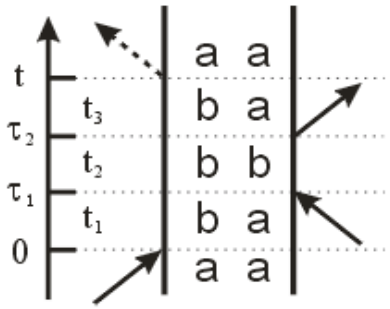

Figure 2-1: Double-sided Feynman diagram of one n^{th} order Liouville space pathway. The interactions occur at different moment. The moments of interactions with incident photons are denoted as τ_n t and the moment of emission of the signal is denoted as t. The time intervals between interactions are denoted as t_n. The states of the 2-level system are |a> and |b>, with |b> having higher energy than |a>.

from the bottom to the top, and the vertical lines represent the time evolution of the bra and ket of the density matrix. The solid arrows indicate the interactions of the system with the external electromagnetic fields. The arrow pointing toward the diagrams means an increase in the quantum number of the ket or bra, while the arrow pointing away from the diagrams means the opposite. The arrow pointing to the right represents a complex field interaction with phase $e^{-i\omega t+kr}$ while the arrow pointing to the left represents the complex conjugate. Each direction represents a rotating frame direction of the pulse, which is resonant with the bra or ket of the system. The signal is represented by a dash arrow pointing away from the diagram, indicating the emission of photon. The signal can point to the left or right, depending on the state of system during time interval t_3. Since the system |a><b| and |b><a| are just complex conjugate of each other and essentially the same, we choose only the diagrams which emit signal to the left as most people do. Thus the sign of the signal is given by $(-1)^n$, where n is the number of interactions on the right side of the diagram.

Following the above rules, the Feynman diagram shown in Figure 2-1 contributes one term to a third order signal in (2.10). During the evolution, there are three interactions with the external electromagnetic fields and an interaction with the signal, which acts on the left or right side of the system depending on their phases. Therefore, the response function corresponding to the Feynman diagram is written as

$$\mathrm{R} = \langle \mu_{ab}(t)\mu_{ba}(0)\rho_{aa}(-\infty)\mu_{ab}(\tau_1)\mu_{ba}(\tau_2)\rangle \qquad (2.11)$$

The system starts at |a><a| state, denoted by $\rho_{aa}(-\infty)$, μ_{ab} and μ_{ba} correspond to the electromagnetic fields with phase $e^{-i\omega t+kr}$ or $e^{+i\omega t-kr}$. Each interaction of the system with electromagnetic field results in a change of quantum state. Based on Feynman diagrams, the relevant term of response function can be easily identified.

2.3 Third-order Spectroscopy

Linear methods, such as the steady state FTIR spectroscopy, can provide information on the existence of a certain chemical structure in given molecules, since this structure can be correlated to specific vibrational modes with characteristic transition frequencies. This is especially efficient in the fingerprint range where each compound produces a unique pattern of peaks. Thus, an analysis of the IR absorption spectrum of an unknown molecule can help identifying chemical groups and bonds in it. In principle, much structural information of the

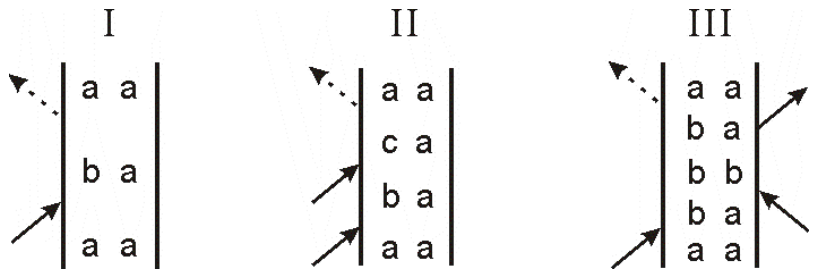

Figure 2-2: Double sided Feynman diagrams of linear absorption spectroscopy (I), second order SFG spectroscopy(II) and third order spectrscopy (III).

molecular system is reflected in the linear spectrum. However, after projecting the absorption onto a single frequency axis, different components overlap with each other and cannot be disentangled, such as couplings and interactions between two or more vibrational oscillators and different broadening mechanisms, which are strongly dependent on the three-dimensional structure of the molecules such as inter-atomic distances and orientations and the environment of molecules. Thus, spectroscopy with more parameters is needed to be introduced to help distinguishing contributions from different interactions. Time-resolved spectroscopy introduces time as the extra parameter. The coupling and interactions can be mapped by studying a dynamic process, when the interaction and coupling would bring an energy transfer or frequency shift of one oscillator due to the excitation of the other one. Different broadening mechanisms can be distinguished by mapping the frequency fluctuation beyond the static limit of the system-bath interaction. Therefore, a higher order spectroscopy is needed, where more interactions with pulses take place, as shown in Figure 2-2, and by controlling the time ordering and intervals the resolved dynamics of the system are feasible.

A second-order process is forbidden in a medium with inversion symmetry, which is usually the case when we study a liquid, a solution or a non-crystalline solid. Therefore, it is mainly used to study the interface by doing sum frequency generation [19, 20]. In order to study molecules in condensed phase, the third-order spectroscopy, which involves three interactions, is a more practical and prevailing tool.

Due to the broad spectrum of the pulse compared to the anharmonicity of the vibrational system, the transition v=1→2 is very often detected in the experiment. Thus, we usually consider our model system to be a 3-level system. The Liouville space pathways that have to be considered in a third-order experiment are depicted with double sided Feynman diagrams in Figure 2-3. The three interactions are brought by the same or different pulses, depending on different techniques. During time periods t_1 and t_3 the system is in a coherent superposition, when it undergoes free evolution. During time period t_2, the system is in the population state

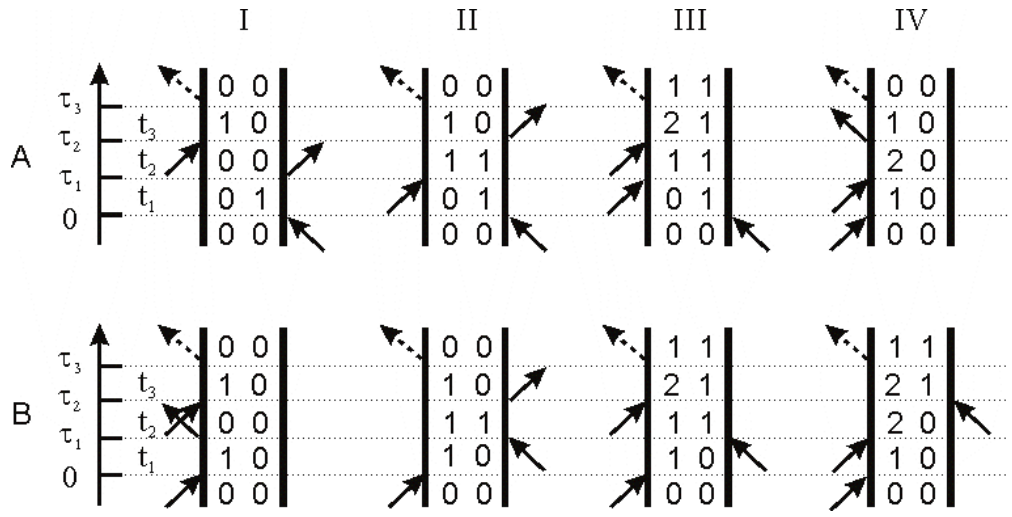

Figure 2-3: Double-sided Feynman Diagrams that have to be considered in a third-order spectroscopic experiment on a three level system. The three interactions occur in different moments. The moments of the interaction are denoted as τ_n, and the time interval between interactions are denoted as t_n. The states of the 3-level system are |0>, |1> and |2>. The energy of the state increases with the number.

as the diagrams in column I to column III show, but the existence of coherence superposition, as the diagrams in column IV show, cannot be excluded. The emitted signals from diagram IA to IIIA are called rephasing signal, because the coherence evolution in t_3 has the opposite phase compared to the coherence evolution in t_1. The others are called non-rephasing signal in contrast because the phase of the system in t_3 is the same as in t_1. In the following discussion, t_1, t_2 and t_3 will exclusively correspond to the three time intervals in the Figure 2-3, unless explicitly indicated otherwise.

According to the Feynman diagrams the response functions are given by:

$$\begin{aligned}
\mathrm{R}_{IA} &= \langle \mu_{01}(\tau_3)\mu_{10}(\tau_2)\rho_{00}\mu_{01}(0)\mu_{10}(\tau_1)\rangle \\
\mathrm{R}_{IB} &= \langle \mu_{01}(\tau_3)\mu_{10}(\tau_2)\mu_{01}(\tau_1)\mu_{10}(0)\rho_{00}\rangle \\
\mathrm{R}_{IIA} &= \langle \mu_{01}(\tau_3)\mu_{10}(\tau_1)\rho_{00}\mu_{01}(0)\mu_{10}(\tau_2)\rangle \\
\mathrm{R}_{IIB} &= \langle \mu_{01}(\tau_3)\mu_{10}(0)\rho_{00}\mu_{01}(\tau_1)\mu_{10}(\tau_2)\rangle \\
\mathrm{R}_{IIIA} &= \langle \mu_{12}(\tau_3)\mu_{21}(\tau_2)\mu_{10}(\tau_1)\rho_{00}\mu_{01}(0)\rangle \\
\mathrm{R}_{IIIB} &= \langle \mu_{12}(\tau_3)\mu_{21}(\tau_2)\mu_{10}(0)\rho_{00}\mu_{01}(\tau_1)\rangle \\
\mathrm{R}_{IVA} &= \langle \mu_{01}(\tau_3)\mu_{12}(\tau_2)\mu_{01}(\tau_2)\mu_{10}(0)\rho_{00}\rangle \\
\mathrm{R}_{IVB} &= \langle \mu_{12}(\tau_3)\mu_{21}(\tau_1)\mu_{10}(0)\rho_{00}\mu_{01}(\tau_2)\rangle
\end{aligned} \tag{2.12}$$

These eight response functions describe the nonlinear response of a 3-level system.

2.4 Calculation of Optical Response Function

For the two states of the oscillator, |a> and |b>, the effect of the interactions with the environment can be described as

$$H = H_0 + \hbar\delta\omega(t) \tag{2.13}$$

Where is the environment Hamiltonian. The dipole operator μ_{ab} is expanded as

$$\begin{aligned}\mu_{ab}(t) &= \exp\left[\frac{i}{\hbar}(H_a + \hbar\delta\omega_a(\tau))t\right]\mu\exp\left[-\frac{i}{\hbar}(H_a + \hbar(\omega_{ba} + \delta\omega_b(\tau)))t\right] \\ &= \mu\exp(-i\omega_{ba}t)\langle\exp[-i(\delta\omega_b(t) - \delta\omega_a(t))]\rangle \\ &= \mu\exp(-i\omega_{ba}t)\left\langle\exp\left[-i\int_0^t \delta\omega(\tau)d\tau\right]\right\rangle\end{aligned} \tag{2.14}$$

ω_{ab} is the transition frequency of the system; $\hbar\delta\omega_a(\tau)$ and $\hbar\delta\omega_b(\tau)$ are the time-dependent frequency fluctuations of |a> and |b> states caused by the solvent. The difference of two fluctuations, $\delta\omega(\tau)$, is assumed to be a stationary Gaussian distribution with mean value at zero. Thus the response function is expanded as

$$\begin{aligned}R &= \langle\mu_{ab}(t)\mu_{ba}(0)\rho_{aa}(-\infty)\mu_{ab}(\tau_1)\mu_{10}(\tau_2)\rangle \\ &= \mu^4\exp[-i\omega_{ba}(t + \tau_1 \\ &\quad - \tau_2)]\rho_{aa}(-\infty)\left\langle\exp\left[-\frac{i}{\hbar}\left(\int_0^t \delta\omega(\tau)d\tau + \int_0^{\tau_1} \delta\omega(\tau)d\tau - \int_0^{\tau_2} \delta\omega(\tau)d\tau\right)\right]\right\rangle \\ &= \mu^4\exp[-i\omega_{ba}(t + \tau_1 - \tau_2)]\rho_{aa}(-\infty)\left[1 + \frac{1}{2!}\left(\frac{i}{\hbar}\right)^2\int_0^t\int_0^t\langle\delta\omega(\tau')\delta\omega(\tau")\rangle d\tau' d\tau"\right. \\ &\quad + \frac{1}{2!}\left(\frac{i}{\hbar}\right)^2\int_0^{\tau_1}\int_0^{\tau_1}\langle\delta\omega(\tau')\delta\omega(\tau")\rangle d\tau' d\tau" + \frac{1}{2!}\left(\frac{i}{\hbar}\right)^2\int_0^{\tau_2}\int_0^{\tau_2}\langle\delta\omega(\tau')\delta\omega(\tau")\rangle d\tau' d\tau" \\ &\quad \left. + \left(\frac{i}{\hbar}\right)^2\int_0^t\int_0^{\tau_1}\langle\delta\omega(\tau')\delta\omega(\tau")\rangle d\tau' d\tau" - \left(\frac{i}{\hbar}\right)^2\int_0^{\tau_1}\int_0^{\tau_2}\langle\delta\omega(\tau')\delta\omega(\tau")\rangle d\tau' d\tau" + \cdots\right] \\ &= \mu^4\exp\left[-\frac{i}{\hbar}\Delta_{ba}(t + \tau_1 - \tau_2)\right]\exp[-g(t) + g(\tau_2) - g(\tau_1) + g(t - \tau_1) - g(t - \tau_2) \\ &\quad - g(\tau_2 - \tau_1)]\end{aligned} \tag{2.15}$$

Or it can be written with different time notes as

$$R(t_3, t_2, t_1) = \mu^4 \exp\left[-\frac{i}{\hbar}\Delta_{ba}(t_3 + t_1)\right] \exp[-g(t_1) - g(t_2) - g(t_3) + g(t_1 + t_2) + g(t_3 + t_2) - g(t_1 + t_2 + t_3)] \quad (2.16)$$

$\Delta_{ab}/\hbar=\omega_{ab}$ is the transition frequency of the system with which the phase of the coherence evolves during the time interval t_i if the system is in the coherent state |a><b|. When a=b, the frequency is zero. In contrast, the frequency fluctuations of the system undergo all the time regardless of on which state the system is.

The frequency fluctuations of the system is measured by $g(t)$, as the frequency-frequency correlation function (FFCF). The cumulant approximation then gives

$$g(t) = \int_0^t \int_0^t \langle \delta\omega(\tau')\delta\omega(\tau'')\rangle d\tau' d\tau'' = \int_0^t \int_0^t C(\tau' - \tau'')d\tau' d\tau'' \quad (2.17)$$

As a two-point correlation, $C(\tau'-\tau'')$ does not describe how the system behaves but only measure the system's memory for its previous transition frequency after $(\tau'-\tau'')$. Thus, $C(\tau'-\tau'')$ is a measure of the frequency fluctuation, a simple approximation of which is given by the Kubo model.

The Kubo model deals with the system in the fast modulation or slow modulation limits. In the fast modulation limit, the fluctuation of the environment goes so fast that the transition frequency changes much quicker than the time resolution of the measurement. Thus $\delta\omega(\tau')$ can be any value following the distribution regardless what $\delta\omega(\tau'')$ is. As a result, the correlation fuction $C(\tau'-\tau'')$ decays very fast and can be approximated by a δ-function $C(\tau'-\tau'')\rightarrow\delta(\tau'-\tau'')$. In the slow modulation limit, the fluctuation goes so slow that the transition frequency of the system stays the same throughout the measurement. Thus $\delta\omega(\tau')$ stays the same as $\delta\omega(\tau'')$. In this situation, the correlation function $C(\tau'-\tau'')$ does not change and can be approximated by a constant $C(\tau'-\tau'')\rightarrow\Delta^2$, where Δ is the root mean square amplitude of the frequency excursion. When both limits fail, the $\delta\omega(\tau'-\tau'')$ will slowly move away from $\delta\omega(0)$, and the correlation is lost after some moments. In this case, the decay of the

correlation is often modeled by an exponential decay, as an interpolation between the fast and slow limits, yielding

$$C(t) = \Delta^2 \exp\left(-\frac{t}{\tau_c}\right). \tag{2.18}$$

τ_c is called correlation time indicating how long it takes for the correlation to be lost. Substituting it into equation (2.17), we can get the Kubo-lineshape function [21]:

$$g(t) = \Delta^2 {\tau_c}^2 \left[\exp\left(-\frac{t}{\tau_c}\right) + \frac{t}{\tau_c} - 1\right] \tag{2.19}$$

In linear spectroscopy, within this stochastic model the lineshape is given by

$$I(\omega) = \frac{1}{\pi} \int_0^\infty dt \cos(\omega t) \exp\big(-g(t)\big) \tag{2.20}$$

This model applies very well for stochastic relaxations. It has been used by Kubo [21], Skinner [22] and many others to discussed the lineshape function.

It should be noted, that the Kubo model is only a simple approximation of the frequency fluctuation of the system in condensed phase. For a more detailed and accurate investigation of molecular system in solution, where the environment fluctuates similarly to the solute, the more sophisticate multi-mode Brownian oscillator model was developed [23, 24].

2.5 Spectroscopic Techniques

2.5.1 Coherence Evolution Measurement

During the coherence time, coherent polarization oscillates with its transition frequency Δ_{ab}. Thus, the time evolution of the coherent polarization contains the information on the fluctuation of the transition frequency. As a result, it is important to measure it to understand the system. In the third order spectroscopy, there are two time periods dominated by coherent polarizations, denoted by t_1 and t_3 in Figure 2-3. The evolution of the coherent polarization during t_3 is measured via the emitted signal after the interaction between the system and the third pulse. The direct measurement of the signal emitted during the first coherence time, explicitly the time interval t_1, is only feasible when it is not disrupted by any following

interaction and results in a linear absorption, giving no information on the dynamics of the system. For this purpose, the photon echo technique is developed. The name "photon echo" comes from the nuclear magnetic spin echo experiment, of which the photon echo spectroscopy is regarded as the optical analog.

Referring to the Feynman diagrams IA to IIIA in Figure 2-3, which are involved in a photon echo experiment, the three pulses interact with the sample as following: The system starts as a population in ground state, ρ_{00}. The first pulse creates a coherent superposition, $\rho_{01}(\tau)$, at time zero on the sample, which oscillates with its transient frequency $\omega = (E_1 - E_0)/\hbar$ and decays as a function of time with its dephasing time. This process is known as the free induction decay. The inhomogeneous distributed oscillators start to become out of phase with each other because they oscillate at different frequencies. The second pulse comes after a coherence time τ, and converts the coherence superposition into the population state. Depending on the relative phase difference between the second pulse and the coherent superposition, it can either results in a ground state population $\rho_{00}(\tau,T)$ (Figure 2-3 IIA), or an excited state population, $\rho_{11}(\tau,T)$ (Figure 2-3 IIIA). The population at excited state decays as the function of time with its population lifetime. After the so called population time[1] T, the third pulse arrives and generates coherent superposition $\rho_{10}(\tau,T,t)$ (Figure 2-3 IIA) or $\rho_{21}(\tau,T,t)$ (Figure 2-3 IIIA) again. This coherence superposition carries on with the free evolution but with a opposite phase compared to the coherent superposition in τ. Therefore, after a time period as long as τ, all the inhomogeneously distributed oscillators become in phase again, when their angular velocities do not change, and emit an echo signal. This is also called stimulated photon echo signal (PE) or rephasing signal. In contrast, the Feynman diagrams IVA and I-IVB in Figure 2-3 describe the other possibility, where the evolutions of the coherences in t_1 and t_3 have the same phase direction. As a result, the coherent polarizations undergo the same free induction decay in t_3 as in t_1 and the echo signal is absent.

For the recurrence of the initial macroscopic polarization and the generation of the echo signal, the order of the interactions of matter with pulses is restricted to be $-\mathbf{k}_1+\mathbf{k}_2+\mathbf{k}_3$ (Figure 2-4 right) according to Figure 2-3. The phase matching condition $-\mathbf{k}_1+\mathbf{k}_2+\mathbf{k}_3$ is chosen by

[1] Note that the name "population time" is essentially accurate only in the situation where there is only one oscillator and the pulse sequence obeys the rephasing requirement as we discussed here. However, it does not necessary mean that there are only population states existing, with the systems with multi-oscillators or with other pulse sequence. In those situations, the system could be in double excited coherent superposition. But usually during this period, the population states are in dominant role and coherent superpositions are neglected in most cases.

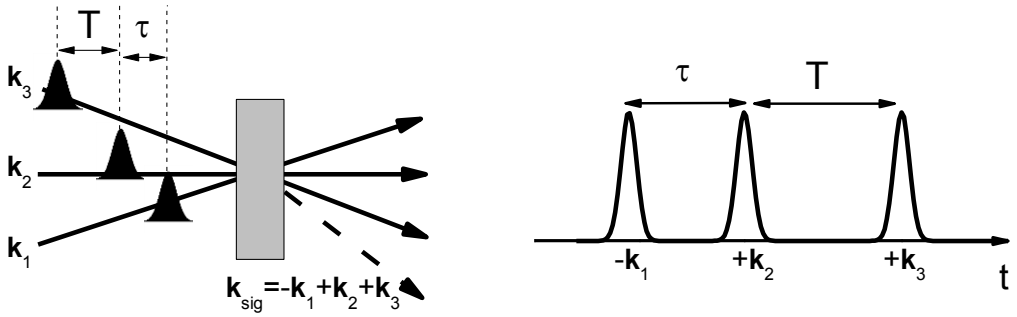

Figure 2-4: Schematic arrangement of k-vectors in a four-wave-mixing 2D experiment in space (left) and time domain (right). It is a background free experiment, with which we are able to measure pure signal without local oscillator light.

measuring signal in a phase matching direction (Figure 2-4 left) in the non-collinear geometry, which is the case in our experimental setup discussed in next chapter.

Note that the echo signal comes from the static inhomogeneity, namely the inhomogeneity which does not change in this time scale. Otherwise, the different frequency components of the inhomogeneous system evolve in different angular velocities during t_3 as they did during t_1. Thus they can never get in phase perfectly again. This situation occurs for systems where spectral diffusion plays an important role. In addition, if the system is purely homogenously distributed, all oscillators will oscillate in the same frequency in two coherence evolution periods. As a result, they would be all the time in phase with each other, and no rephasing or echo signal will be generated. Nonetheless, the term "photon echo" is a widely accepted concept and name for such cases regardless the homogeneity and inhomogeneity of the system being interrogated. Based on this scheme, a few types of echo experiment are developed.

a) In a two-pulse photon echo (2PE) experiment, the population time T is fixed at zero, and the second and the third interaction with the sample occur simultaneously. The signal is measured as a function of coherence time and gives information on overall decay of the macroscopic polarization of the sample. Due to the direct relation between the static inhomogeneity of the system and the intensity of the echo signal, one can measure the loss of inhomogeneity [25].
b) In the three-pulse photon echo (3PE), both delays τ and T are changed. The polarization dynamics can be monitored in a more complete way. It allows for a distinction of different dephasing and the underlying couplings[26].

c) If one measures the peak shift of the signal in ii, the three-pulse echo peak shift (3PEPS) measurement is performed. As a result, the inhomogeneity change during population waiting time, for example spectral diffusion, can be measured[27-29].

On the other hand, if the coherence time is fixed at zero in a transient grating scattering measurement, the signal is scanned as a function of population time instead of the coherence time, thus the population evolution is measured like in pump-probe measurement.

2.5.2 Population Evolution Measurement

Pump-probe spectroscopy is the earliest introduced and most popular third-order spectroscopic technique for decades for its simplicity and powerfulness. As shown in Figure 2-5, a conventional pump-probe spectroscopy employs typically two pulses. The intense pump pulse arrives first in the sample to create an optical transition, which is probed by a weak probe pulse after a certain time period T_{delay}. The later passes through the sample at a slightly different angle to separate itself from the pump pulse. The probe generates a transient third order polarization $P^{(3)}$, which, as a result, generates an electromagnetic field, E_{signal}, that propagates along the same direction as probe. The emitted field and the probe pulse are measured by a detector, with frequency resolved or not. The method of detecting a frequency-modulated electromagnetic field by mixing it with a reference field is called heterodyne detection. The mixing of the signal causes changes of the intensity of the reference light, which is usually regarded as the absorption change of the sample, when the signal is weak compared to the reference, i.e., the probe in this situation. By measuring the intensity of the probe with or without the excitation of pump, we can get the absorption change induced by the pump, given by

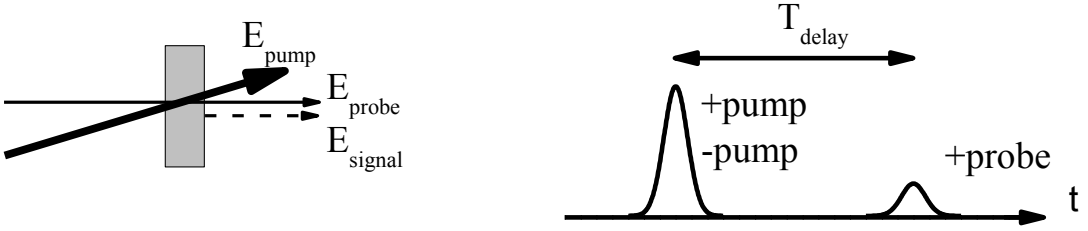

Figure 2-5 Schematic arrangement of k-vectors in a pump probe experiment in space (left) and time domain (right). The probe pulses acts as a local oscillator pulse meanwhile.

$$\Delta A(\omega) = -\log\left[\frac{I(\omega)}{I_0(\omega)}\right] = -\log\left[\frac{\int_{-\infty}^{\infty} dt\left|E_{probe}(\omega) + E_{signal}(\omega)\right|^2}{\int_{-\infty}^{\infty} dt\left|E_{probe}(\omega)\right|^2}\right] \tag{2.21}$$

$$\approx -\log\left[1 + \frac{2\int_{-\infty}^{\infty} dt\left|E_{probe}(\omega)E_{signal}(\omega)\right|}{\int_{-\infty}^{\infty} dt\left|E_{probe}(\omega)\right|^2}\right] \approx \frac{2\int_{-\infty}^{\infty} dt\left|E_{probe}(\omega)E_{signal}(\omega)\right|}{\int_{-\infty}^{\infty} dt\left|E_{probe}(\omega)\right|^2}$$

$$\propto \frac{2E_{probe}(\omega)E_{signal}(\omega)}{{E_{probe}}^2(\omega)} \propto \frac{iP^{(3)}(\omega)}{E_{probe}(\omega)} = \frac{i\chi^{(3)}{E_{pump}}^*(\omega_1)E_{pump}(\omega_2)E_{pump}(\omega_3)}{E_{probe}(\omega)}$$

Here the emitted signal E_{signal} is approximated to proportional to iP according to the slowly varying envelope approximation. ω_1, ω_2 and ω_3 are the frequencies of the pump and probe in the interaction and fulfill the phase matching condition $\omega=-\omega_1+\omega_2+\omega_3$. Thus, they are not necessary the same frequency as being probed and cannot cancel each other simply. In the pump probe experiment, the time interval between the first two interactions, which occur within the pulse duration, is usually very short; thus due to negligible fluctuation of the oscillating frequency we can regard ω_2 equals to ω_1, and, as a result, ω_3 equals to ω. As a result, the signal is $i\chi^{(3)}E^*_{pump}(\omega_1)\,E_{pump}(\omega_1)$. However, it is still impossible to correct for the amplitude of $E_{pump}(\omega_1)$, before knowing ω_1 precisely. In most cases, we can either assume that the spectrum of pump is flat in the area due to spectrally much broader spectrum of ultrashort pulses compared to the excited peak or regarded it as a spectrally δ peak for the pump spectrum is so narrow. The effect of the pump spectrum on the lineshape of the signal is therefore neglected. Note that the signal due to the coupling between different oscillators is beyond the capability of the correction here. Thus the result can be simplified to be

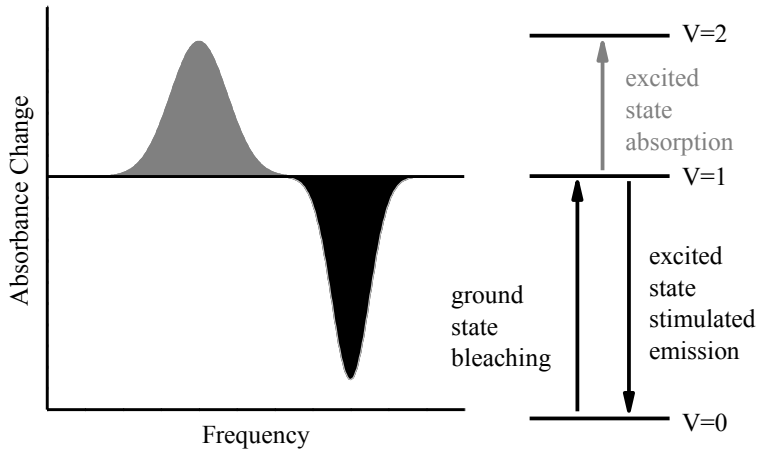

Figure 2-6: Frequency-resolved signal (left) of a pump probe measurements, with three-level structure on the right. The grey part is the increased absorption due to the excited state absorption and the black signal is the decreased absorption due to the ground bleaching and the stimulated emission as shown in the right.

$\Delta A(\omega) \propto i\chi^{(3)}$ with the $E_{pump}(\omega_1)$ being a constant over the pulse's spectrum.

When the pump and probe pulses are temporally separated, the three interactions can only occur in one certain time sequence, that the pump interacts before the probe. The amount of possible Liouville space pathways is 6 as shown in first three columns in Figure 2-3. The diagrams in column I give signal of ground state bleaching, column II contribute to stimulated emission, and column III contribute to excited state absorption. The resulting signals are shown in Figure 2-6. Both the ground state bleaching and the excited state stimulated emission lead to a decrease of absorption, meaning a negative signal, while the excited state absorption leads to an increase of absorption corresponding to a positive signal. For an anharmonic vibrational system, the v=1→2 transition requires less energy than the v=0→1 transition. Thus, the excited state absorption signal is shifted to the lower frequency relatively. The displacement is dependent on the anharmonicity of the system. And for vibrational oscillators, excited state absorption is generally broader because of shorter life time of v=2 state.

However, when pump and probe pulses overlap with each other, the interaction with the probe can occur before one or both of interactions with the pump. Thus Feynman diagrams in column IV of Figure 2-3 are possible and contribute to ground state bleaching (IVA) and excited state absorption (IVB) respectively. As a result, the amount of possible Liouville space pathways is 8×2=16. When the probe is detected with frequency resolved, this time disorder will cause a perturbed free induction decay at negative T_{delay} and coherence spike during the pulses overlapping when T_{delay} equal 0 in time domain [30].

In the pump-probe measurement, the time difference between pump and probe pulse, which corresponds to t_2, is controlled. As a result, the population evolutions are studied by this technique. In a polarization sensitive measurement, the change of the anisotropy can help extract the information of interactions and coupling between different chromophores [31, 32].

2.5.3 2D Spectroscopy

When the spectrum is highly congested, the pump-probe technique would come up with some problems. The Figure 2-7 shows a system comprehending four peaks in a narrow spectral range. When it is excited by an ultrashort pulse which has a very broad spectrum and excites all the peaks within its spectral envelope, all the peaks simultaneously react as Figure 2-6 shows. For anharmonic vibrational oscillators, the ensemble of decreases of absorption due to

v=0→1 transition, shown in black in panel (b), are similar to the linear spectrum in panel (a), while the enhance absorption due to v=1→2 transition, shown in light grey in panel b, is red shifted and spectrally broader. For the detector, they all add to a final signal shown in panel c. The overlapping of different signals coming from different transitions leads to a strongly distorted result, and it is extremely difficult to derive reliable individual spectra of the peaks. Hence it is impossible to extract the anisotropy and the lineshape evolution of an arbitrary peak.

In contrast, the multi-dimensional spectroscopy can help to overcome this problem. By resolving the frequency of excitation in the extra dimension, it is possible to unravel the source of different signal. As shown in panel (d) of Figure 2-7, the two-dimensional (2D) spectroscopy achieved by stretching the vertical dimension as excitation frequency disentangles the strongly overlapping of the signals. The v=0→1 transition signal is located at diagonal for the excitation frequency equal detection frequency. The homogeneously broadened peaks, such as 1, 2 and 3, appear to be like a circle[2]. For an inhomogeneously broadened peak, such as 4, the two dimensional lineshape looks like an ellipse, corresponding to the ensemble of oscillators with slightly different fundamental frequencies. For vibrational spectroscopy, the v=1→2 transition is located on the lower detection frequency side of v=0→1 transition due to the anharmonicity of the oscillators. The two different contributions

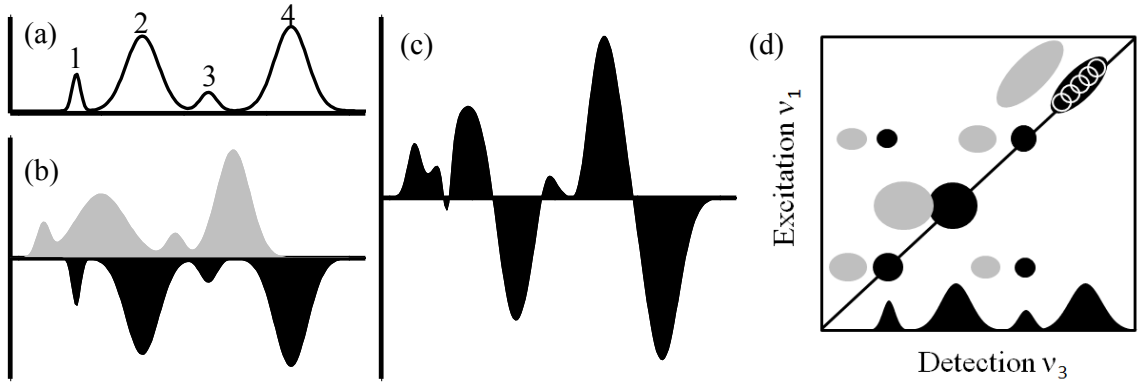

Figure 2-7: (a) The linear absorption of the four peaks of the system. (b) The bleaching and stimulated emission contributions (black) and excited state absorption contribution (grey). (c) Final pump-probe signal detected on the detector as a combination of two contributions. (d) Two-dimensional plots by resolve the excitation frequency in vertical dimension, the solide line is to highlight the diagonal of the spectra where $\upsilon_1 = \upsilon_2$.

[2] In principle the homogeneous peak appears as a diamond, while every cross section along excitation or detection dimensions results in a Lorentz lineshape. However in reality it is very often like circle because the center of the peak is more round and the diamond looking wings are less obvious.

of homogeneously broadened peak with smaller anharmonicity than the line width of the peak, such as peak 2, still overlap and distort the lineshape. But the inhomogeneously broadened peak, like 4, is possibly separated into two contributions for the smaller anharmonicity compared to the line width of the single oscillator. If two oscillators have connection with each other, in forms of anharmonic coupling, energy transfer, coherence transfer, chemical exchange, physical transformation and so on, the cross peaks will appear, such as the ones corresponding to the peaks 1 and 3. The cross peaks consist of negative and positive contributions as well. The separation between the two contributions is the off-diagonal anharmonicity of two oscillators or the anharmonicity of the accepting modes, which will be discussed later. The 2D spectroscopy appears clearly to be very powerful and has significantly increased information content [33].

In order to generate a 2D spectroscopy plot, excitation is needed to be frequency resolved. We can either selectively excite oscillators with certain frequency, or excite all oscillators regardless their frequencies and resolve the excited polarization by studying the free induction decay during the first coherence time t_1. Based on these two approaches, two techniques, 2D pump probe which scan a narrow pump pulse in frequency domain and Fourier transform 2D (FT 2D) spectroscopy which scan the second pulse-sample interaction in time domain, were developed.

The 2D pump probe, also known as dynamic hole-burning spectroscopy, was the first implementation of nonlinear 2D vibrational spectroscopy [34]. With a spectrally narrow pump pulse, spectral width down to 9-10 cm^{-1} in the case of Hamm's experiment, the excitation frequency is restricted in a small range and is regarded as known. Then by probing the sample with a spectral broad probe pulse, it is possible to build a 2D spectroscopy plots by scanning the pump pulse through the whole spectral range. An improvement [35, 36] was made latter to accomplish a 2D plot in single shot by dispersing the pump pulse on the sample, thus the spatially different parts of the sample are excited by pump with different frequencies, i.e. dynamic hole-burning measurements at different pump frequencies are done simultaneously. They are both basically conventional pump-probe technique, involving two pulses serving as the pump and the probe respectively. The spectrally narrowed pump will result in a lengthening of the pulse, leading to a time resolution of the dynamics of the order of picoseconds [34]. As the first two interactions are done by the same pulse, this scheme provides less experimental control over the Liouville pathways [37].

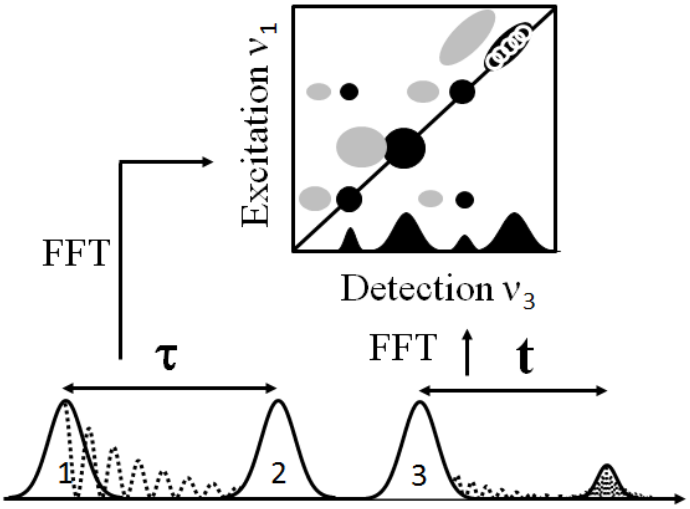

Figure 2-8: The scheme for the FT 2D spectroscopy. The two coherence time are Fourier transformed into frequency domain to creat a frequency-frequency correlation plot.

FT 2D spectroscopy was first demonstrated by Ernst's group with NMR [38]. It can be regarded as an improvement of spin echo experiment, which studies the time evolution during coherence time. The 2D IR spectroscopy is an optical analog of the 2D NMR [39-43]. By controlling the coherence evolution time t_1 of the coherence superposition generated by the first interaction, the excitations at different frequencies are able to be discerned. After having measured the signal as a function of the coherence evolution time, a Fourier transform of the coherence time and the signal results in an excitation frequency resolved signal, as shown in Figure 2-8. Using this method, all the oscillators covered by the broad spectrum of the ultrashort pulse are excited simultaneously, and the time resolution is maintained.

The difference between the photon echo and the FT 2D measurement lies not only on the Fourier transforms, but also the signal being considered. In the photon echo experiment, normally only the rephasing signals are considered, while in FT 2D spectroscopy, the absorptive signal is investigated, which is the real part of both the rephasing and non-rephasing signal. In principle, a Fourier transform of the pure rephasing signal is enough to give the absorptive part since it evolves as free induction decay. However, the problematic issue of the measurement is that it is impossible to perfectly separate the real part of pure rephasing signal from the imaginary part which is the dispersive signal [44, 45]. As a result, the peak appears to have a phase twist. To compensate this twist, an addition of equally weighted rephasing and non-rephasing signal are done. The distorted wing of both overlap with each other and canceled to give a pure absorptive peak.

Compared to the pump-probe experiment, same amount of Feynman diagrams are relevant in the 2D FT spectroscopy. Therefore, integrating the 2D plot along excitation frequency axis should result in a pump probe result in principle. On the other hand, the control of coherence time makes it a coherent experiment.

2.5.4 2D Plots of a Single Oscillator System

When there is an ensemble of only one kind of oscillators in the studied system, the response function of each Feynman diagram is decided by the transition frequency Δ_{ab} and the lineshape function $g(t)$, as have been discussed in section 2.4. As the transition frequency is given by the energy gap between the two states, the lineshape function strongly depends on the movement of the bath of the system.

In case of the slow modulation limit, the bath moves much more slowly compared to the molecular systems, the system-bath interactions can be regarded as time-independent too. However, the ensemble of the interaction appears an extra broadening because an enormous number of systems are coupled to a very large number of different bath modes (or the baths in different phase of their motion). As a result, the system-bath interactions are not same for different system. Consequently the Hamiltonian is not the same for all systems. This is also known as the static limit. In this limit, the relaxation of each single system can be completely described as an exponential decay, but the ensemble is more complex. In linear absorption spectrum, the transition is a sum of very many Lorentzian peaks and becomes inhomogeneously broadened. Statistically, this leads to a lineshape of Gaussian peak in linear spectroscopy.

In case of the fast modulation limit, the bath moves much more rapidly compared to the dynamics we are interested in, thus being regarded always at the thermodynamic equilibrium and the effect on the system can being averaged to constant parameters. This is also known as Markovian approximation. In this situation, because the ensemble of system-bath interactions can be regarded as time-independent and is same for all systems, the relaxation of the whole ensemble system can be nicely described as an exponential decay. Consequently, the broadening of the optical transitions is called homogeneous broadening and the lineshape of the transition is a Lorentzian peak in linear spectroscopy.

In the FT 2D spectroscopy, the different lineshapes present in a more pronounced way. When the oscillators are excited by laser pulses, these excitations will give a reduced absorptive

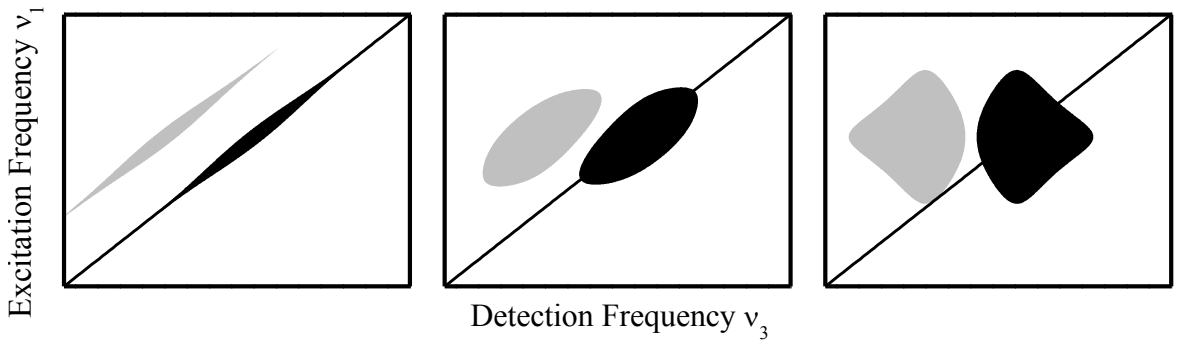

Figure 2-9: 2D plots of single oscillator system in different homogeneous and inhomogeneous broadening situations. Increased absorptions are shown as black peak on diagonal, and decreased absorptions are shown as light grey peaks.

signal, which consists of the ground bleaching and the stimulated emission contribution, and an enhanced absorptive signal, due to the excited state absorption, at lower detection frequency (Figure 2-9). In the slow modulation limit, the transition frequencies of different excited oscillators are not the same, which is resolved by the FT 2D spectroscopy, leading to signals at identical frequency as they are excited. Thus the resulting diagonal peak appears an ellipse along the diagonal of the 2D plot (Figure 2-9 left). The width along the diagonal is the linear absorption, describing the inhomogeneous distribution of the oscillators, while the anti-diagonal width is very narrow, due to very small homogeneous broadening compared to the inhomogeneous broadening. In the fast modulation, all the excited oscillators emit the same signal with the same Lorentz lineshape because they are experiencing the identical system-bath interaction, leading to a peak at diagonal with both cross sections along ν_1 or ν_3 appearing to be the same Lorentzian peak as in the linear spectrum (Figure 2-9 left). When both limits play a role, the peaks appears to be an intermediate between the two (Figure 2-9 middle). The cross sections along any direction are affected by the Gaussian and Lorentian components simultaneously. Generally, the diagonal cross sections are more dominated by the Gaussian component and the anti-diagonal cross sections by the Lorentzian component of the linear absorption. However, it should be noted that the overlap between the negative and positive contribution can distort the features and change the cross sections considerably.

If both limits failed, then the system does not have a static inhomogeneity, which means the bath is not time-independent for either the ensemble or single oscillator. As a result, the system-bath interaction evolves with time, making the transition frequency deviate from its initial value. This process is known as the spectral diffusion.

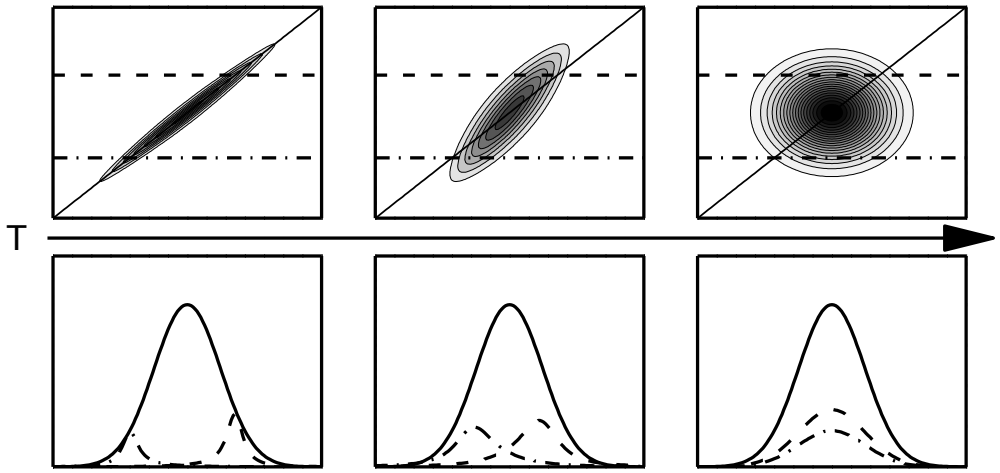

Figure 2-10: Illustration of spectral diffusion in form of 2D spectra. The upper panels are the 2D spectra and the lower panels are the linear spectrum. The population time is evolving from left to right. The dashed and the dash dot lines in the 2D spectra correspond to the directions along which the cross sections in the lower panel were made. In order to avoid the distortion of the negative contribution, only the positive signal are considered in this model.

The spectral diffusion is a process that diminishes the inhomogeneous distribution existing initially because of different system-bath interactions. In a spectral hole burning experiment, one excites an inhomogeneously broadened transition with a pulse whose bandwidth is smaller than the spectral width of the spectral broad transition, thus only a fraction of the molecule ensemble is excited to the higher state (Figure 2-10). If the inhomogeneity of the system is not static, due to the fluctuation of the structure or the bath of the system during the population time, which is the time period between the excitation and the detection, as a result, the initially distribution of the excited molecules is washed out, meaning that a certain set of system-bath configurations are eventually distributed over all possible situations. As a result, the detection signal will give a signal over broader range than initially excitation, i.e., spectral diffusion occurs. Thus, the spectral diffusion is a measure of how fast the structure or the environment changes.

The homogeneity and inhomogeneity are very often measured via the eccentricity [46, 47] or the center lines of the peak [48-50]. The center line is generated by finding the maximum of the cross sections, which is made along ν_1 or ν_3. The slope or inverse slope of the center lines are demonstrated to be correlated to the FFCF, therefore it is an efficient measure of the frequency fluctuation of the system.

2.5.5 2D Plots for System with Two Correlated Oscillators

Compared to a single-oscillator system, about which the most important information a 2D plot can tell us is the peak shape reflecting the different broadening mechanism, a 2D plot for a system with several oscillators can tell more information about the coupling and energy transfer between them.

For a two-oscillator system without any coupling or energy transfer, the two oscillators would be independent from each other. Therefore, the 2D plot is a simple sum of two as shown in Figure 2-11 (a), with the decreased absorption corresponding to v=0→1 transition and an increased absorption at lower detection frequency, corresponding to the v=1→2 transition. The distances, ΔA and ΔB, between these peaks come from the anharmonicity of the oscillator, and are called diagonal anharmonicity. If there exists any coupling between the two oscillators, for example common ground state, the excitation of one oscillator will change the transition frequency of the other. As a result, the coupled oscillator absorb photons at a different frequency, leading to a decreased absorptive feature at v=0→1 (1 is the initial excited state before the coupling oscillator is excited) and an enhanced absorptive peak at v=0→1' (1' is the new excited state when the coupling oscillator is excited) usually located at the red-shifted frequency as shown in Figure 2-11 (b). The distances between the two features, ΔAB, depending on the coupling strength of the system, is known as the off-diagonal anharmonicity. When there is any energy transfer between the two oscillators, the energy of one oscillator can hop to the other one. The relaxation of one oscillator excites the other oscillator, thus inducing the decreased and enhanced absorptive signal of the accepting

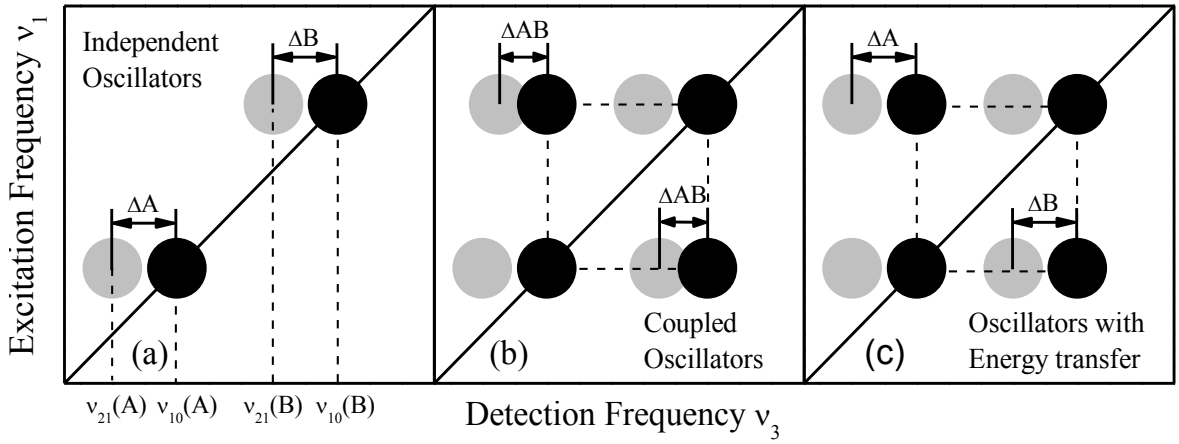

Figure 2-11 2D plots for two-oscillator system when they (a) are independent; (b) couple with each other; (c) have energy transfer between. Increased absorptions are represented by dark black peaks and decreased absorptions are represented by light grey peaks. All anharmonicities are assumed to be larger than the line width of peaks to avoid significant overlapping of different contributions, for the sake of simplicity.

oscillator. Therefore, the resulting signal will be identical to the features, when the accepting oscillator is directly excited by the pulse, with the excitation frequency equal to transition frequency of the first oscillator, as shown in the off-diagonal range of the Figure 2-11 (c). The distances between the positive and negative peaks are decided by the diagonal anharmonicity of the accepting oscillator, for the signal is attributed to the excitation of which. As shown in our plot, the distance between the positive and negative off-diagonal peaks in up left range is ΔA, and the distance of other pair is ΔB.

Although positive cross peaks in both cases appear to be located at the same position with a negative one on the left in a similar pattern, they come from different Liouville space pathways and have different properties. In the following we will discuss them based on the Liouville space pathways. In this discussion we will neglect all the pathways where the pulses interact only with the same oscillator, for they do not give information about cross peaks. And the pathways, due to which the nonrephasing signal is generated, are also out of our discussion here for it gives similar information as rephasing signal except the peak shape.

For a coupled two-oscillator system at ground state, $|00\rangle\langle 00|$ is used to represent it. The interacting pulses come from both sides, with different phase and vectors, and interact with arbitrary oscillator in double-sided Feynman diagrams. The ladder scheme and double-sided Feynman diagrams are shown in Figure 2-12. Note that there are still some forbidden pathways which involve simultaneous change in both states. Because the signal is too weak, they are not discussed here, and detailed discussion can be found in [45, 51]. Upon the coupling between the vibration A and B, the energy of double excitation is lowered by ΔAB. Therefore, the absorbing frequency of one oscillator is shifted for ΔAB to $\nu(A)$-ΔAB or $\nu(B)$-ΔAB, when the coupled oscillator has been excited in the first interaction. The corresponding Liouville space pathways are described with Feynman diagrams I, II V and VI in Figure 2-12. The pathways III, IV, VII and VIII in Figure 2-12 contribute to the decreased absorption signal. Interestingly half of the Feynman diagrams have an interstate coherence in population time T, when the system is supposed to have a population state. For most situations, the coherence decays very fast and contributes very little to the peaks, being neglected in our discussion here. As a result, the off-diagonal peaks are dominated by I, III, V and VII. The decreased absorption is attributed to a ground state path way and the enhanced absorption is attributed to an excited state path way. When the coupling strength ΔAB is smaller than the line width of the peak, the two signals with different sign will overlap significantly and cancel each other. As a result, the residue of the features will push each other away and show a

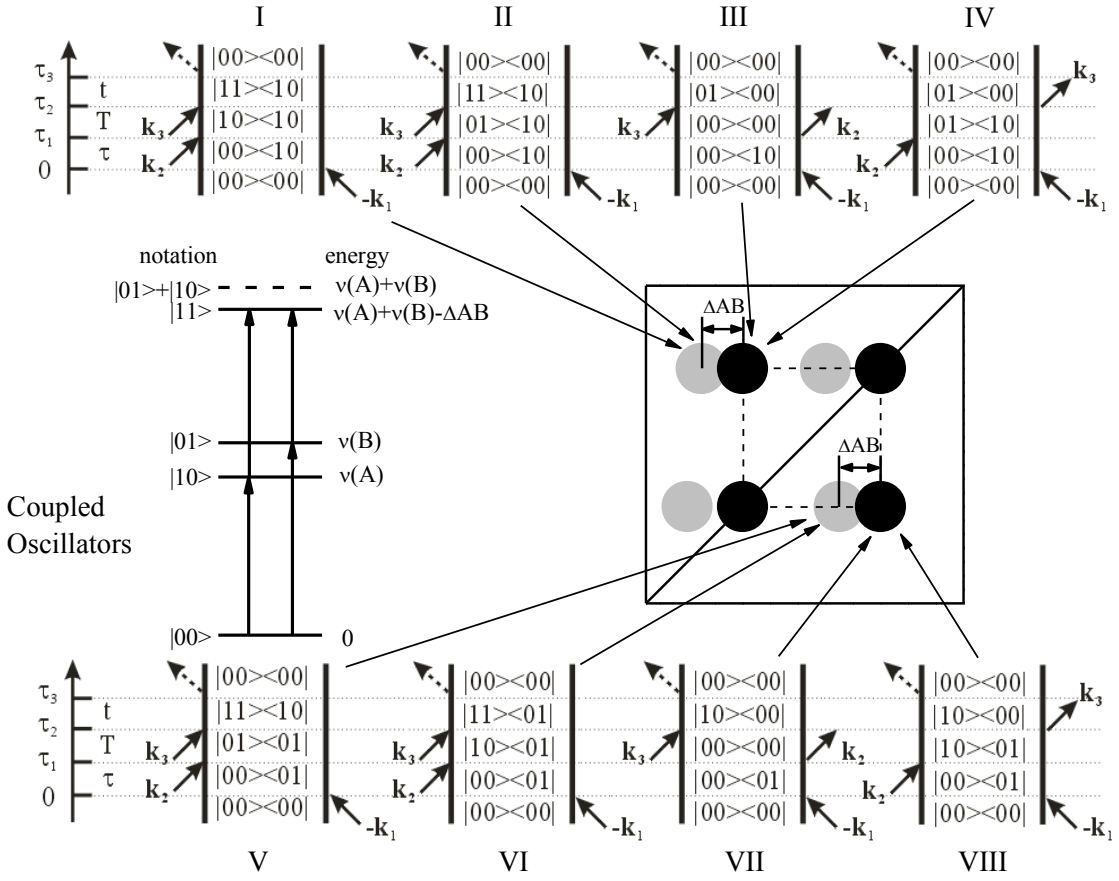

Figure 2-12 2D spectrum for 2 coupled oscillators, with the Feynman diagrams contributing to the cross peaks. The ladder scheme shows the energy level in the coupled system.

bigger separation between the positions of the positive and negative peaks. When the excitations of oscillator A and B decay and refill the ground state during time T, the system has only a single excitation during time t. The frequency of emitted signals from Feynman diagram I and V are then shifted back to the ν(A) or ν(B). This would weaken signal intensities of both cross peaks. Therefore we can conclude that the life time of cross peaks, as a function of T, is dominated by the life time of the initial excitation.

For a two-oscillator system, where we consider only energy transfer without coupling, |A> and |B> are used as the notations for the two oscillators respectively. For each oscillator, the energy, as shown in level scheme in Figure 2-13, are identical with the single oscillator shown in Figure 2-6. The Liouville space pathways which contribute to the cross peaks are described with double-sided Feynman diagrams I-IV in Figure 2-13. The energy transfer occurs during the population time T. When the oscillator A or B is excited by the first two pulses, the energy of the oscillator can transfer to the other one. The energy gap between two oscillators is compensated by the energy in manifold including low frequency modes. Therefore, when the third pulse comes, it will probe the excitation of B or A instead. Thus, while the oscillator A is

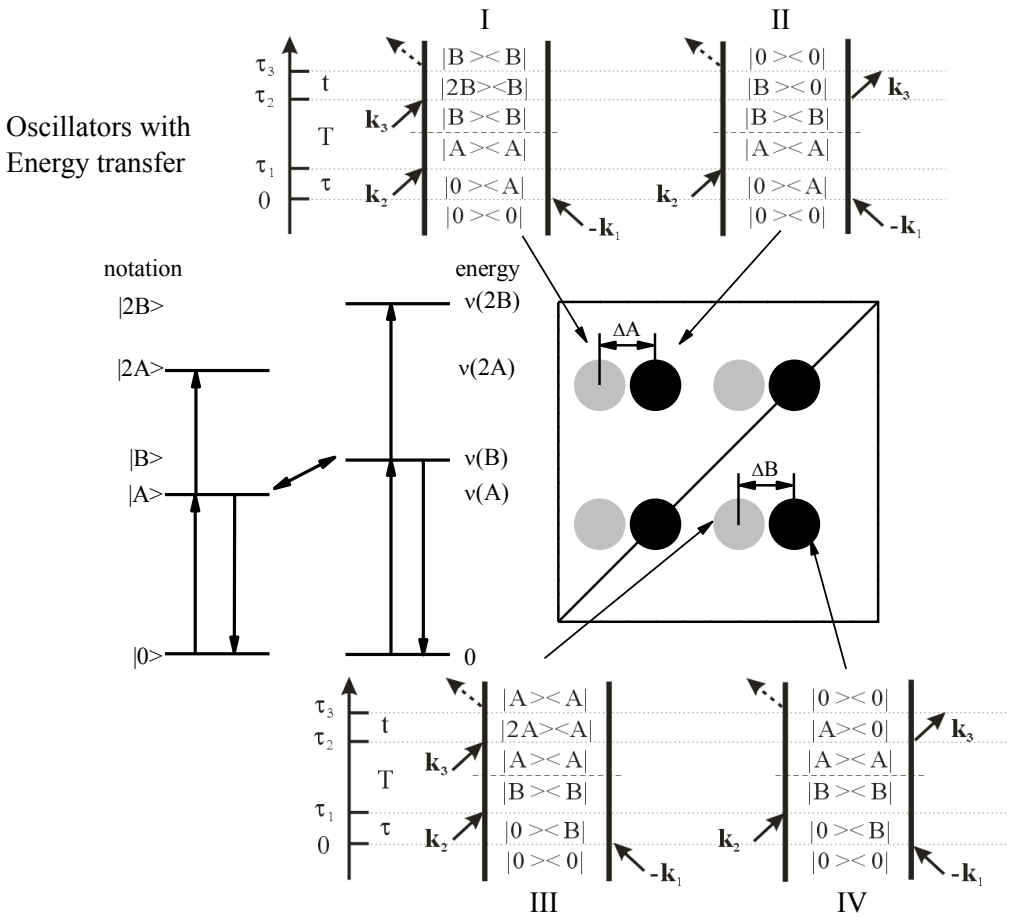

Figure 2-13 2D spectrum for two-oscillator system with only energy transfer, with the Feynman diagrams contributing to the cross peaks. The ladder scheme shows the energy level in the system.

excited at frequency ν(A), the decreased absorption in 2D plot appears at ν(B), corresponding to Feynman diagram II and IV in Figure 2-6, and the enhanced absorption appears at ν(B)-ΔB corresponding to Feynman diagram I and III in Figure 2-6, and vice versa. When the intensity of the signal is measured as a function of T, the transition time from one to the other and the life times of two oscillators all play a role here. Consequently, the evolution is rather a complicate process than simply be dictated by some oscillator. On both sides of the diagonal line there are energy transfers from A to B and vice versa. However, the downhill process, which means the population transfer from higher energy level B to lower energy level A, is much more efficient and faster than the uphill process. Therefore, the off-diagonal peaks on up left range are more intense than the lower right ones.

In reality, very often both the coupling and the energy transfer exist in the multi-oscillator system simultaneously. The coupling usually indicates a communication between the oscillators, which is basically essential and very often sufficient for occurrence of the energy transfer. This situation would make the analysis more difficult, as it introduces not only an

overlap of different off-diagonal peaks but also some extra peaks involving both processes. The combination with theoretical calculation would be helpful to understand the experimental results.

3. Experiments

Since the invention of laser in 1960 [52, 53], people have been aiming for shorter and more intensive pulses [54]. The extremely high intensity makes the nonlinear signal significant and the short pulse duration increases greatly the time resolution of dynamics.

With development of the Kerr-lens mode locking [55] and the Chirped Pulse Amplification (CPA) [56], the Ti:Sapphire laser system can generate pulses with a femtosecond pulse duration and peak powers up to terawatts, allowing for nonlinear frequency conversion. Optical Parametric Amplification is one of the most important methods for converting the fundamental wavelength around 800nm into a wide range from UV to IR at high pulse energy and short pulse duration.

3.1 Light Source

The light source we use consists of a commercial laser system which produces ultrashort pulses at 800nm, and an OPA system which converts the laser output into mid-IR spectral range [57-60] which covers the OH and NH stretching sensitive range we are interested.

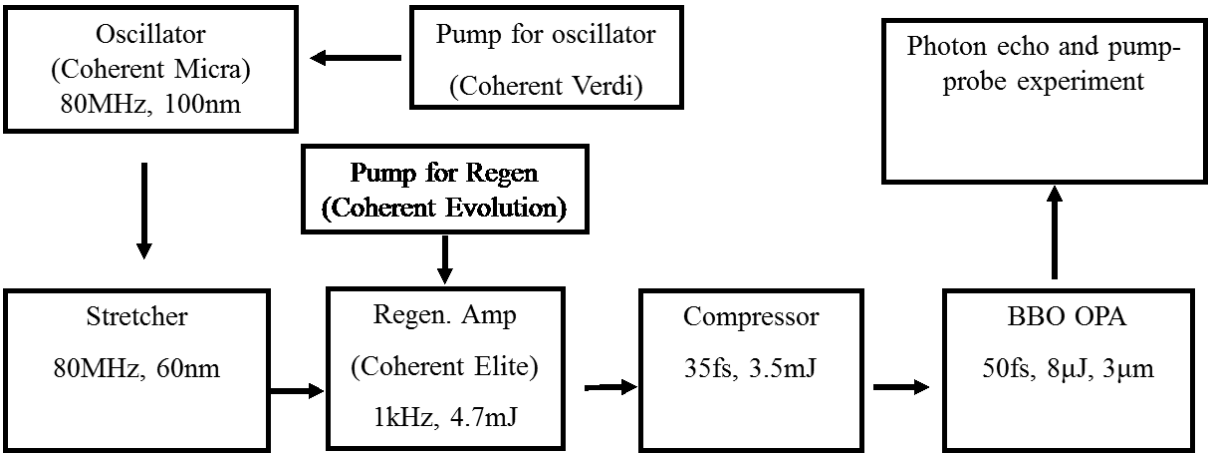

Figure 3-1 Overview of the experimental setup. It consists of a commercial laser system, a home build OPA and the photon echo and pump probe experiment setup.

3.1.1 Commercial Laser System

The 800nm laser pulses are generated by a commercial laser system (Coherent). It consists of a Ti:Sapphire oscillator (Micra) and a regenerative amplifier (Legend Elite). The oscillator is

pumped by an integrated intra-cavity doubled Nd:YVO_4 laser (Coherent Verdi) which emits continuous wave light at 532 nm. A pump laser power of 5 W results in around 400 mW output of the oscillator at a repetition rate 80 MHz. The oscillator employs Kerr-lens modelocking. The bandwidth of the spectrum is typically over 100 nm, centered at 800 nm. The output is then stretched by as much as 10,000 times in time, using a single grating stretcher, to significantly reduce the peak power and avoid the potential damage of the active medium in the amplifier by the high peak power during the amplification. The chirped pulse is then sent into the regenerative amplifier pumped by an integrated intra-cavity doubled Nd:YLF laser (Coherent Evolution-30), operating at a 1KHz repetition. The amplifying crystal is cooled down to -10ºC to compensate the thermal lens effect [61]. The pulse energy is increased by a factor of up to 10^6. After recompression, the output pulse has an energy of 3.5 mJ per pulse, with a pulse duration of 35 fs. The spectrum is centered at 800 nm with a bandwidth of more than 50 nm.

3.1.2 Optical Frequency Conversion

With extreme high intensity in the crystal, some nonlinear effects start to take effect because of the increasing weight of higher order nonlinear susceptibilities [62]. The second order nonlinear susceptibility $\chi^{(2)}$ is used for optical frequency conversion. In a crystal for which $\chi^{(2)}$ is nonzero, there can be new frequency ω_3 generated based on the frequencies ω_1 and ω_2 (assuming $\omega_1 > \omega_2$) of the incident light waves as

$$\omega_3 = \omega_1 \pm \omega_2 \tag{3.1}$$

and meanwhile, the wave vectors fulfill

$$\mathbf{k}_3 = \mathbf{k}_1 \pm \mathbf{k}_2 \tag{3.2}$$

the phase matching condition. If we rewrite it in form of refractive index and frequency, the condition for a collinear phase matching geometry is

$$n_3\omega_3 = n_1\omega_1 \pm n_2\omega_2 \tag{3.3}$$

For a medium where the refractive index increase or decreases monotonously, it is very often unfeasible to achiev the two phase matching conditions simultaneously. In principle people can use material with anomalous dispersion, which break the monotony, to fulfill the phase match conditions. However, crystals with birefringence like BBO or KTP are more popular

for flexibility. A birefringence is the dependence of refractive index on the direction of polarization of the light. With the axial of the crystal and the direction of the incident light, a principle plane is defined. The light with polarization normal to the principle plane is called ordinary ray, whose refractive index is isotropic. The light with polarization parallel to the principle plane is called extraordinary ray, whose refractive index is anisotropic. By tune the angle of the crystal and the polarization of the incident beam, we can fulfill the phase match condition in two ways proposed by Midwinter and Warner [63]. In type I the two low frequency beams are parallel in polarization, while the highest frequency one is perpendicular. In type-II the two low frequency beams are perpendicular with each other in polarization, and the highest frequency one is parallel with either of them.

In our setup, two kinds of nonlinear crystals are used. With BBO crystal (negative uniaxial, point group 3m, θ=30º, ϕ= 0º), type-II is achieved, and with $AgGaS_2$ (negative uniaxial, point group 42m, θ= 37 º, ϕ= 45 º) type-I is implemented.

3.1.3 OPA Setup

Because the BBO crystal we use in OPA has a strong absorption below 3000 cm^{-1}, the tuning range of direct conversion is limited. Therefore, a second conversion in $AgGaS_2$ is introduced to generate mid-IR at longer wavelengths. The scheme of the setup is shown in Figure 3-2 [57].

A beam with an energy of 1 mJ per pulse is split off from the amplifier output and sent into the OPA. For the first conversion, the incoming 800 nm pulse is split into 4 beams, which carry about 1%, 5%, 20% and 75% of the energy, respectively. The weakest beam is focused by a 100 mm lens on a 2 mm thick sapphire plate after being changed in polarization by 90 degrees. The high intensity in the focus generates a supercontinuum, which covers a spectral range from the visible to the near-IR, because of self-phase modulation [64]. A frequency component from the continuum serves as a seed for OPA. After passing a delay stage, the 10% branch is made collinear with the seed beam, and both are focused together to the upper part of a 4 mm BBO crystal, where the first parametric amplification takes place. The time overlapping of the two beams is achieved by adjusting the delay stage. The amplified signal light and the idler light propagate collinearly and pass a polarizing beam splitter which separates the signal from the idler light. The fundamental light has already been separated by a dichronic mirror before. The diverging parametric output of the signal frequency is re-collimated by a concave mirror and travels back to the lower part of the same BBO crystal.

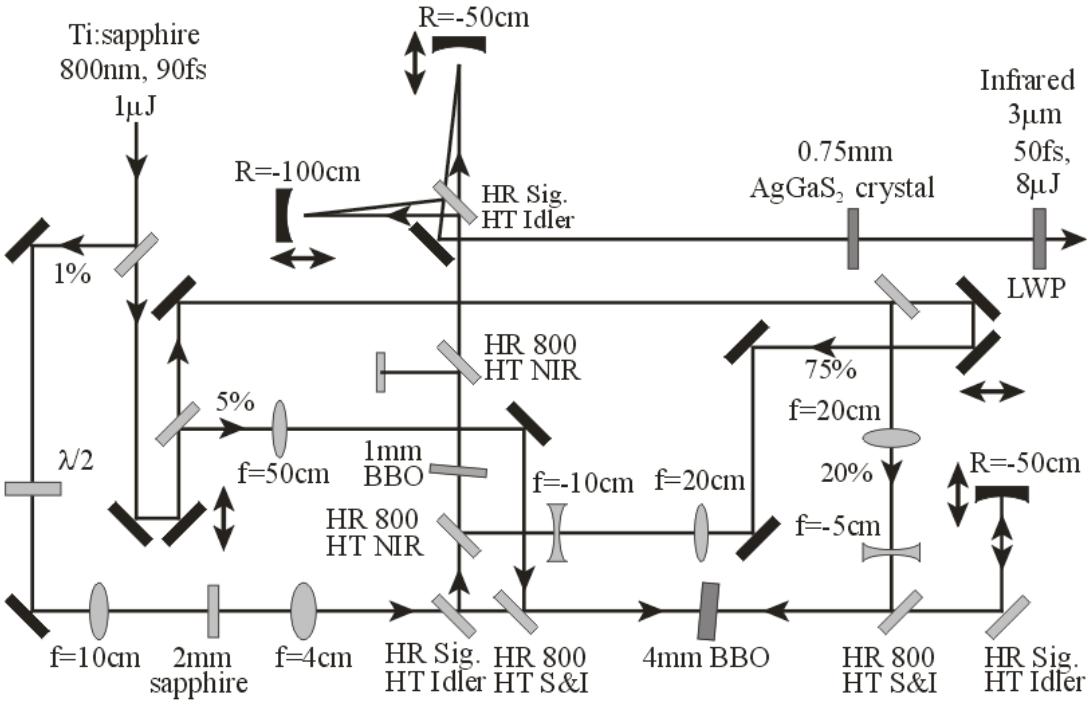

Figure 3-2: Scheme of OPA setup. The input laser is split into four branches to serve as seed and pump for the three stage amplification on BBO crystals. And the amplified signal and idler are refocused on the Ag_2GaS crystal to perform a DFG process to generate tunable mid-IR light. HR/HT: high reflectivity/transmission; S/I: signal/idler; LWP: long wave pass.

On the way to the crystal, the signal is combined with the 20% beam, the beam diameter of which has been decreased by a 4:1 telescope system to increase the intensity. With the same orientation of the BBO crystal relative to the light path and polarization, the signal is amplified for the second time. After the second amplification, the signal is again separated by polarizing beam splitter and goes through a 1mm BBO crystal. The forth beam which carries 70% energy arrives on the BBO crystal too after shrunk by a 2:1 telescope system. The BBO crystal is tuned to fulfill the same phase matching condition to perform the third pass amplification. After the second amplification, the energy of the signal and idler together is above 200 μJ per pulse. By tuning the angle of the BBO crystals, the spectrum of the signal is tunable from 1.2 μm to 1.5 μm, therefore the spectrum of corresponding idler varies from 2.4 μm to 1.7 μm.

The beam consisting of both signal and idler pulses is separated by a dichronic mirror. After reflections by two spherical mirrors, the two beams are recombined and focused on a 0.5 mm $AgGaS_2$ crystal, where the difference frequency of signal and idler is generated (DFG). This DFG process in the crystal generates mid-IR pulses with a spectrum tunable between 3 μm and 10 μm. The output energy is 8 μJ per pulse when the wavelength is around 3 μm. Two

spherical mirrors R = -1000 mm and R = -3000 mm are used to re-collimate the beam after the crystal. A long wave pass filter blocks the two input pulses and allows the mid-IR to go through. A CaF_2 plate is used to compensate the chirp of the pulse introduced by the crystals and mirrors in the OPA. For different alignments and wavelengths, the thickness of the plate can vary from 6 mm to 10 mm. The pulse duration is 55 ± 5 fs according to the Transient-Grating Frequency-Resolved Optical Gating (FROG) measurements after the compensation. The pulse stability is very high with rms less than 0.3% in the middle of the pulse spectrum, and less than 0.5% over the main part of the pulse spectrum.

3.2 Pulse Characterization

The characterization of the ultrashort pulses is mostly based on the autocorrelation and cross correlation techniques [65]. When two pulses, split from the same pulse or coming from different ones, overlap temporally and spatially simultaneously in a nonlinear material, the intensity of sum frequency generation or two-photon absorption, or any other nonlinear signals, will indicate to what extent the two pulses overlap. In the pump probe setup, we use a 70 μm Germanium to perform a two-photon absorption autocorrelation measurement. By change the time overlap, we can get the intensity of the signal decided by

$$I_{sig}(\tau) \propto \int_{-\infty}^{\infty} |E(t)E(t+\tau)|^2 dt = \int_{-\infty}^{\infty} I(t)I(t+\tau)dt \qquad (3.4)$$

The pulse duration is therefore equal to the temporal width of signal divided by factor $\sqrt{2}$ when it is assumed to be a Gaussian pulse. However, the autocorrelation needs an implicit assumption that the lineshape of pulse is already known, for example ideally Gaussian, which

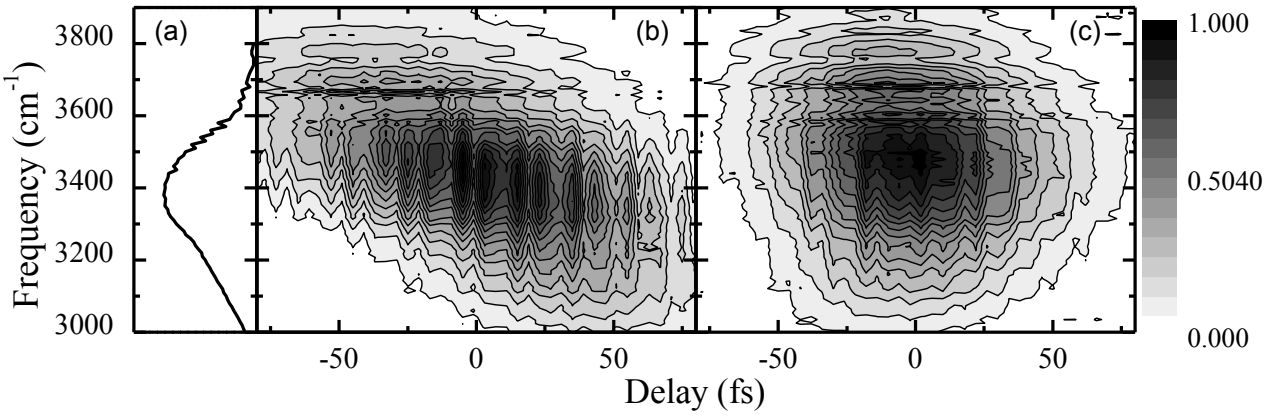

Figure 3-3: Frog trace of the chirped (b) and a chirp-compensated (c) ultrashort IR pulse. The dips in the frequency range is due to the absorption of vapor in the air, and the fluctuation in the time range causes by the interfering with the stray light. The spectrum of the pulse is shown in (a) for comparison.

is not always true. It cannot tell any phase information either. Therefore, a better way to characterize the pulse is proposed, which is frequency-resolved optical gating (FROG) [66].

A transient-grating FROG (TG-FROG) can be easily done on the photon echo setup, which will be discussed in next section. In a FROG measurement, two pulses are time overlapped to generate a transient grating on a medium with instantaneous response, e.g., CaF_2. The third pulse can be scattered by the grating in a specific direction fulfilling the phase matching condition. The intensity of the signal is given by [66]

$$I_{TG}(\tau) = \int_{-\infty}^{\infty} |E(t)E(t-\tau)E^*(t-\tau)|^2 dt = \int_{-\infty}^{\infty} I(t)I^2(t+\tau)dt \qquad (3.5)$$

from which we can retrieve the amplitude and frequency relation of the pulse, namely the FROG trace. FROG experiment is a background-free experiment, if we neglect the the scattering light from the imperfect interface.

An example is given in Figure 3-3. The spectrum of the output of the OPA is shown in panel (a) and the FROG trace of the pulse is shown in (b) and (c) as before and after a compensation of a 10 mm CaF_2 window. After the compensation, the pulse duration of the pulse is around 65 fs. The time band width product is around 0.5, which indicates that the pulse is close to transform limit. The parameters of pulses in the experiments of thesis are summarized in Table 3-1.

Table 3-1: Parameters of pulses in the experiments

Experiment	Center Frequency (cm^{-1})	Spectral Bandwidth (cm^{-1})	Pulse Duration (fs)	Time-bandwidth Product
0% AT oligomer	3250	273	61.88	0.48
92% AT oligomer	3400	230	65.5	0.48
92% AT oligomer	3250	229	70.4	0.55
GC base pair in $CHCl_3$	3250	205	78.8	0.51

3.3 Photon Echo Experiments

A typical photon echo experiment involves 3 pulses (c.f. Figure 2-4). The three pulses interact with the sample in a sequence. Based on different designs, there are several ways to arrange the 3 beams in collinear or non-collinear geometry.

In collinear geometries, the two or three pulses travel collinearly and their relative delay is changed by a pulse shaper [67-69] or by an interferometer [70]. The photon echo signal is selected by phase cycling and Fourier transform.

The non-collinear design, also known as photon echo configuration in box-car geometry, sets all the three beams in different directions and the signals come out in their own phase-matched direction, i.e. they are spatially separated [71, 72]. The echo signal is detected in the direction $-k_1+k_2+k_3$. A fourth beam travels along the same direction and interferes with the signal in order to record the amplitude and phase information of the signal. The interference amplifies the signal and therefore greatly enhances the sensitivity of the measurement. In this design, all the four pulses can be manipulated arbitrarily, which gives a great flexibility in experiments. However, the spatial overlaps of four pulses are hard to achieve since mid-IR is invisible to human eye and can only be measured with slow and bulky detector. Moreover, when the four beams are split off by several beam splitters, the phase instabilities, caused by the fluctuation of the optics or the delay stage, can result in fake signals or distortions of the peaks [73, 74]. Therefore people have developed several ways to compensate the phase jittering passively or actively [73, 75].

3.3.1 Optical Setup

The photon-echo setup is depicted in Figure 3-4. The incoming beam is first split by a 50/50 beam splitter. The transmitted and reflected beams are collimated in the horizontal plane and have a distance of 10 mm from each other. A 90º off-axis parabolic mirror with a focal length of 100 mm is used to focus them on a Diffractive Optics Element (DOE), i.e., an optical grating, which diffracts the light in vertical direction as the grooves are in horizontal direction. The DOE is designed to diffract highest intensity, i.e. 20%, into the two first-order beams. The diffraction angle is 2.2 degree for 3μm wavelength, which means the angle between the two first order beams is 4.4 degree. The diffracted light is re-collimatted by a second parabolic mirror which is identical to the first one. Since the defocusing and diffraction take place at the same point, the divergence of the beams themselves and between the beams is corrected simultaneously. These four first-order beams pass through a mask, while all the other unwanted orders are blocked. The four beams are given the box-car geometry, shown in the lower right corner of Figure 3-4. The two beams transmitted through the beam splitter serve as a phase-locked pulse pair, referred to as $\mathbf{k}_1$ and $\mathbf{k}_2$, and the two reflected beams serve as a phase-locked pulse pair, referred to as $\mathbf{k}_3$ and $\mathbf{k}_{LO}$. This geometry

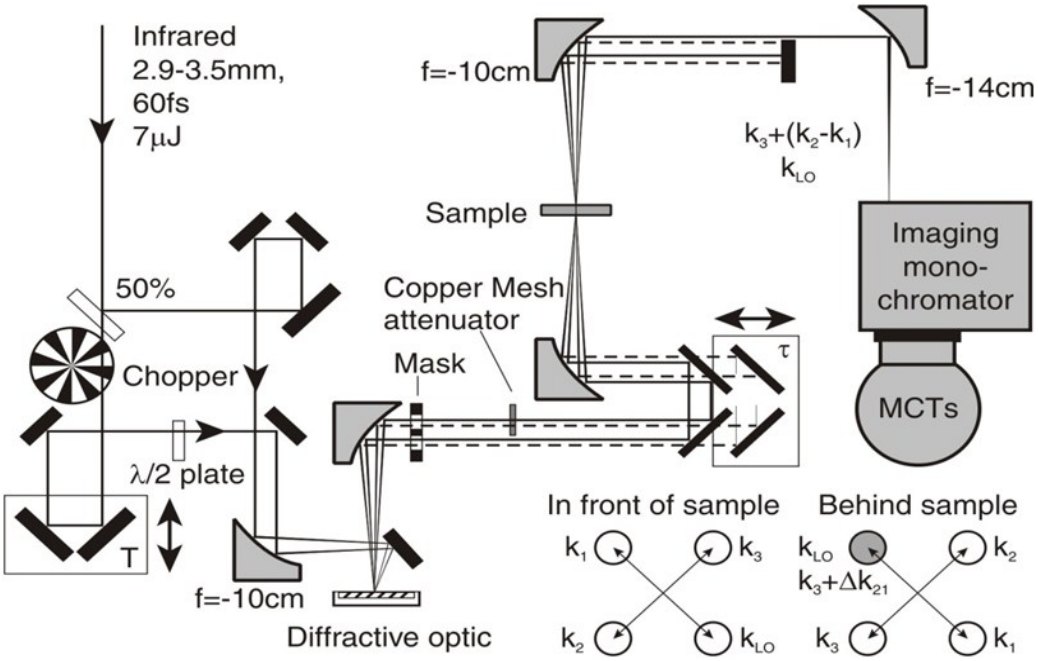

Figure 3-4: The design of photon echo setup. The mid-IR is split first by a beamsplitter, and then the two beams are split by the diffractive optics into two phase locked pulse pairs. The three beams are focused on the sample to generate photon-echo signal, and the fourth one interfere with the echo signal. On the lower right part is the boxcar geometry of pulses, displayed as the observer facing the direction from which the light come. The vector of the grating $\Delta k_{21}=k_2-k_1$.

guarantees that the emitted signal $\mathbf{k}_{sig}=-\mathbf{k}_1+\mathbf{k}_2+\mathbf{k}_3$ propagates along the same direction as $\mathbf{k}_{LO}$. On the second delay stage, the four beams are divided into two groups, upper two and lower two, and reflected by two pairs of mirrors. Then two 90º off-axis parabolic mirrors are used to build a one-to-one imaging system, and focus all the four beams into a 100μm spot. After the imaging system, the re-collimated beam of $\mathbf{k}_{LO}$ is focused by a parabolic mirror into the slit of a monochromator with $\mathbf{k}_{sig}$. The spectrum of the local oscillator together with the signal is recorded by a 16-pixel HgCdTe detector array with a spectral resolution of 8 cm^{-1} at 3μm. Since the spectral window for a fixed grating position is only around 100cm^{-1} wide, being much narrower than the spectral bandwidth of the pulse, the grating of monochromator is rotated in steps to cover the whole spectrum.

According to basic properties of a Fourier transform, the bandwidth 8 cm^{-1} corresponds to a time period of 1.8 picoseconds which is larger than the typical time difference between signal and local oscillator. Consequently, they interfere with each other on the detector array, i.e. the detector records the interferegram of the two electric fields.

The heterodyne-detected signal depends on the phase different Δφ between $\mathbf{k}_{LO}$ and $\mathbf{k}_{sig}$. Therefore, the phase stability is of much importance for the quality of the data. Instead of

active phase stabilization, this setup can stabilize the phase in a passive way. The relative phase Δφ measured by the detector depends on $\mathbf{k}_{LO}$- $\mathbf{k}_{sig}$ = $\mathbf{k}_{LO}$-(-$\mathbf{k}_1$+$\mathbf{k}_2$+$\mathbf{k}_3$) = ($\mathbf{k}_{LO}$-$\mathbf{k}_2$)-($\mathbf{k}_1$-$\mathbf{k}_3$) =($\mathbf{k}_{LO}$-$\mathbf{k}_3$)-($\mathbf{k}_1$-$\mathbf{k}_2$). On all optical components in the setup there are two or four incident beams. This leads to that each beam always hits optics together with another beam which has a negative sign of the k-vector. For example $\mathbf{k}_1$ accompanies $\mathbf{k}_2$ while $\mathbf{k}_3$ accompanies $\mathbf{k}_{LO}$ until they arrive the mirror pairs, since which $\mathbf{k}_1$ travels together with $\mathbf{k}_3$ and $\mathbf{k}_2$ goes with $\mathbf{k}_{LO}$. Mechanical fluctuations affecting pairs of beams and the phase instabilities of one beam are canceled by the accompanying beam with different sign. Therefore, a phase stability better than λ/150 is secured.

A chopper is placed in the way of transmitted beam by the beam splitter, and runs at the frequency 500Hz. The recorded spectrum of the local oscillator is alternatively taken with and without signal. The difference of two spectra, which are represented by I_{pump} when the light is unblocked and I_{unpump} when the light is blocked, is given by:

$$I = I_{pump} - I_{unpump} = \left|E_{LO} + E_{sig}\right|^2 - |E_{LO}|^2 = \left|E_{sig}\right|^2 + 2\mathrm{Re}\left(E_{LO}E_{sig}\right)$$
$$= {E_{sig}}^2 + 2E_{LO}E_{sig}cos\phi \qquad (3.6)$$

where the $\mathbf{E}_{LO}=E_{LO}e^{-i\omega t}$ and $\mathbf{E}_{sig}=E_{sig}e^{-i\omega t}$ represent the electric field of local oscillator and signal, and ϕ is the phase difference between them. The signal is given by the third-order signal, and eliminates the intensity of the local oscillator itself and stray light of $\mathbf{k}_3$. However, the scattered light from the beams $\mathbf{k}_1$ and $\mathbf{k}_2$ can still play a role. Thus, searching for a position on the sample where light is less scattered is still very important in the experiment.

To advance the k_{LO} relatively to the interaction, a 0.5mm CaF_2 window is inserted into $\mathbf{k}_3$ to retard the signal, which is generated when the $\mathbf{k}_3$ arrives in the sample. In the meantime, $\mathbf{k}_{LO}$ is attenuated into 2% by copper meshes to reduce unexpected excitation which could potentially affect the interactions of the sample with other three pulses. A delay stage is used to change the delay of transmission of beam splitter, namely the time difference between pulse pair $\mathbf{k}_1$, $\mathbf{k}_2$ and pulse $\mathbf{k}_3$. A mirror pair which reflects $\mathbf{k}_2$ and $\mathbf{k}_{LO}$ is mounted on a second delay stage, therefore the time difference of k_1 and k_2 is adjustable. Assuming the delay time of two delay stages are t_1 and t_2 respectively, the coherence time τ and population time T are t_2 and t_1-t_2 respectively. Thus, two delay stages should be moved simultaneously when we scan the coherence time. The time difference between $\mathbf{k}_{LO}$ and $\mathbf{k}_3$ is about $-t_2$+700 fs, i.e., the time difference between the local oscillator and the rephasing signal is fixed around 700 fs, since

the 0.5 mm CaF_2 can induce a time difference between $\mathbf{k}_3$ and $\mathbf{k}_{LO}$ for around 700 fs. The $\mathbf{k}_{LO}$ can arrive after the $\mathbf{k}_1$ when $t_1+t_2>700$ fsor even after $\mathbf{k}_2$ when $t_2>700$ fs. This will cause a signal of $\mathbf{k}_1$ or $\mathbf{k}_2$ pumps, $\mathbf{k}_{LO}$ probes on top of the interferegram. This pump probe signal can be filtered out during the data processing afterwards, which will be discussed in section 3.3.3. In the meantime, the intensity of local oscillator changed by the pump probe signal is negligible due to the signal being less than 20 mOD mostly in our systems, meaning it decreases less than 2%.

3.3.2 Coherence Time Scan

There are two Fourier transforms in a 2D measurement; each transfers one coherence evolution of the system from the time domain into the frequency domain. The FT generating the detection frequency by converting the second coherence evolution is done by the monochromator and the local oscillator, which disperse the broad spectrum onto the detector array to record the frequency-resolved amplitude and phase. The FT of the first coherence evolution is done after scanning the coherence time τ.

In the pump-probe measurement as we discussed in section 2.5, the resulting absorptive signal is the sum of both phase matched processes $-\mathbf{k}_1+\mathbf{k}_2+\mathbf{k}_3$ and $+\mathbf{k}_1-\mathbf{k}_2+\mathbf{k}_3$. Similarly, the absorptive 2D signal consists of the rephasing signal emitted into the direction $-\mathbf{k}_1+\mathbf{k}_2+\mathbf{k}_3$, and the non-rephasing signal, $+\mathbf{k}_1-\mathbf{k}_2+\mathbf{k}_3$. In the non-collinear geometry, the rephasing signal and non-rephasing signal propagate non-collinearly along their own wave vector directions. It would require more hardware, and more local oscillator to measure them simultaneously.

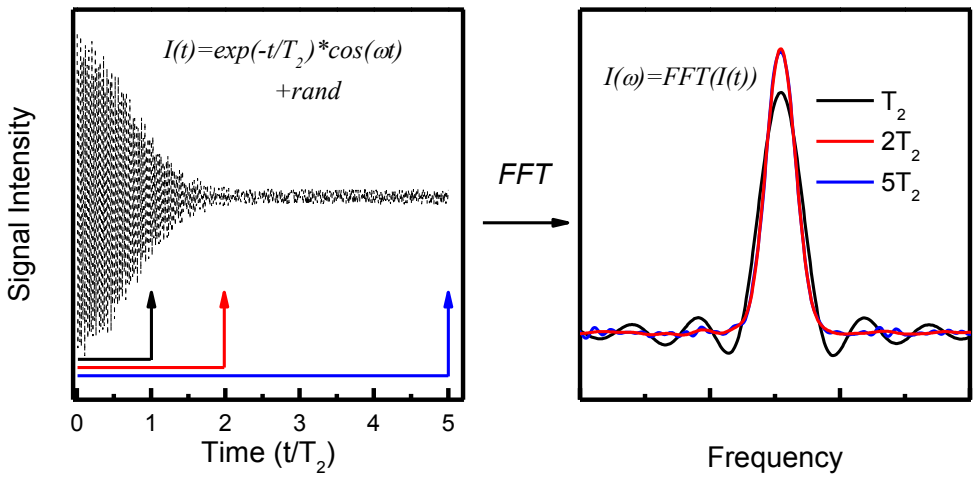

Figure 3-5: A numerical simulation of the exponential decay of oscillating and its FFT result. The random noise is considered being evenly spread in time. The FFTs were done with three time range, covering T_2, $2T_2$ and $5T_2$. The arrows in left panel show the time ranges being transformed and the right panel shows the results of FFT.

Therefore, we put our detector at the direction, along which the rephasing signal $-\mathbf{k}_1+\mathbf{k}_2+\mathbf{k}_3$ propagate. When we reverse the time order of $\mathbf{k}_1$ and $\mathbf{k}_2$ during measurement to measure $+\mathbf{k}_2-\mathbf{k}_1+\mathbf{k}_3$, the non-rephasing signal is recorded.

The scan range of the coherence time has to be matched to the dephasing time of the system. As discussed in section 2.5, the second pulse scans over the dephasing of the oscillating superposition of coherences which are excited by the first pulse. For a FT method, the longer the time has been scanned, the higher the frequency resolution will be. However, when the coherence time scan is too much longer than the dephasing time T_2, the noise will get too much involved and, thus, lowers the signal-to-noise ratio. When the scanned coherence time is not as long as the dephasing time, the measured dephasing process is truncated. This truncation will broaden the band in the FT as a result of lower time resolution, and also generate small side bands. A numerical simulation of the Fast Fourier Transforms (FFT) of different time ranges is presented in Figure 3-5. The oscillation curves on the left decays with a time constant T_2, with the noise being a time-independent additive random number. The FFT is done from three different time ranges, all of which start from t=0 but end at different moments. The shortest time range ends when $t=T_2$ corresponding to the black arrow in left panel and the longest time range ends when $t=5T_2$ corresponding to the blue arrow in the plot. From the oscillation it is clear that the shortest range does not cover the whole decay and the longest one covers far more than the decay. In contrast, the time range of the third FFT ends at $t=2T_2$, after the oscillation has decayed to most extent, corresponding to the red arrow. After the FFT, the black curve, which is the result for the FFT of T_2, turns out to be a broader peak with oscillating side bands on both sides. The FFTs of $2T_2$ and $5T_2$ give almost identical main peak, in terms of amplitude and bandwidth, pointing to the absence of truncation effect. However, the FFT of $5T_2$ appear to be noisier because of the unnecessary noise collected from $2T_2$ to $5T_2$. Therefore, it is critical to choose a suitable scan range to produce a non-misleading plot.

3.3.3 Phase and Amplitude Retrieval

The data set after one measurement is a collection of interferegrams between signal and local oscillator at different coherence times. Each interferegram contains the desired information such as the relative phase of the signal to the local oscillator and the amplitude of signal mixed with the useless information such as the amplitude of the local oscillator, the stray light, and the pump probe signal mentioned in section 3.3.1. It is given by equation (3.6) in

frequency domain. When we assume that the intensity of the signal is significantly smaller than that of the local oscillator, then detected signal can be simplified to be

$$S(\tau,\omega) = 2E_{LO}(\tau,\omega)E_{sig}(\tau,\omega)cos\phi = f(\tau,\omega)\exp(i\phi) + f(\tau,\omega)\exp(-i\phi) \qquad (3.7)$$

Here $f(\omega) = E_{LO}(\omega)E_{sig}(\omega)$. In order to extract the useful information and build a 2D plot, the data processing method shown in Figure 3-6 is applied as proposed by Lepetit and his coworkers [76].

The interferegram in the frequency domain is first converted into the time domain by an inverse Fourier transform,

$$F^{-1}S(\omega) = f(t-\Delta t) + f(t+\Delta t) \qquad (3.8)$$

Here $\Delta t=\phi/\omega$ is the time difference between the local oscillator and the signal. Since the $f(\omega)$ is a symmetric function, so is $f(t)$ and $F^{-1}S(\omega)$. The equation (3.8) shows that there are two pulses symmetric about the time zero defined by the local oscillator pulse, since the interferegram gives only time difference between different components not time sequence. A Heaviside function $\Theta(t)$ is multiplied with the Fourier Transformed signal to single out the relevant term $f(t-\Delta t)$ alone and suppress the stray light or pump probe signal which are located at different positions in the time domain. The filtered signal is converted back to frequency domain by a Fourier transform and we obtain

$$f(t-\Delta t) = F[\Theta(t)F^{-1}S(\omega)] = E_{LO}(\omega)E_{sig}(\omega)\exp(i\omega\Delta t) \qquad (3.9)$$

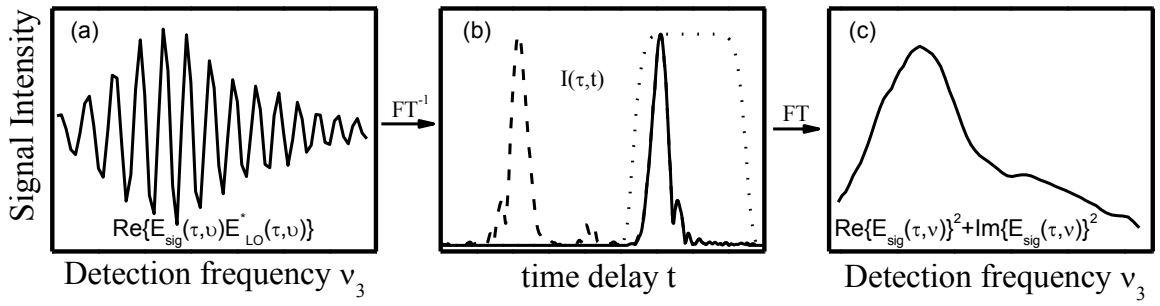

Figure 3-6: Illustration of data process. The recorded intereferegram (panel a) is inverse Fourier transformed to time domain first, then the useless signal (dash line in panel b) are filtered out by a super Gaussian function (dots line in panel b). The signal (solid line in panel b) is Fourier transofrmed to frequency domain to be a complex electric field E_{sig} of signal when we know the electric field of local oscillator E_{LO}.

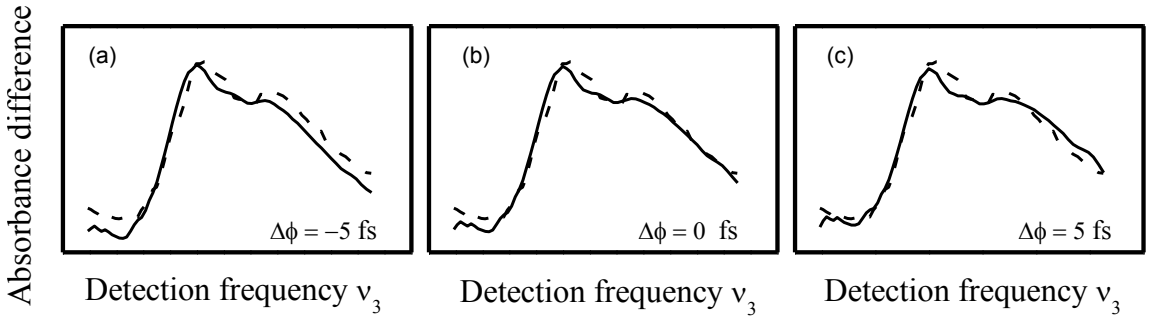

Figure 3-7: The comparison of pump probe signal (solid line) with real part of integral (dashed line) along excitation frequency with different phase. The relative phase is scaled as the time difference between signal and local oscillator as shown in the lower right corner of the panels. The integrated area of the absorbance change is normalized for pump probe and 2D spectra for better comparison.

In order to obtain the pure signal $E_{sig}(\omega)$, the amplification of the local oscillator during the interference should be corrected by dividing the final signal by the electric field of the local oscillator. The absorption of sample should be considered as well, thus the transmission ratio of the sample is also employed to divide the signal. The Fourier transformed result is regarded as the complex field of the emitted signal after the third pulse, which consists of non-rephasing and rephrasing signal. Ideally, according to (3.9) we can determine the phase of the signal by multiplying it with $\exp(-i\omega\Delta t)$. However, the phase of this complex field is not always accurately known. First, the measured signal contains only phase difference between the local oscillator and the signal, and, therefore, an implicit assumption is made that the phase of the local oscillator is proportional to the frequency over its bandwidth, i.e. $\varphi_{LO}=2\pi\nu t$. Secondly, the relative phase difference cannot be decided very accurately. Thus, an additional pump-probe measurement is introduced to "phase" the complex field. The real part of the absorptive 2D spectrum projected on the axis υ_3 is regarded as equivalent to the pump-probe signal with the pump probe pulse delay equal T, as long as all the contributions to the stimulated vibrational echo are absorptive [45, 77]. Consequently the complex 2D spectrum is integrated along the excitation frequency axis, and the real part of the integral is fit to the pump probe signal by varying the phase of the complex field. A comparison with different phases is shown in Figure 3-7. The phase is valid for all the signals with different coherence times. In this way the detection frequency is derived.

By doing a Fourier transform along the coherence time, the excitation frequency is resolved. To compensate the effect of the spectral envelope of the pulses, the electric field of the pulses are divided one time along detection frequency axis and two times along excitation frequency axis. It should be noted that this procedure is only valid when the pulses are transform limited

and the phase of the pulse is supposed to be proportional to the frequency. The final result of this procedure is the 2D spectrum, which shows frequency-frequency correlations.

3.4 Pump Probe Experiments

The pump probe measurements are done on the same setup as the photon echo. Instead of 4 beams in the PE, pump probe measurements include only two. Therefore, the two lower beams in PE, i.e. $\mathbf{k}_2$ and $\mathbf{k}_{LO}$, are blocked. The upper beam $\mathbf{k}_1$ serves as the pump and $\mathbf{k}_3$ is attenuated down to 4% to serve as the probe. The transmission absorbance change is

$$\Delta A(T,\omega) = -\log\left(\frac{I(T,\omega)}{I_0(\omega)}\right). \tag{3.10}$$

The lack of a reference requires a stable pulse and signal averaging over many scans. Compared to 2D IR experiment, a pump-probe measurement needs less time to achieve a frequency-resolved signal for a certain amount pump and probe pulse delay times, which corresponds to the population times in 2D-IR experiment. The excitation frequency is not resolved because the first two interactions occur at the same time (τ=0). This technique enables us to investigate the system over a longer population times than 2D-IR measurements with an expense of reasonable measurement time. While it takes 8 hours or more to measure 13 2D plots with different population time up to 1.5 ps, a pump-probe measurement up to 100 ps with more than 250 different pump probe pulse delays needs less than 3 hours.

4. Ultrafast Vibrational Dynamics of Hydrated DNA

The structure of DNA has been studied for a long time, for its important role in storing the genetic information with which life can pass on. In 1953, Watson and Crick proposed a double helix structure based on their x-ray diffraction results [4], which is generally accepted as the first correct model. In his model, the DNA molecule is like a long twisted ladder (see Figure 4-1), the stringers of which is made of phosphate groups and five-carbon sugars (2-deoxyriboses) and called backbone, and the steps of which consist of complementary base pairs (adenine-thymine, AT, and guanine-cytosine, GC).

In the double helix, each base pair is integrated by hydrogen bonds to form Watson-Crick (WC) geometry, as shown in Figure 4-1. For AT base pair, both bases donate one hydrogen atom, forming two hydrogen bonds in between. For GC base pair, three hydrogen bonds are involved since guanine donates two hydrogen atoms and cytosine donates one. However, in the gas phase or the solution, where no backbone or other groups help to stabilize any special geometry, they can also form dimers in variable geometries, such as Watson-Crick, inverse Watson-Crick when one base is flipped for 180º, Hoogsteen and inverse Hoogsteen when different groups from bases participate in the bonds. Generally, the extra bond of GC base pairs makes Watson-Crick geometry more stable and favored in such situation, while AT base

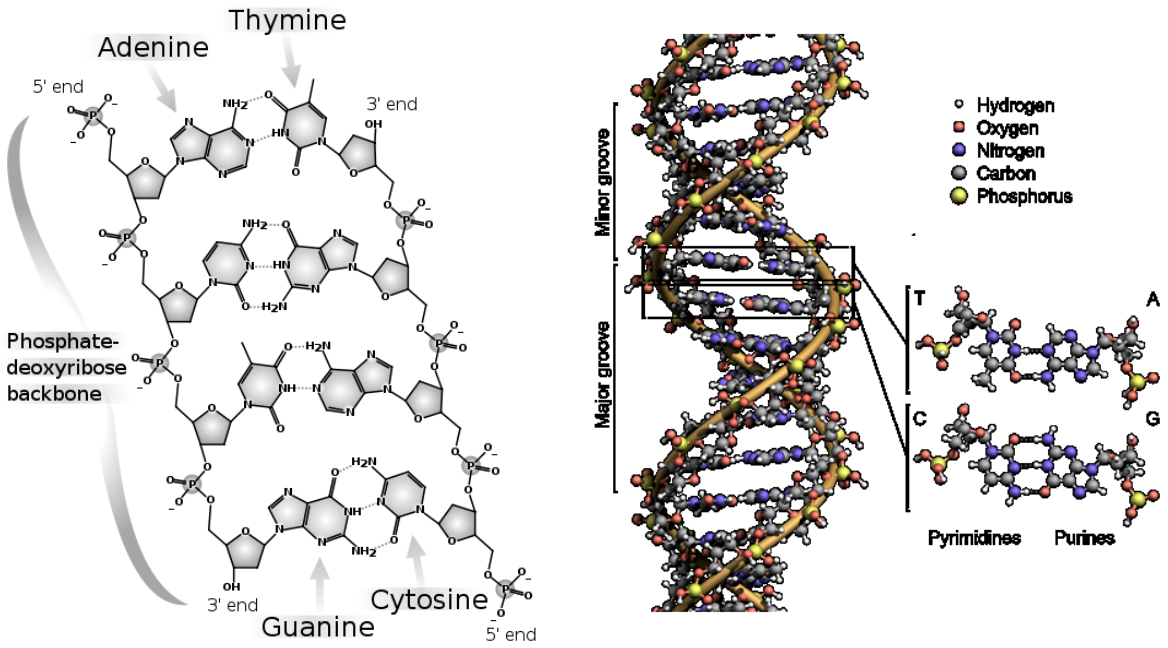

Figure 4-1: Chemical structure of DNA (left) and the structure of DNA double helix and Watson-crick geometry of two kinds of nucleobase pairs (right). The dots between bases are the hydrogen-bonds.

pairs are more flexible.

The three dimensional structure of the double helix, a form that DNA chain generally persist, was presented in Figure 1-1. It has been shown that there are many parameters, related to the structure of the DNA, such as the angle between the base pairs and the backbone, the width of the major and minor grooves, which are spaces along the helix axis between the two strands, and the direction of the twisting. Based on these parameters, the structure of DNA is classified in several different conformations, including A-DNA, B-DNA and Z-DNA forms, among them B-DNA predominantly exists in the living organisms.

The A-DNA (Figure 4-2 left) was found by Franklin and Gosling in 1953 [10], shortly after suggestion of the B-DNA (Figure 4-2 middle) by Watson and Crick. The A-DNA is usually found in dry environment, when there are not many water molecules attached to the DNA structure. An overall picture shows that A-DNA is a right-handed antiparallel duplex, with strong base pair inclination. In contrast to A-DNA, B-DNA usually exists when there is more water attached to the DNA molecule. Accordingly, the water molecules attached to the helices change the structure to much extent, including enlarging the distance between different base pairs, diminishing the inclining of the base pairs and broadening the minor groove. The Z-DNA (Figure 4-2 right) was found in 1979 [78], much later than the A- and B-DNA, for its rare existence. Unlike the A- and B-DNA, it is a left-handed helix. In general, the conformations that the DNA adopts depend on the hydration level, as well as the DNA sequence and other parameters, and can transit into other forms [79]. For example, a DNA molecule in A form at low hydration level can transit to B form when it is fully hydrated. The

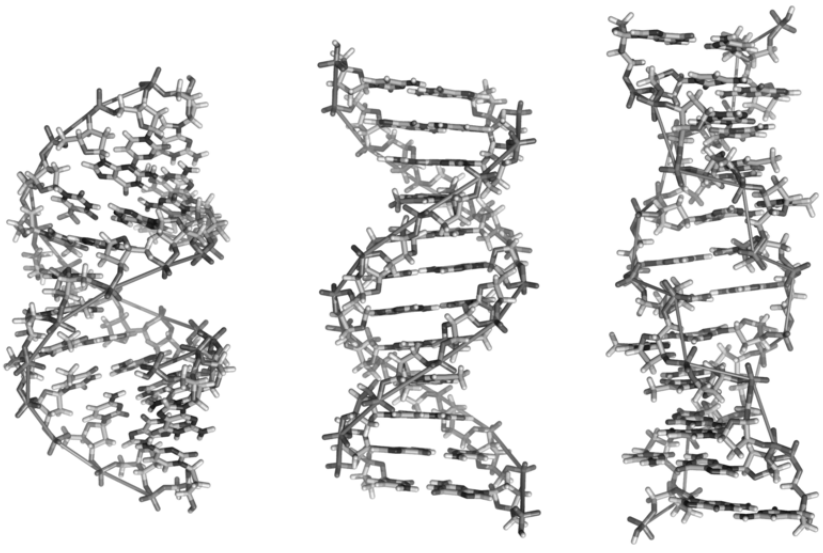

Figure 4-2: The side views of A-DNA (left), B-DNA (middle) and Z-DNA (right).

mechanical properties of the DNA, which are directly related to the structure, are significantly important for cells, since many processes need to change it. In order to study the structure of DNA, the hydrogen bonds inside base pairs as well as interactions between the DNA and the environment are investigated.

In this chapter, DNA consisting of only adenine and thymine with a well-defined structure is studied. Unlike the various patterns of adenine-thymine base pairs in solution, the geometry of base pairs are strictly limited in the DNA with double helix structure. For a small oligomer, it is also possible to control the sequence of the nucleobases [31, 32, 80]. In our study, we choose to study a double helix with Watson-Crick geometry, which is the geometry of the native DNA. Similar to the native DNA, full interactions of the ribose-phosphate backbone are included. However, it is still difficult to study DNA in water solution, due to the overlap of NH stretching in DNA bases with the strong OH stretching absoption of water. In order to overcome this problem, the water content in the sample film can be controlled [31, 81] by controlling the relative humidity of environment.

4.1 DNA Hydration

The hydration of DNA by surrounding water shells plays a defining role for the double helix geometry and is vital for basic molecular processes such as the exchange of energy between DNA and its environment [79, 82]. The interactions of ionizing radiation with biological molecules produce a variety of damage leading to observable effects such as mutation, transformation and cell death. Damage to DNA and higher-ordered structures by tracks of charged particles can be induced either by direct energy deposition or by diffusible radical species generated in water surrounding the molecule. Ionization and excitation of the hydration shell of DNA leads to the formation of radical and molecular species at picosecond time scale. Therefore, knowledge about the hydration, including the number and spatial distribution of water molecules, becomes necessary in understanding the radiation damage [12, 83].

The surface of DNA is characterized by the major and the minor groove of different width and depth. Structure units such as ionic phosphate group and sugar rings of the backbone as well as pairs of nucleic bases offer a variety of interaction sites with water molecules of the environment. Local hydrogen bonds between water molecules and the interaction sites, as well as long-range Coulomb forces determine the structure and function of the hydration

shell. At ambient temperature, fluctuations of the water structure, including the breaking and reformation of hydrogen bonds, occur on an ultrafast time scale of up to ~1 ps and cause a fluctuating electric field that gives rise to a dephasing of vibrational excitation and influences the vibrational relaxation [84-86].

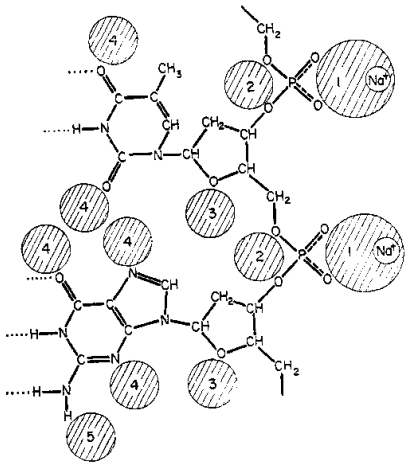

Figure 4-3: Schematic picture of DNA helix with the number noting the sites where water can attach in a preferring order. (plots extracted from Ref. 87)

In the 1960's Falk et al. proposed a scheme of DNA hydration consisting of two hydration shells, based on a serial of gravimetric and infrared spectral studies concerning the finger print range and the OH stretching range [87, 88] for a native DNA sample in different relative humidities (R.H.). The first hydration shell is presented in Figure 4-3. At 0% R.H., there are only 2 water molecules per base pair, which are attached to the ionic phosphate groups and the sodium ions (site "1") due to their high affinity for water molecules. With increasing relative humidity, the water first completes the first hydration shell around the phosphate group, which contains 5-6 water molecules at 65% R.H., and then starts to approach the base pairs in the DNA double helix. Note that each site can contain more than one water molecule and conversely each water molecule may belong to more than one hydration site. The oxygen atoms on P-O-C groups between phosphate group and the deoxyribose rings (site "2") and C-O-C group of the rings (site "3") may also become hydrated below 60% R.H., and more when relative humidity increases from 60% to 80%. The –N, NH, and C=O (site "4" and "5") are not hydrated until the R.H reaches 65%. All the hydration sites are occupied when R.H. is 80%, beyond which the water molecules mainly go to the "empty space" between molecules and push them apart, meaning that the water molecules are no longer attached directly to the DNA bases but to the already existed water molecules and form the second hydration shell. Finally in the 92% R.H. there are on average more than 20 water molecules per base pair. Apart from the first hydration layer, the adsorbed water molecules are similar to liquid water.

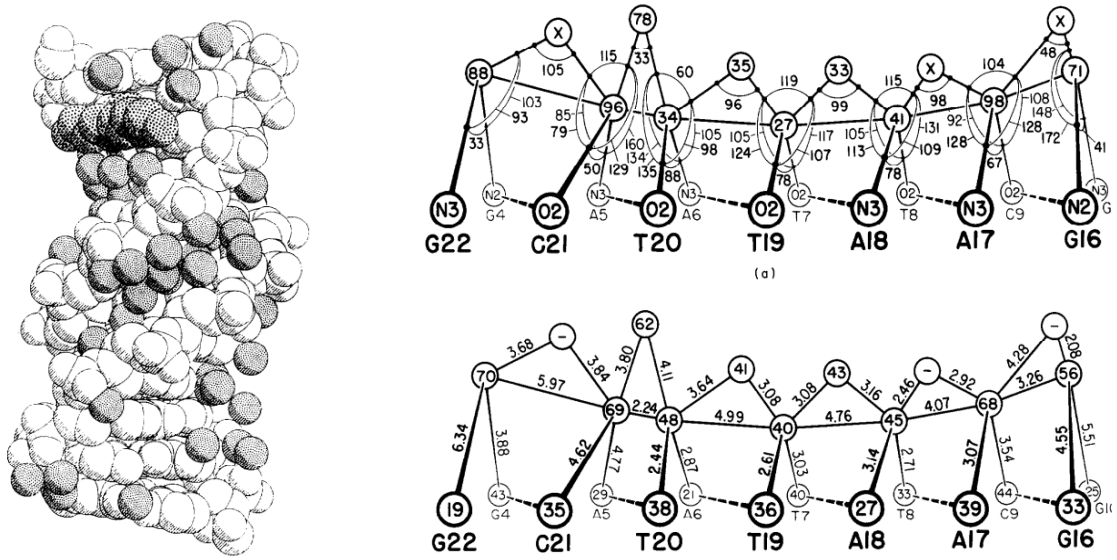

Figure 4-4: Left: The space-filling drawing of the dodecamer and its associated solvent molecules. The water molecules in the middle (shown as finely shaded sphere) are attached to the minor groove of DNA. Right: unrolled view of the spine or backbone of water molecules that curve down the minor groove. Spheres from the bottom are atoms from the paired bases, and the other spheres are oxygen atoms from water molecules. (figures extracted from Ref. 11)

In Falk's later work in 1970 [81], the difference spectra between different R.H. were taken. It turns out that the hydrogen bond strength between OHs in the DNA-water system is similarly distributed as in liquid water for the very similar redshift of OH stretches presented upon formation of hydrogen bonding, regardless of the hydration level. It should be noted here, that the difference spectra only showed the spectra of water molecules, which attach to the DNA when the hydration levels increased, excluding the residue water that cannot be removed. However, when temperature was decreased, crystalized water appeared only in the sample with more than 13 water molecules per base pair which corresponds to R.H. 86%. It again suggested that the first hydration shell has properties markedly different from those of bulk water while the outer layer behaves very similarly to bulk water. The study was conveyed with stationary IR spectra, so fluctuations of the water molecules, finite hydrogen bond life times and exchange processes between the primary and secondary hydration shell are neglected.

More geometry information was obtained from stationary X-ray diffraction pattern recorded with dodecamer C-G-C-G-A-A-T-T-C-G-C-G crystallizes as slightly more than one full turn of B-DNA at cryogenic temperature [11, 89]. The positions of water molecules were mapped via the time-averaged electronic charge density of oxygen atoms. They found a zig-zag chain of water molecules extending across the minor groove of the adenine-thymine base pairs, which they named as 'spine of water' (Figure 4-4). The 'spine of water' plays an important

role in stabilizing the B conformation of the helix. On the other hand, the water molecules here bridge the major groove in an irregular manner.

With the method ‘hydrated building block’ [90], Berman and her group confirmed the existence of ‘spine of water’ and demonstrated that the hydration for GC and AT pairs is similar in crystals. The number of first hydration shell is estimated to be 17 water molecules per nucleotide pair with extra water forming a disordered and highly mobile part of the hydration shell of B-DNA [91]. Both bases and phosphate groups have significantly organized hydration shells. The extent of hydration is larger and has higher priority around phosphates, but highly mobilized [92].

However, the water shell around the DNA group is not static, but undergoes permanent fluctuation in different time scales. While x-ray diffraction focuses on the time-averaged distribution of water molecules around crystallized DNA, nuclear magnetic resonance (NMR) was used to investigate the resident and reorientation times of water molecules interacting with DNA [93-96]. The fast reorientation time of the water molecules about the hydrogen bond axis is found to be between 0.5 ns and 10 ns, orders of magnitude slower than the bulk water [96]. The residence time of the molecules becomes longer for the increased order of the hydration water, and the residence time of the water molecules in major groove is less than 500 ps compared to over 1 ns for those in minor groove, pointing to their high mobility [95], but still much slower than in bulk water.. More recent researches [97] suggested a similar residence time for water molecules in the major and minor groove.

Interested in the geometries and dynamics of water molecules around DNA, molecular dynamics (MD) calculations were done on short DNA sequences in solution on time scale of a few nanoseconds [98, 99]. The major features observed in X-ray diffraction measurements, such as “spine of water” in minor groove, were reproduced [98]. Calculations on a 10 ns time scale give average life time of hydrogen bonds of the order of 10 ps with maximum value around 200 ps [99]. When considering the water molecules hydrogen-bonded to DNA, i.e., distances between the water molecule and the DNA non-exchangeable protons are less than 0.35 nm, the average residence time increased to 100 ps with maximum value up to 600 ps, which is consistent with the NMR experimental data [99]. A MD analysis of the hydrogen bond lifetime correlation functions (HBLTCF) of hydrogen bonds between DNA and water [100] gives multi-exponential decays with time constant from 0.5 to 115 ps, pointing to different types of water molecules bounded to DNA. The lifetimes of water attaching to the

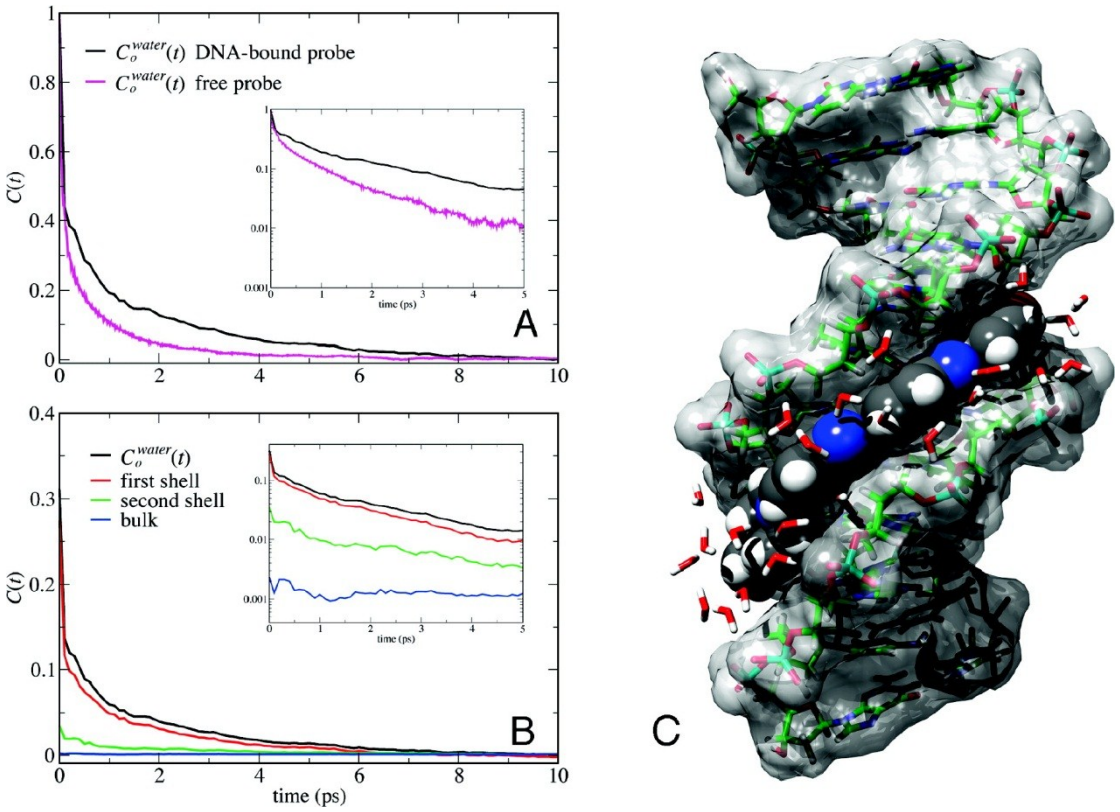

Figure 4-5: The water response. (A) Comparison of $C_0^{water}(t)$ for the probe bound to DNA (black) and free in aqueous solution (magenta). (B) Spatial decomposition of $C_0^{water}(t)$ for the DNA-bound probe into contributions from the first and second solvation shells of the probe and bulk water (defined as water molecules beyond the second shell of the probe). (C) DNA structure with the probe shown as the black, white and blue spheres and the first hydration shell. (figures taken from Ref. 107)

bases in minor groove turn to be longer than those in major groove by a factor of 2, both much longer than the water attached to the phosphate group.

Recently, the ultrafast dynamics of DNA and the water molecules around it were studied by nonlinear spectroscopy. Time-resolved Stokes shift (TRSS) is used to investigate short DNA fragments in aqueous environment with drugs attaching to the minor groove as probe or oligonucleotides in which a native base pair is replaced by a dye molecule as probe [101-103]. The basic approach is to electronically excite the probe, inducing a subsequent reorientation of the polar surroundings to lower the energy of the electronically excited state. This process is known as the solvation process, containing the information of interactions between the probe and surrounding solvent molecules, and can be measured through the time-dependent Stokes shift of the fluorescence emitted by the probe. Therefore, a combinative system surrounding the probe consisting of DNA, counterions and attached water molecules is under investigation (Figure 4-5 right). In a linear response approximation, two-point frequency-time correlation functions (TCF) have been derived from the transient Stokes shift and compared to the results for the same chromophore in bulk water. Their results showed that TCFs of

different DNA/chromophore systems decay on a slower time scale than TCFs of the same chromophore in water (Figure 4-5 top-left). Some simulations of TRSS experiment [103-107] have also been done and a highly complex multi-exponential behavior covering orders of magnitude in time is observed. Because of the long-range character of the underlying electrostatic (dipole) interactions between the probe and its environment, including water shell and DNA, such TCFs represent the combined dynamics of the different constituents of the system, i.e., the DNA structure, in particular its charged groups, the counterions of DNA, and the water shell. While a selective extraction of the water response is difficult, such behavior has been interpreted as a slowing-down of water reorientation dynamics at the surface of DNA and proteins, with the assumption that the inserted chromophore does not change the properties of the DNA structure. This interpretation was not supported by others [108] and has been challenged by recent ^{17}O NMR relaxation studies of proteins [109].

Another class of experiments makes use of femtosecond vibrational spectroscopy, in particular, 2D-IR spectroscopy, in which vibrational excitations serve as probes of molecular interactions and dynamics in the electronic ground state. Selecting particular vibrations of DNA or water, molecular couplings, and ultrafast processes in the macromolecular structure and the hydration shell can be separated. So far, femtosecond pump-probe experiments and 2D infrared spectroscopy of DNA have concentrated on base pair vibrations, that is, modes in the fingerprint range and NH stretching modes [31, 32, 110, 111]. Recently, the interactions between phosphate group in the DNA backbone and the surrounding water shells were studied by ultrafast vibrational spectroscopy with femtosecond time resolution [112, 113]. The asymmetric $(PO_2)^-$ vibration which displays a vibrational lifetime of 340 fs was used as the probe for the interaction. This study showed that the water shell serves as an efficient sink of vibrational excess energy with energy transfer from phosphate group to the water environment within subpicosecond time scale. Excitation of OH stretching vibrations of water molecules results in a formation of vibrational hot ground state, thus the shift of asymmetric $(PO_2)^-$ reflects the weakening or broken of hydrogen bonds between water molecules and phosphate groups.

Beyond the existing knowledge reviewed above, a number of important issues of DNA hydration remain unclear, such as the fast interactions between water molecules and bases in major or minor grooves on a femtosecond time scale. Such information can tell the influence of interactions between NH groups and their environments, such as OH groups of the water shell, on the lineshape of the NH stretching modes. Moreover, the dynamical properties of the

highly heterogeneous water shell around DNA are highly related to the structural fluctuation and energy transfer within the water shell, which are in the femtosecond time domain. OH stretching vibrations of water molecules, which undergo spectral diffusion caused by fluctuation of DNA/water system, serve as very sensitive probe for these behaviors. With 2D FT spectroscopy, we can study the lineshape of vibrations and measure directly the spectral diffusion in femtosecond time scale.

In this chapter, we will discuss results from nonlinear 2D infrared spectroscopy of DNA oligomers at different relative humidities. The experiments on low humidity samples, where few water molecules are present, give insight into the NH lineshapes and energy transfer between different NH stretching modes. The results from high humidity sample give extra information about the dynamics of OH stretches of water molecules.

4.2 Experimental

Sample preparation: The system studied here is a short DNA double helix containing 23 alternating adenine-thymine base pairs; the sequence of the nucleobases is shown in Figure 4-6 (a). In this well-defined short DNA fragment, the base pairs are in Watson-Crick geometry [32, 112, 113]. The DNA oligomer was synthesized by Thermo Scientific (HPLC/desalted). In order to produce thin film with high optical quality, the sodium counterions were replaced by surfactant molecules, cetylmethyl-ammonium chloride (CTMA) [114-116], which form complexes with DNA. The DNA-CTMA complexes then were dissolved in *tert*-butanol, and cast on clean 500 nm thick Si_3N_4 windows. The concentration of the DNA in the films was approximately 0.015 M. The thicknesses of films were of the order of 10 μm and varied by a factor of 2~3 depending on different experiments. The DNA samples were sealed in a home-built stainless steel sample cell, which consists of two chambers connected with a channel; one chamber held the humidity agent to control the relative humidity of air and the DNA sample in other chamber. The agents we used to obtain 0, 33 and 92% relative humidity were P_2O_5, saturated solution of $MgCl_2$, and saturated solution of $NaBrO_3$ respectively [87]. The calibration of different relative humidity was made by measuring the shift of asymmetric stretching mode of $(PO_2)^-$ groups in the DNA backbone according to previous work, as well as the intensity of absorptive OH stretching band [32, 113]. For less distortion on the signal induced by the dispersion of sample [117], the absorbance of sample in our measurements was mostly below 0.5 OD.

As was discussed in the introduction, the conformation of DNA helices depends on the hydration level. X-ray diffraction has shown that DNA helices with alternating adenine-thymine base pairs exist in B-like conformations at a humidity level higher than approximately 70% RH [118, 119]. Theoretical calculations [120], x-ray diffractions [121] and infrared spectroscopy [122, 123] have suggested that adenine-thymine rich part of DNA helix adopts the B conformation for a wide humidity range and rarely undergoes conformational transitions. The frequency positions of phosphodiester backbone vibrations coupled to the sugar motions and the glycosidic bond torsion are sensitive probes of DNA conformation. In our samples, two infrared bands at 835 and 890 cm^{-1} which are characteristic for the B-geometry are observed at 92% RH. Upon reducing the water content to 33% RH, these bands undergo minor shifts of 2-3 cm^{-1}, i.e., the B-form prevails. In the whole range from 0 to 92% RH, infrared bands characteristic for the A-form of DNA at 805 and 860 cm^{-1} are absent.

2D-IR experiments: In our experiment, the OH stretching vibrations of the water molecules and the NH stretching modes of the AT base pairs serve as a direct probe of the hydration dynamics in the electronic ground state. The two vibrations are located in the same spectral range, requiring an analysis of the nonlinear vibrational response as a function of the hydration level. The excitation frequencies of the experiments were centered at 3250±10 cm^{-1}, which was in the middle of the two NH stretches as shown in Figure 4-7 (a) and Figure 4-11 or at 3400±10 cm^{-1}, which overlapped with the maximum of OH stretching of water molecules. The energy was around 7 μJ per pulse. With the spectral bandwidth being more than 250 cm^{-1}, we obtained a pulse duration around 60-70 fs according to the FROG measurements (c.f. Table 3-1). The ranges of coherence time scanning were from -600 fs to +800 fs for 0% measurements and -300 fs to +300 fs for higher humidity measurements. The measurements were done with the polarization of the k_3 and k_{LO} being parallel and perpendicular to the pulse k_1 and k_2. In our later discussions, we mainly focus on the perpendicular measurements because of better quality and the more pronounced off-diagonal peaks.

4.3 Dynamics of NH Stretching Modes

4.3.1 Results

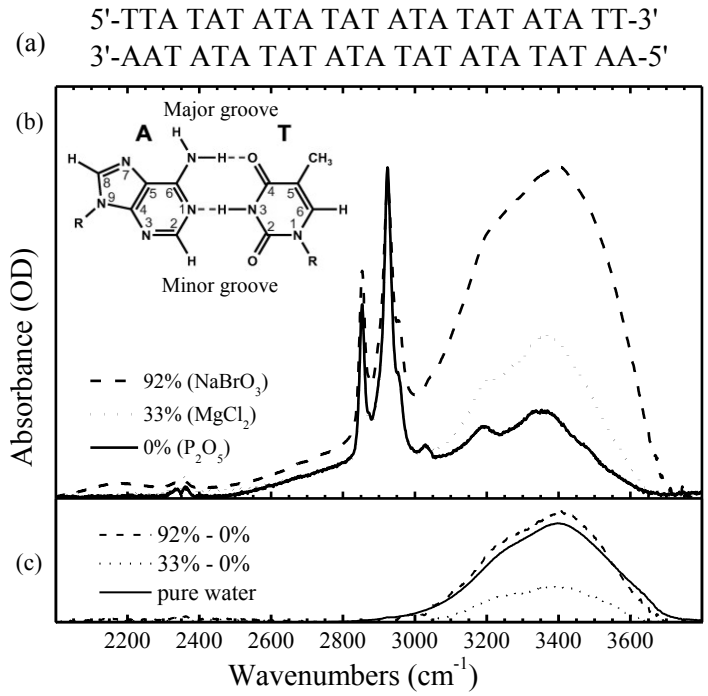

Figure 4-6: (a) Sequence of alternating AT base pairs in the double-stranded DNA oligomers we study. (b) Linear infrared absorption spectrum of a DNA thin film sample at 0% (solid), 33% (dash), and 92% (dot) R.H.. Inset: Molecular structure of the AT base pair in Watson-Crick geometry, A: adenine, T: thymine. (c) Subtraction of spectra of 0% from 92% (dot) and 33% (dash), compared with spectra of pure water (solid) which is scaled for better comparison.

The steady state absorption spectra of the sample for 0, 33 and 92% R.H. are shown in Figure 4-6. Note that the strong narrow peaks around 3000 cm^{-1} as well as the small peaks on the right side of them are the different CH stretching modes of the DNA oligomers and CTMA conterions; they remain basically unchanged under different humidity condition. The band between 3000 and 3700 cm^{-1} is due to the NH and NH_2 stretching modes of base pairs and OH stretching modes of water molecules in the hydration shell. The intensity of the bands in this range increases substantially when the water content in the sample is increased, and the overall lineshape changes as well.

At 0% R.H. there are two pronounced peaks located at 3200 and 3350 cm^{-1}, which are attributed to the NH stretching frequencies since there are only few water molecules in the sample at this hydration level. With increasing relative humidity, the weight of water molecules' contribution in the spectrum increases in unison. The most pronounced change occurs between 3000 and 3800 cm^{-1}. By subtracting the 0% R.H. spectra from 33 or 92% R.H., the difference profiles are comparable with the absorption of bulk water in terms of center frequency and width, as shown in Figure 4-6 (c). Note that the strength of the

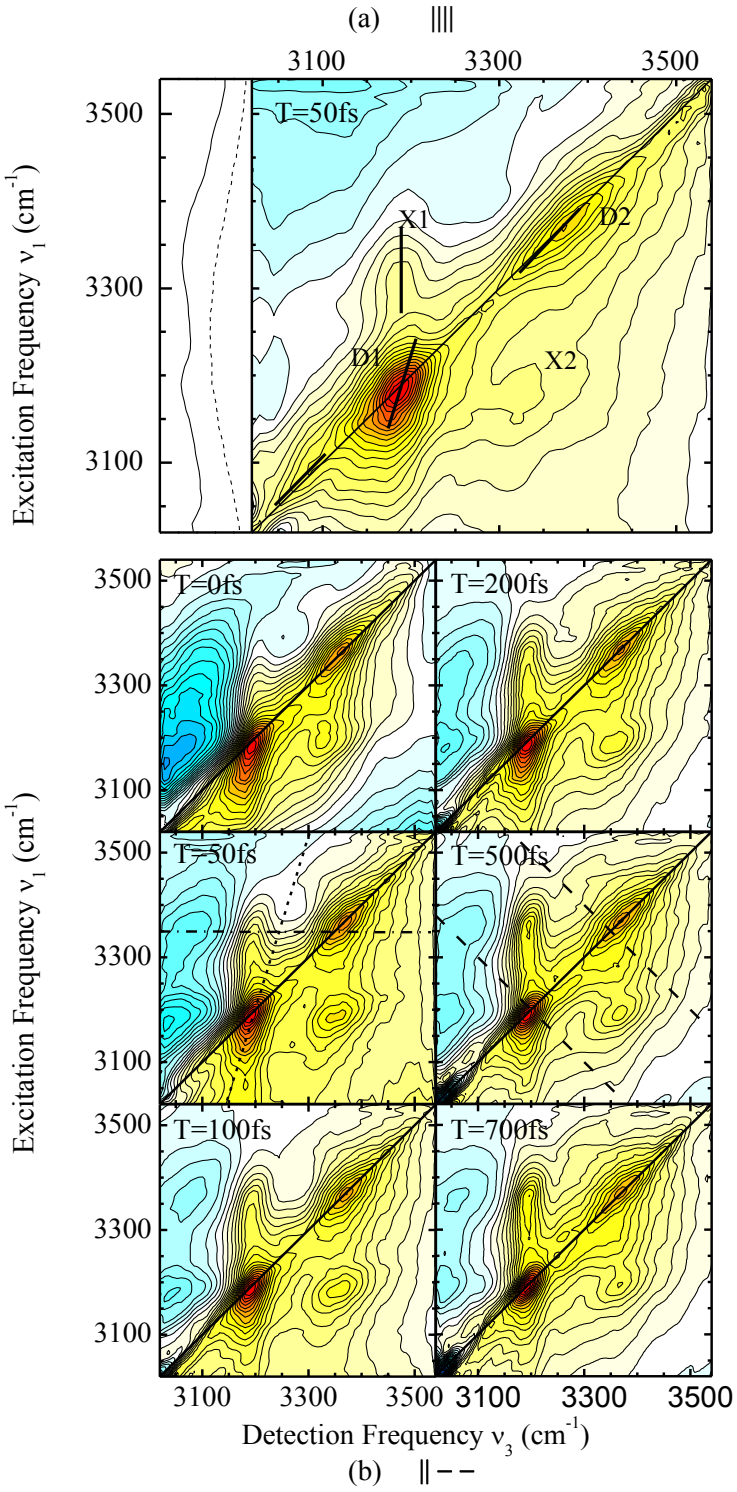

Figure 4-7: Absorptive 2D spectra as a function of population time T of the sample at R.H. 0%. (a) Parallel polarization for all four beams (||||). (b) Perpendicular polarization for k_3 and k_{LO} to k_1 and k_2 (||--). The two dimensions are excitation frequency (ordinate) and detection frequency (abscissa). Each spectrum is normalized to its maximum of positive signal and contour lines correspond to 5% changes in amplitude. The black thick lines from the left low corner to right up corner is the diagonal where $\nu_1=\nu_3$. The black solid lines in (a) are the center lines of each peak. The dash lines in (b) are the directions where cross sections in Figure 4-10 and Figure 4-12 were made along. On the left side of panel (a) is the linear absorption of the sample (solid line) and the spectrum of excitation pulse (dash line).

absorption of bulk water does not scale with the water concentration, but arbitrarily for better comparison.

This is consistent with Falk's conclusion [81], that strength of the hydrogen bonds in water shell of DNA, excluding persisting ones that cannot be removed, is comparable with that in neat water.

In order to study the NH stretching modes of the adenine-thymine base pairs, the influence of OH should be avoided. Therefore, the absorptive 2D spectra of sample at R.H. 0% were measured and shown in Figure 4-7. In panel (a) a result obtained with the polarization of the four pulses all parallel with each other (||||) and the population time T=50fs is shown. In panel (b), results obtained when k_3 and k_{LO} are perpendicular to k_1 and k_2, are shown as a function of population time T. The positive signal (yellow-red part) represents a decrease of absorbance while the negative signal (blue part) represents an increase. Regardless of the population time, there are always two obvious positive diagonal peaks located at (ν_1,ν_3)= D1 (3200, 3200) cm^{-1} and D2 (3350, 3350) cm^{-1}, and in the off-diagonal range two positive cross peaks appear at (ν_1,ν_3)= X1 (3350, 3200) cm^{-1} and X2 (3200, 3350) cm^{-1}. The shapes of these four peaks do not change much as a function of population time T. In the left part of the plots where the detection frequency ν_3 is lower than 3200 cm^{-1}, a negative signal is dominant over a

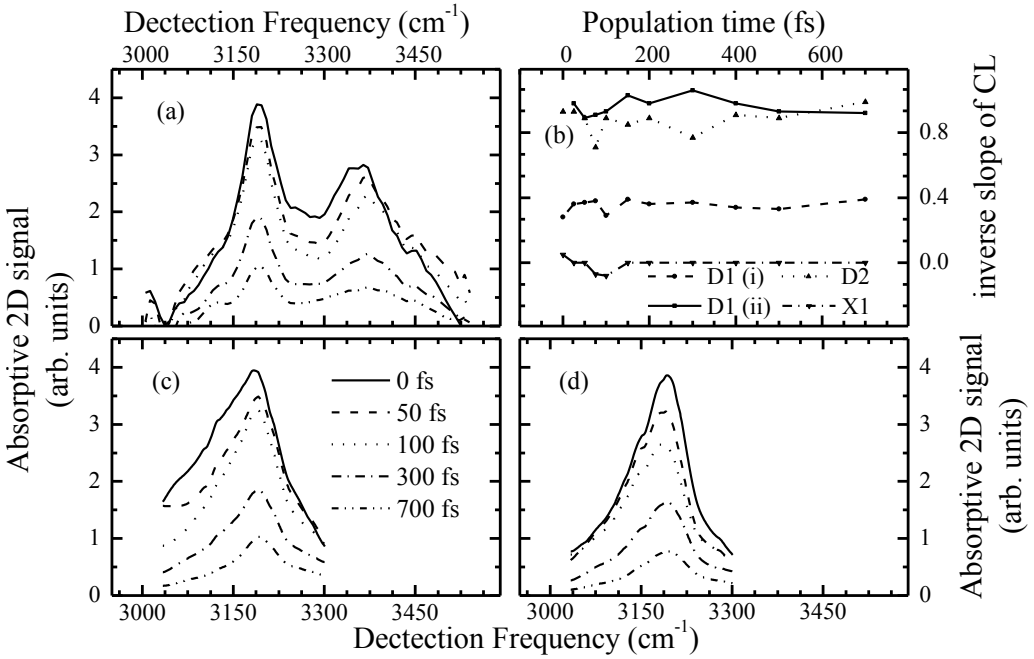

Figure 4-8: Cross sections along (a) diagonal and (c) center line through absorptive 2D spectra for sample at R.H. 0% with polarization being (||--), while (d) shows the cross sections along same positon as (c) but with polarizaiton being (||||) . The cross sections are plotted as function of detection frequency. The slopes of center lines are shown in (b), as function of the population time.

very broad range of ν_1 from 3100 to 3500 cm^{-1} with two maxima located at (ν_3,ν_1)= (3200, 3050) cm^{-1} and (ν_3,ν_1)= (3350, 3050) cm^{-1} in the case of perpendicular polarization. The intensity of these two peaks varies to some extent with population time, but the peak shape does not change significantly.

The two diagonal maxima are attributed to the fundamental 0→1 transitions of NH stretching oscillators. All different vibrations display substantial overlaps due to their extremely broad bandwidth. Nevertheless, the different peaks have distinguishable different lineshapes. The upper peak D2 appears to be an ellipse along the diagonal, with a tip extending to higher frequency. The lower peak D1 displays more complex pattern which consists of two different components. With the intense narrow peak centered at (3200, 3200) cm^{-1}, there is a shoulder sticking out along the diagonal towards the low frequency side. Moreover, the narrow peak exhibits an ellipse not along the diagonal but forms an angle. This tilted ellipse becomes more pronounced when the polarizations of interacting pulses are perpendicular. For a detailed inspection, we determined the center line of each peak, shown as the solid thick line in Figure 4-8 (a). The center lines were derived by finding and connecting the maxima of cross sections along ν_3 taken at different excitation frequency ν_1. The angle between the center line of D1 and the diagonal turns out to be 28.1 degree. There are two components of the diagonal peak D1 with distinctly different center lines; the center line of the shoulder is basically parallel to the diagonal, while the center line of the ellipse forms an angle with the diagonal. To better separate the two components, cross sections of D1 along the diagonal and along the center line were taken and shown in Figure 4-8 (a) and (c) respectively. The diagonal cross sections (Figure 4-8 (a)) exhibit the bleaching signal of the vibrations of the system; therefore they display basically the two strong peaks at the same positions as in the linear spectra. The peak at 3200 cm^{-1} consists of a spectrally narrow component superimposed on a broader one instead of a single peak. It should be noted that the cross sections along the center line is neither a single peak but have a rather long tail, the position of which suggests the existence of a cross peak. However, the strong overlap between the diagonal peaks and the cross peak prevents us from analyzing it into more details. Nevertheless this is evident that the lower peak is composed .by two different contributions, (i) a narrow band with bandwidth in the order of 50 cm^{-1} and relatively round, (ii) a broader band with bandwidth over 130 cm^{-1} and extends along the diagonal. As we have discussed in section 2.5.4, different peak shapes correspond to different combinations of homogeneous and inhomogeneous broadening mechanisms. The round peak shape is dominated by the homogeneous broadening while the

ellipse along diagonal is dominated by the inhomogeneous broadening. Thus the two components are dominated by the homogeneous broadening (D1(i)) and the inhomogeneous broadening (D1(ii)). The bandwidths of the components were derived by doing a peak fit, consisting of a narrow peak and a broad one, on the diagonal cut. The widths of components stay unchanged in the measured time scales, within the error margin. The peak at 3350 cm^{-1} presents also a shoulder around 3450 cm^{-1}. It can hardly be noticed in the 2D plots, since the lineshape of the shoulder is similarly extending along the diagonal as the peak D2. However, it is confirmed by all the cuts at different population times. Therefore, the diagonal peak D2 is composed of two different components as well, (i) the broad peak along the diagonal and centered at (ν_1,ν_3)=(3350, 3350) cm^{-1}, (ii) a weak shoulder along diagonal too and centered at (ν_1,ν_3)= (3450, 3450). They are both dominated by the inhomogeneous broadening.

A comparison of cross sections along center lines of D1(ii) between different polarization (Figure 4-8 (c) and (d)) shows that the D1(ii) is significantly more asymmetric when the polarization is ||-- than when the polarization is ||||, in the first 100 fs. The variation of the peak shape under different polarization configuration means that the wing of the cross sections come from different contribution, which is likely the cross peak between D1(i) and D1(ii). The difference points out a coupling between two oscillators which have different directions of their transition dipoles. The quick disappearance of the difference suggests that the two oscillators reach their equilibrium very quickly.

To investigate the time evolution of the different peaks, the inverse slopes of the center lines are plotted as a function of population time in Figure 4-8(c). All the slopes stay at same value, within experimental error margin, for population times up to 700fs. The stable slopes of the center lines show that spectral diffusion is limited to the bandwidth of the different peaks.

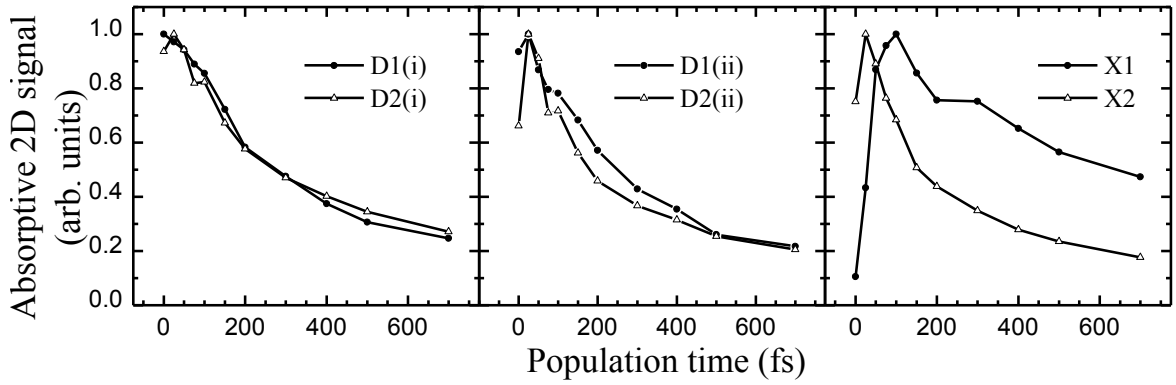

Figure 4-9: Normalized spectrally integrated intensity of the peaks as a function of T. The integrations were made over each peak on the 2D spectra recorded with (||--) polarization configuration.

Integration over each component was taken from the 2D spectra measured with the (||--) polarization configuration, and shown in Figure 4-9 as a function of population time T, for a more detailed inspection on the temporal dynamics. The two main components of the diagonal peaks D1(i) and D2(i) show a substantial decay which is reproduced by a single exponential decay with a time constant of 430 fs. This behavior is close to the kinetics observed before in the pump-probe experiments [31, 32], where a fast component of 500 fs was attributed to the fast decay of the v=1 state and a slow component around 20 ps to the longlife time of a vibrational hot ground state. The slow component is not observed in the 2D measurements up to 1 ps. The integrations are made also over the two shoulders of the diagonal peaks, represented by D1(ii) and D2(ii). To avoid the influence of the excited state absorption, the integrated area of D1(ii) is limited to the half where $\nu_1<\nu_3$, i.e., $3093<\nu_3<3125$ and $(\nu_3-20)<\nu_1<\nu_3$. The single exponential fittings show that the lifetimes of two components D1(ii) and D2(ii) are substantially similar to that of D1(i) and D2(i) within the error margin of the experiment. The kinetics of the two off-diagonal peaks X1 and X2 differs considerably. While X2 decays monotonously after 25 fs on a similar time constant as the diagonal peaks, X1 increases first until it reaches the maximum at T=100 fs and then decays for a factor of only 2 within next 600 fs, which is much slower than any other oscillators.

The initial increase of X1 can be attributed to two possible processes, (i) the decay of the spectrally broad excited states absorption (ESA) signal of D2 overlapping with the cross peak X1, which is shown as the negative signal, and (ii) the energy transfer from oscillators at 3350 to 3200 cm^{-1}. In Figure 4-10 (a), the cross sections along the detection frequency ν_1=3345 cm^{-}

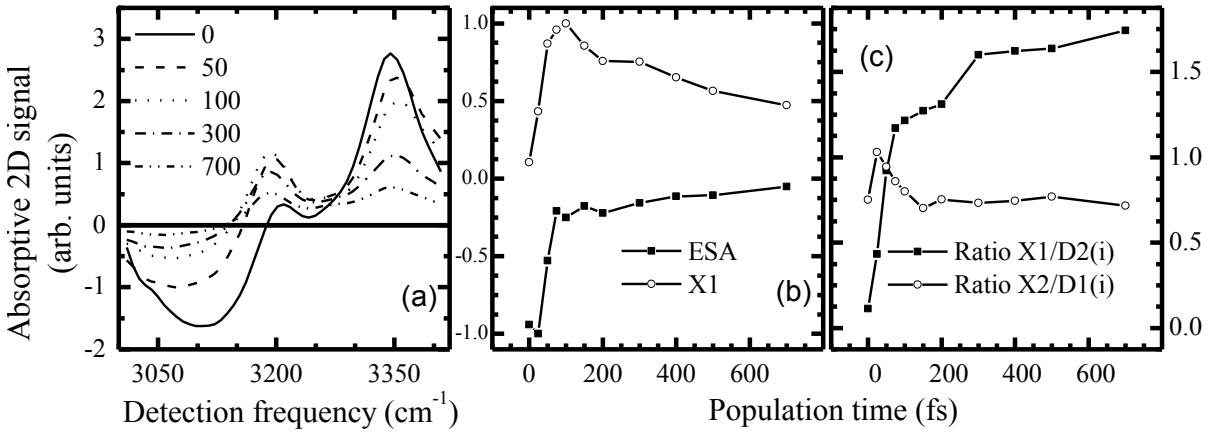

Figure 4-10: (a) Cross section of absorptive 2D IR for sample at 0% along the detection frequency ν_1=3345 cm^{-1}. (b) Normalized spectrally integrated intensity of the excited state absorption at low frequency side, compared with the integration of off-diagonal peak X1. (c) Ratio of X1/D2(i) and X2/D1(i) of normalized integration.

[1] at different population times are plotted. The narrow peak at ν_3=3200 cm^{-1} is the off-diagonal peak X1. It appears to be on top of a spectrally broad background extending down to 3000 cm^{-1}, which is assigned to the ESA of D2(i). With the strong overlap between the narrow component and the broad background, it is hard to separate the potential increase of the positive peak in early time period from the decay of the negative background. The dynamics of excited state absorption, by integrating the peak at (ν_1, ν_3)=(3350, 3100), shown in Figure 4-10 (b), exhibits a quick decay in the first 100 fs similar to the quick rise of X1 signal. After the first 100 fs, the ESA signal has decayed to a low intensity and slowed down, thus the dynamics of X1 signal is dominated by the coupling and/or energy transfer between the oscillators at 3200 and 3350 cm^{-1}. The slowed down decay of the ESA is in line with the 430 fs decay of the bleaching signal of D2(i). For a quantitative inspection, the ratio between X1 and D2(i) is calculated and shown in Figure 4-10 (c) as a function of population time T. Apart from the quick rise in the first 100 fs, the ratio keeps rising for the next 600 fs, with a time constant of the order of 0.5 ps. In contrast, the ratio between X2 and D1(i) stay relatively unchanged during the 700 fs we measured.

4.3.2 Assignment of NH stretching modes

We first discuss the assignment of the NH stretching modes. In the adenine-thymine base pair, there are three NH oscillators, two of which are located on the NH_2 group of adenine and the other one is located on the NH group of thymine. For isolated adenine molecules in the gas phase, the NH_2 vibrations have been treated as asymmetric and symmetric NH_2 stretching modes with measured frequencies at 3569 and 3451 cm^{-1} respectively [124]. In gas phase, the adenine molecules are far away from each other, i.e., there is little interaction between different molecules. Thus, both NH units of the NH_2 group are free and possess identical vibrational frequency, and the frequency difference between the two peaks $\Delta\nu_{NH}$=3569-3451=118 cm^{-1} is due to the coupling between two NH stretching oscillators. This is supported by the frequency position of the center at 3510 cm^{-1}, which is close to the frequency of the free NH oscillator, N9H of free adenine, located at 3509 cm^{-1}. Therefore, the coupling $|V|=\Delta\nu_{NH}/2$ between the two NHs equals to 59 cm^{-1}. When the base pair is formed in WC geometry, the formation of a hydrogen bond between one NH unit of the NH_2 group and the CO group of thymine will distort the symmetry of the NH_2 group. As a result, it is not clear whether the NH_2 group can still be described as symmetric and asymmetric stretches or as individual stretching modes of the two localized oscillators, one hydrogen-bonded and the other one free. The gas phase spectra of isolated A-T pairs display two stretching bands of the

adenine NH_2 group at 3326 and 3530 cm^{-1} ($\Delta\nu_{NH}$=3530-3326=204 cm^{-1}) and the stretching band of the free N9H group at 3507 cm^{-1}. It still preserves the pattern that the free NH stretching is located between the other two stretches. Moreover, the spectra downshifts of the NH bands caused by hydrogen bonding in the A-T pair are of the same order of magnitude as $\Delta\nu_{NH}$ and theoretical calculations suggest couplings between the adenine and thymine NH stretching oscillators much smaller than $\Delta\nu_{NH}/2$ [125]. In our measurement, the two peaks have a splitting of 150 cm^{-1}, being similar to the free NH_2 group in isolated adenine. Since the main difference of two situations is the formation of one hydrogen bond, the coupling between the two NH stretching modes is not changed substantially and splitting is still comparable to that of two peaks of the free NH_2 group. Therefore the frequency difference between two stretching modes is mainly due to the coupling between two NH stretching modes and the asymmetric and symmetric treatment is still valid. The absence of a long-living free NH oscillator in time-resolved experimental results also supports this picture. Isolated thymine molecules in the gas phase display stretching frequencies at 3435 and 3482 cm^{-1} for N3H and N1H group [124, 126]. Upon formation of AT pairs, the N3H group forms a hydrogen bond with N1 of adenine. The stretching frequency of the hydrogen-bonded N3H shifts down to 3295 cm^{-1}, a value close to the frequency of the symmetric NH_2 stretching vibration of adenine in the base pair (3326 cm^{-1}).

According to the earlier pump-probe studies [31], the upper peak at 3350 cm^{-1} is assigned to the asymmetric stretching mode of the NH_2 group of adenine and the lower peak to the superposition of the hydrogen-bonded NH stretch of thymine and symmetric stretching mode of the NH_2 group of adenine. This picture is in agreement with the gas phase measurement, that the frequency of the asymmetric NH_2 stretching mode is higher than that of the symmetric NH_2 stretching modes, while the hydrogen-bonded NH of thymine is found at a similar vibrational frequency. In the 0% R.H. sample, there are still two water molecules per base pair, the OH stretching of the water molecules is assigned to the small shoulder at 3500 cm^{-1}. This type of local interaction is similar to that of water molecules interacting with the ionic heads of small reverse micelles [127-129], where the OH stretching band is narrowed and peaks at frequencies around 3500 cm^{-1} and above, depending on the micelle sizes [129].

In agreement with those assignments, in the 2D spectra, the diagonal peak D2 (3350, 3350) cm^{-1} corresponds to the fundamental transition of the asymmetric NH_2 stretch of adenine (cf. Figure 4-7). The shoulder observed at the higher frequency side in the diagonal cuts (cf. Figure 4-8 (a)) is assigned to the OH stretching modes of the water molecule attached to the

phosphate group. They both exhibit rather stable peak shape during the experiment time (cf. Figure 4-7 and Figure 4-8 (c)). Around D1 (3200, 3200) cm^{-1}, the 2D spectra and cross sections display two different features, (i) a substantial narrow band tilted to the ν_1 axis and (ii) a broad band elongated along the diagonal (cf. Figure 4-7 and Figure 4-8 (a), (b)). According to the pump-probe experiment, the combination of the two components is assigned to the NH stretch of thymine and the symmetric NH_2 stretch of adenine. Considering that the upper peak at 3350 cm^{-1}, which is clearly inhomogeneously broadened with the center line parallel to the diagonal, was assigned to the asymmetric stretching modes of NH_2 from adenine, we, thus, assign the similarly broad component (ii) to the symmetric NH_2 stretch of adenine. The component (i) is hence assigned to the stretching mode of the hydrogen bonded NH group of thymine. Both components exhibit stable peak shapes too (cf. Figure 4-8 (c)).

The T-independent peak shapes show that there is no measureable spectral diffusion beyond the bandwidth in the time range of the order of hundreds of femtoseconds and suggest a stable structure of the DNA system in low hydration level in the picosecond time scale. Generally, spectral diffusion originates from the structure fluctuation of the excited vibrational group, including the fluctuating geometry of the hydrogen bond and fluctuating forces exerted by the bath. As a big biomolecule containing hundreds of atoms embedded in the solid film, it has a rather rigid structure that does not allow any quick structural change in such a short time. Nevertheless, the helix and its polar groups, such as the phosphate groups, undergo fluctuating thermal motions which can result in a fluctuating long-range Coulomb interaction with the vibrational transition dipoles. Therefore, the minor spectral diffusion here suggests that the frequencies of the fluctuation motions are too low to take effect in such a short time, supported by the sub-200 cm^{-1} frequency of DNA backbone motions [130], and the interaction strength is limited because of the substantial distance between the polar groups on the outside and the AT pairs in the inner part of the DNA structure.

At very low hydration level of R.H. 0%, there are only few water molecules attached to the phosphate group of backbone. The hydrogen bonds between the water molecules and the phosphate group have a binding energy of about 8kJ/mol, higher than other molecules [87], and tightly attach the water molecules to the backbone of DNA molecules. The fluctuation of the water molecules is therefore strongly restricted and the spectral diffusion originating from rotation of water molecules is hindered. The constant anisotropy of the OH stretch excitations observed in the previous pump probe experiment [31] confirmed the rather rigid attachment of

the water molecules to the backbone of the DNA and the minor role of hydrogen bonds between base pair groups and water molecules.

Thus, the 'quasi-static' inhomogeneity of the system, mainly the NH_2 group of adenine and the OH group of the water, is attributed mainly to structural disorder. For the NH_2 group, the unbound NH unit sticking out of the base pair is a probe of the molecular surroundings. Structure inhomogeneity along the double helix or of the interaction between double helices and CTMA counterions is reflected on the vibrational Eigenfrequency of the free NH and, thus, stretching frequencies of the NH_2 group. Therefore, one could expect a correlated broadening of the symmetric and asymmetric NH_2 stretching modes of adenine. In contrast, the NH stretch of thymine is embedded in the well-defined base pair with the hydrogen bond to adenine being the strongest local interaction. Thus, it is less sensitive to structural inhomogeneity and appears rather homogeneous, which is in line with the 2D lineshape tilted away from the diagonal. The water molecules attached to the outside of the well-defined double helix sit very close to the phosphate groups and to the CTMA counterions as well. The disorder of the attachment of the CTMA to the phosphate group of the DNA, such as in distance and angle, give the water molecules various possibilities to attach to the phosphate group. Hence, the inhomogeneous broadening of the OH stretch of the water molecules is expected.

4.3.3 Vibrational Relaxation and Coupling of NH stretching Modes

Figure 4-9 displays the temporal evolution of the four peaks. All diagonal peaks D1(i), D1(ii), D2(i) and D2(i) decay similarly with a time constant of approximately 430 fs, corresponding to the lifetime of v=1 state of the oscillators. Such decay are in agreement with the results of the pump-probe experiments. Upon formation of hydrogen bonds, the NH stretches are red-shifted and located closer to over- and/or combination tones of fingerprint modes. The reduction of the energy mismatch enhances the decay rates of the NH stretches via fingerprint modes. A strong anharmonic coupling between the NH stretching modes and overtones and combination tones which have a strong NH bending contribution has been observed in 7-azaindole dimers [131] and in DNA oligomer [111], and it serves as the most efficient relaxation channel for the initially excited NH stretches. IR pump/anti-Stokes Raman probe experiments show that vibrational energy transfers from the excited NH stretching oscillators to fingerprint vibrations of A-T base pairs in same DNA oligomers studied here [132].

The diagonal peaks shown in the cross sections along the center line of the narrow D1(i) suggest that there is an anharmonic coupling or/and energy transfer between the of symmetric NH_2 stretching mode of adenine and the hydrogen-bonded NH stretching mode of thymine. This is in line with the anisotropy decay observed in the pump-probe experiment [32]. The pump-probe signal showed an anisotropy decay at 3200 cm^{-1}, with a time constant of 150 fs. The quick decay suggested that the energy transfer between the NH stretch of thymine and the symmetric NH_2 stretch of adenine has a coupling strength of 15 cm^{-1}, making the distribution of excited dipoles between the two oscillators reach their equilibrium very quickly. This agrees with the quick disappearance of the difference of the symmetry when the polarization configurations are different. However, the strong overlap between the diagonal and off-diagonal peaks hindered further analysis in the present 2D spectra.

The presence of off-diagonal peaks indicates the existence of an anharmonic coupling and/or energy transfer between asymmetric stretches of the NH_2 group at 3350 cm^{-1} and one (or two) mode(s) at 3200 cm^{-1} (c.f. Figure 4-7). In general, a cross peak displays a dispersive pattern as we discussed in 2.5.4. However, when the off-diagonal anharmonicity is smaller than the spectral bandwidth of the original peak, the two components overlap with each other and, thus, result in a cancellation of intensity. For the off-diagonal peak X2, the spectral broadness of the peak D2(i) causes a strong compensation of positive and negative contribution of the off-diagonal peak X2. Together with the extensive shoulders of the spectrally broad diagonal peaks, the compensation results in a broad weak feature at the position of the off-diagonal area. From this we can hardly conclude what the off-diagonal coupling between the modes at 3200 and 3350 cm^{-1} is, but only estimate that it is substantially smaller than the spectral half width of D2(ii) of 70 cm^{-1} along ν_3. In contrast, for off-diagonal peak X1, we observe a less broad off-diagonal which suggests that a narrower peak contributes to the detection of this peak. Therefore, the transition contributing to the off-diagonal peak X1 is assigned mainly to the narrow component D1(i) of the lower diagonal peak, i.e. the NH stretching mode of thymine.

The positive off-diagonal peaks X1 and X2 behave temporally differently as well. While the X2 decays monotonously in 700 fs by a factor of 5, similarly to the decay of diagonal peaks, X1 first increases until it reaches its maximum at T=100 fs and then decays only by a factor of 2 at T=700 fs (c.f. Figure 4-10(b)). Since the peak X1 is superimposed on the initially (T=0 fs) predominant spectrally broad negative contribution due to the $v=1\rightarrow2$ transtion (c.f. Figure 4-10(a)), the quick rise of X1 during the first 100 fs is strongly influenced by the fast decay of

the negative contribution. Nevertheless when the excited state absorption is much weaker after T=100 fs, the positive X1 dominates over the residual negative signal. The rise of the ratio of the off-diagonal peak X1 over diagonal peak D2(i) (c.f. Figure 4-10(c)) suggests an energy transfer from the oscillator at ν_{01}=3350 cm^{-1} to the oscillator at ν_{01}=3200 cm^{-1}, in which the upper oscillator is deactivated and the (unshifted) v=0→1 transition of the lower oscillator excited. The energy difference between the two excitations is accepted by the vibrational manifold of the DNA. This downhill energy transfer enhances the positive X1 component relative to D2(i) whereas the negative spectrally shifted X1 decays in parallel to the deactivation of upper oscillator. In the 2D experiment, after the excitation of the upper oscillator by the first two pulses, the energy transfer provides an additional channel of the v=1 population decay of the upper oscillator and results in the v=1 population of the lower oscillator, before the third pulse comes and detects the sample. As a result, decay of the X1 is slowed down compared to the D2 decay. The inverse energy transfer, i.e. uphill process from the NH stretching mode of thymine at ν_{01}=3200 cm^{-1} to the asymmetric NH_2 stretching mode of adenine at ν_{01}=3350 cm^{-1} is less efficient because of the energy mismatch. Otherwise, it would enhance the intensity of the positive peak X2 relative to D1(i). Such behavior is absent (c.f. Figure 4-10(c)), i.e., the rate of the uphill energy transfer is substantially smaller than the population decay rate of the asymmetric NH_2 stretching oscillator.

There are two time constants in the time evolution of the intensity ratio X1/D2(i), 1) the quick rise during the first 100 fs, which is strongly affected by the spectral broad negative signal and 2) the slower rise with 0.5 ps time constant, which is attributed to the energy transfer. Taking the 0.5 ps as the measure for the incoherent energy transfer time, a standard Fermi golden rule approach gives an absolute value of the coupling strength between two oscillators of the order of 5 cm^{-1}. Couplings of same order between vibrational transitional dipoles have been observed in fingerprint modes by Krummel et.al [110] and for NH stretch oscillators by Szyc et.al [32]. It again confirms the approximation we made before that the coupling is so small that we cannot derive it from the lineshape of the off-diagonal peaks.

Very similar experimental results were measured with DNA oligomers containing 23 non-alternating AT pairs. This fact suggests that in the system studied here, energy transfer along the helix, e.g., between the stacked base pairs is not playing an important role. Instead, the energy transfer between the asymmetric stretching mode of the NH_2 group of adenine and the stretching mode of the hydrogen bonded NH from thymine is favored as a dipole-dipole coupling due to their relative close distance of 0.35 nm and the small angle ~30º between the

transition dipoles, both determined by the base pair geometry. This is supported by the positions of both cross peaks X1 and X2, as well as the vertical center line of peak X1 and its bandwidth being comparable to that of the NH stretch oscillator as part of diagonal peak D1.

In general, one should consider also a vibrational anharmonic coupling between the symmetric and asymmetric stretching modes of the NH_2 group of adenine. Under the broadband excitation conditions applied here as well as in the pump-probe experiment, such anharmonic coupling should result in a quantum beat [133], i.e., the modulation of the intensity of the off-diagonal peak at a frequency determined by the spectral splitting of the two vibrations of 150 cm^{-1}/220fs. However, such behavior is absent in our experiment, and also in the spectrally resolved pump-probe experiment done for different relative humidity [31, 32, 113]. Moreover, the positive component of such a coupling would result in a very broad off-diagonal peak comparable to the width of D2 and the broad contribution of D1 while this signature is not obvious as well. Thus, we conclude that the coupling between the symmetric and asymmetric stretching modes of NH_2, if existing, is much smaller than the bandwidth of both peaks and impossible to retrieve from our experimental results.

In conclusion of this section, we have studied DNA oligomers containing 23 adenine-thymine base pairs with only few water molecules attached to the phosphate group of the backbone. The 2D spectra are predominantly attributed to excitations of the NH stretching modes of the base pairs. The peak at 3200 cm^{-1} is assigned to the superposition of the symmetric NH_2 stretch of adenine and hydrogen-bonded NH stretch mode of thymine, while the peak at 3350 cm^{-1} is assigned to the symmetric NH_2 stretch vibration of adenine. The different lineshapes of the NH stretches enable us to discern the spectrally narrow homogeneously broadened NH stretch band of thymine from the broad inhomogeneously broadened transition of the symmetric NH_2 stretch band of adenine. The inhomogeneous broadening of the symmetric and asymmetric NH_2 stretches is probably due to the unbound NH unit sticking out of the base pair which is sensitive to the varying environment, while the hydrogen-bonded NH group of thymine exhibits mainly homogeneous broadening. An energy transfer is observed from the asymmetric NH_2 stretch of adenine to the NH stretch of thymine. In contrast, energy transfer between base pairs is negligible. In general, the DNA structure is rigid and does not fluctuate in the short time scale we studied, thus no pronounced spectral diffusion was observed. The few water molecules attached to phosphate group of the DNA have rigid structure and undergo no obvious spectral diffusion.

4.4 Ultrafast Dynamics of DNA-Water Interactions

4.4.1 Results

In order to study the interactions of the water shell with DNA, samples at higher humidity were studied. The absorptive 2D spectra of samples at 33 and 92% R.H. are shown in Figure 4-11. According to Falk's study [87], there are 6 and more than 20 water molecules per base pair in the sample at 33 and 92% R.H. respectively. Both data sets are measured with the perpendicular polarization configuration.

The 2D spectra obtained at 33 and 92% R.H. display initially patterns similar to that of the sample at 0% R.H., consisting of two diagonal peaks D1 and D2 that appear at (ν_1, ν_3) = (3200, 3200) cm^{-1} and (3350, 3350) cm^{-1}, and two off-diagonal peaks X1 and X2 present at (ν_1, ν_3) = (3200, 3350) and (3350, 3200) cm^{-1}. However, this pattern is on top of a stronger background which covers the region where ν_1 and ν_3 are higher than 3100 cm^{-1}. The shoulders extending to the lower and higher frequency along the diagonal is still present underneath diagonal peaks D1 and D2. With the spectral positions barely different, the amplitude and the peak shapes are undergoing moderate changes. The off-diagonal peak X2 becomes more pronounced than X1 at T=0, while they are comparable in 2D spectra at 0% R.H.. The diagonal peak D2 appears rounder and thus less inhomogeneous than it was at 0% R.H.. The shoulder of D2 is getting more intense when the relative humidity is increasing.

In the spectra at 33% R.H., a contribution on the diagonal at (3270, 3270) cm^{-1} rises relatively to the two diagonal peaks as a function of population time T. This contribution is more pronounced in 2D spectra at 92% R.H.. While the peak D1(3200, 3200) cm^{-1} is undergoing little reshaping as a function of population time T, the upper peak D2(3350, 3350) cm^{-1} changes substantially. The overall peak shape of the 2D spectra is becoming rounder too, as the population time T evolving, due to the increasing off-diagonal peaks and the wings which fill the gaps between the peaks. The speed of the reshaping increases when the humidity increases.

On the right part of the spectra, where ν_3>3450 cm^{-1}, both spectra exhibit delayed build-up of a negative signal. In spectra at 92% R.H., it starts to appear for T≥100 fs. At T=700 fs, it turns to be a peak extending along ν_1, and peaking at (ν_3, ν_1) = (3500, 3480) cm^{-1}. Along the ν_3 dimension, the negative signal is strongly overlapping with the positive signal, making them

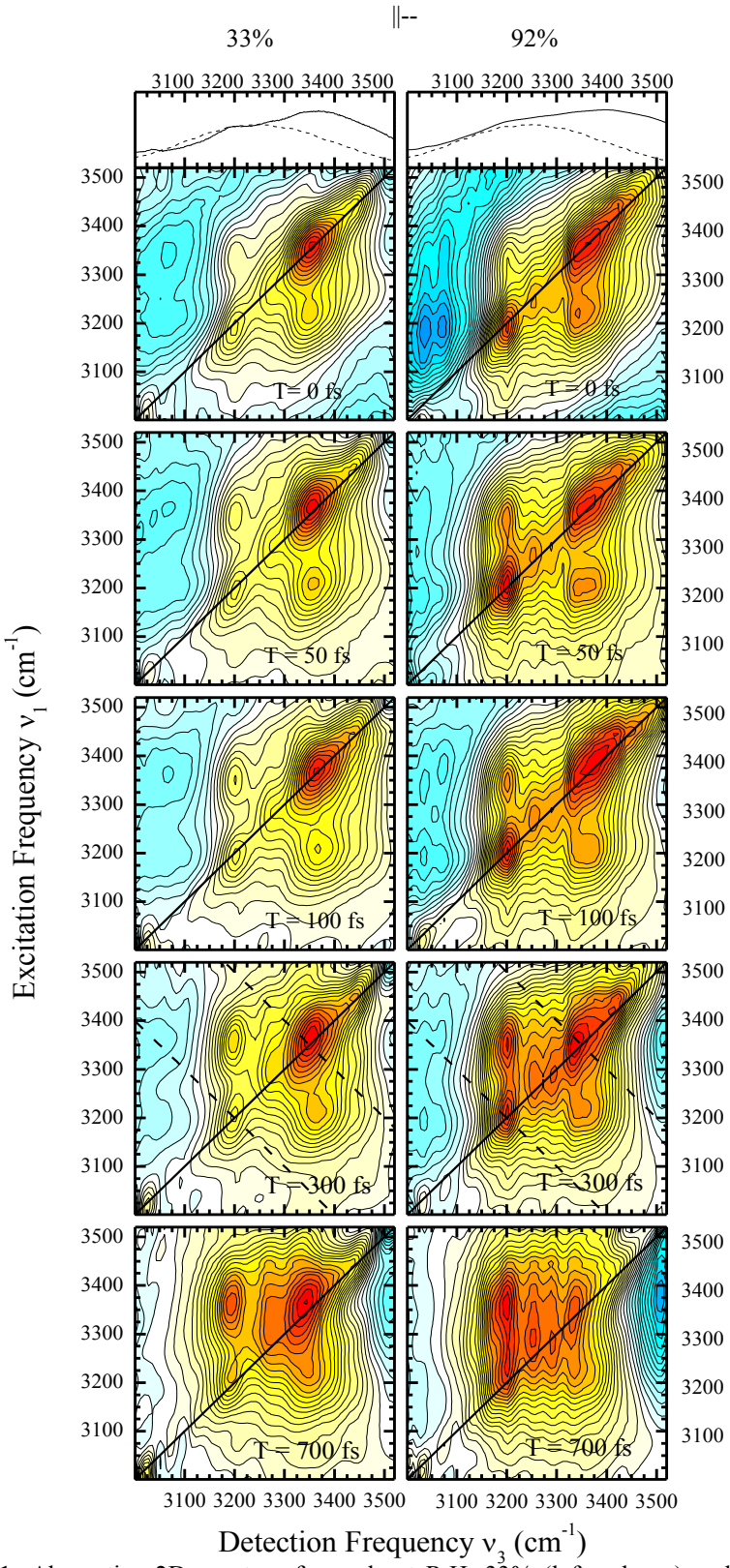

Figure 4-11: Absorptive 2D spectra of sample at R.H. 33% (left column) and 92% (right column). The spectra are listed with increased population time T from up to down. The polarizations of the pulses k_3 and k_{LO} are perpendicular to that of k_1 and k_2. Each spectrum is normalized to its positive maximum and contour lines correspond to 5% changes in amplitude. On top of both columns, the linear absorption (solid line) and spectrum of excitation pulses are present. The dash lines in the T=300 fs panels indicat where the anti-diagonal cross sections in Figure 4-12 were made.

both distorted. Along the ν_1 dimension, the negative signal is very broad, covering a range from 3100 to 3500 cm^{-1}.

For a more detailed inspection, normalized cross sections along diagonal and anti-diagonal through (3200, 3200) and (3350, 3350) cm^{-1} were made and are shown in Figure 4-12.

For the diagonal cross sections, the peak at 3200 cm^{-1} was the unit for the normalization of the results at the different hydration levels. The cross sections at 0% R.H. display T-independent lineshapes for the peak at 3200 cm^{-1}, and the overall lineshape changes only slightly due to different decay rates of the peak at 3350 cm^{-1} without any significant reshaping. The cross sections at higher hydration level exhibit a similarly stable peak at 3200 cm^{-1}. In contrast, the shoulder at 3270 cm^{-1} starts to increase as a function of population time T. For the sample at 33 and 92% R.H., this contribution increases for roughly 10% and more than 20% respectively, which implies the increasing role of the contribution around 3270 cm^{-1} when the

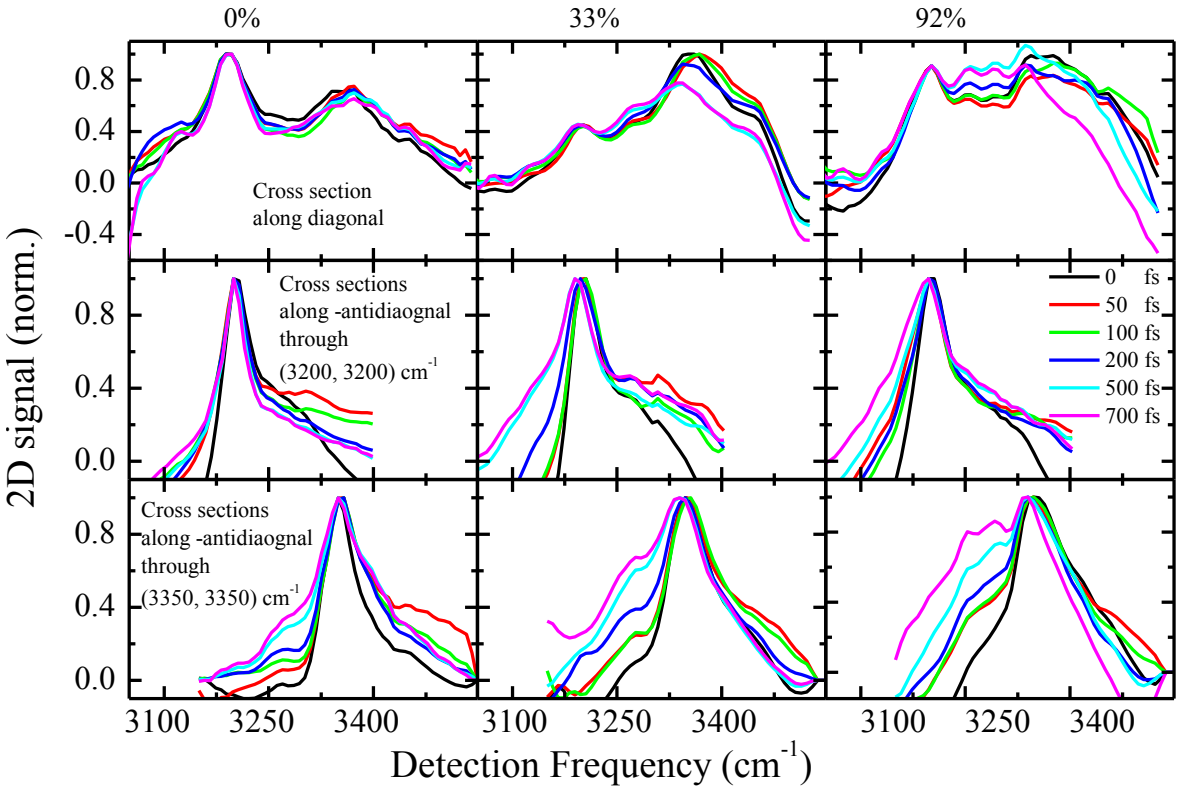

Figure 4-12: Normalized cross sections along diagonal and anti-diagonal for sample at different relative humidities 0% (left column), 33% (center column) and 92% (right column). The first row presents the cross sections along diagonal, normalized to the peak 3200 cm^{-1}. The second row presents the cross sections along anti-diagonal through (3200, 3200) cm^{-1} and the third row shows anti-diagonal cross sections through (3350, 3350) cm^{-1}, which are normalized to their maximum. All anti-diagonal cross sections were normalized to their maximum.

water content is also increased. The shoulder on the lower frequency side of peak 3200 cm^{-1} appears to be less pronounced when the hydration level increases, while the shoulder on the higher frequency side of peak 3350 cm^{-1} is enhanced to comparable intensity with the main peak and results in a broader peak.

The cross sections along anti-diagonal through (3200, 3200) cm^{-1} were normalized to their maxima. The cross sections for the sample at 0% R.H. show unchanged lineshape on high frequency side; the rising on low frequency side between 0 fs and 50 fs is mostly due to the fast decay of the negative excited state absorptions. This invariability on high frequency side persists with the increasing water content. The continue rise of low frequency side during later time is more pronounced in sample at high humidity, which could be the combining effect of decaying excited state absorption and rising cross peaks. The dynamics of the cross sections at 33 and 92% R.H. are comparable within experimental errors. The half width at half maximum at high frequency side is 25±5 cm^{-1} for sample at R.H. 0% and 33%, and 35±5 for sample at R.H. 92%. The width was calculated on its projection onto the detection frequency. The moderate change of the lineshapes indicates a weak interaction between the peak at 3200 cm^{-1} and the increased water molecules.

The cross sections along anti-diagonal through (3350, 3350) cm^{-1} for sample at R.H. 0% exhibit a narrow peak centered at 3350 cm^{-1}. The main body of the peak stays unchanged with time evolving while the shoulder on low frequency side rises. The rise of the shoulder can be

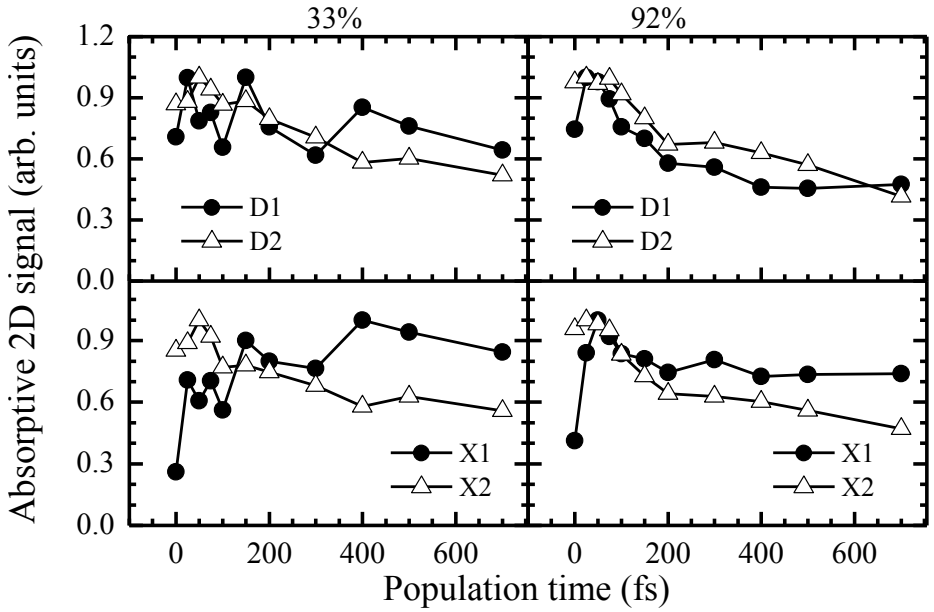

Figure 4-13: Normalized spectrally integrated intensity of the peaks for sample at R.H. 33% (left column) and 92% (right column). The general behaviors of four peaks are similar independent of different relative humidity.

attributed to the combination of the decay of excited state absorption of D2 and rise of X1 as well as a broad contribution underneath when the relative humidity is high. With increasing water content, the rise of the broad shoulder becomes more pronounced, suggesting the broad component comes from the OH stretching mode of water. Being fitted with two Gaussian peaks, the strong narrow peaks give a bandwidth (FWHM) of 35±5 cm^{-1} for sample at 0 and 33% R.H. and 50±10 cm^{-1} for sample at 92% R.H. projected on the detection frequency coordinate. The broad contribution is affected by the excited state absorption at low frequency side or hot ground state absorption, which will be discussed later, at high frequency side; thus it is impossible to obtain a reliable result about its real bandwidth.

The temporal behavior of the peaks is presented in Figure 4-13 after integrated over the peaks of the 2D spectra on samples at 33 and 92% R.H.. The diagonal peaks D1 and D2 decay in sub-picosecond time, which is close to the pump-probe results of the sample at 92% R.H.. After 700 fs, the residue value is considerably higher than that of the sample at 0% R.H.; it is due to that the OH stretches at hot ground states hinder the refilling of the ground state and maintain the ground bleaching signal. The off-diagonal peak X1 displays a delayed rise and a

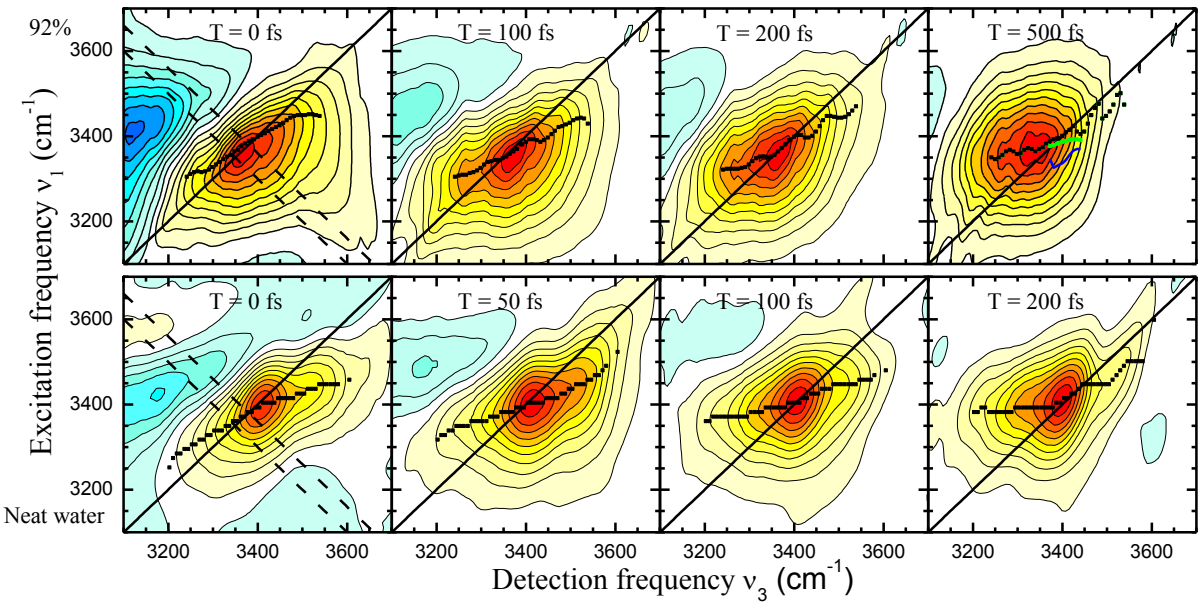

Figure 4-14: (a) Absorptive 2D spectra of sample at 92% R.H. and excited at 3400 cm^{-1} as a function of population time T. (b) Absorptive 2D spectra of neat water at 304K and excited at 3400 cm^{-1} as a function of population time T from Ref (47). The dash lines at T=0 panels indicate the direction along which the anti-diagonal cross sections in Figure 4-15 were generated. The scatters (closed squares) in each plot indicate the maximum of the cuts along excitation frequency, from which the center line is obtained. The green and blue squares in T=500 fs for DNA-water system are the maximum of the positive and negative component due to the overlap of the 0→1 transition and 0'→1' transition signals respectively.

slower decay afterwards similar to its behavior at 0% R.H., while X2 decays in step with the diagonal peaks. The rise and slowed down decay of the cross peak X1 can be attributed to the energy transfer, similar to the mechanism in the sample at low hydration level.

To facilitate a direct comparison of water dynamics around DNA with neat water, the absorptive 2D spectra of sample at 92% R.H. excited at 3400 cm^{-1} is shown in Figure 4-14 (a) as function of the population time T together with the absorptive 2D spectra of neat water at temperature 304 K excited at 3400 cm^{-1} being shown in Figure 4-14 (b) as a reference [47]. Unlike the spectral results excited at 3250 cm^{-1}, the diagonal peak at 3200 cm^{-1} is negligible and the other one at 3350 cm^{-1} is shifted to higher frequency at around 3380 cm^{-1}, which corresponds to the maximum of linear spectrum at 92% R.H.. Here the 2D spectra were not corrected by the electric field of three interacting pulses, for better comparison with the neat water experimental results which were not corrected either. In both sets of spectra we observe a significant reshaping from initially elliptic spectral envelope along the diagonal to an essentially round envelope at later population time. This reshaping points to a spectral diffusion due to the randomization of OH stretching frequencies. However, the process in DNA-water system extends over 500 fs, much longer than the 100-200 fs in neat water.

The cross sections along the anti-diagonal through (3380, 3380) and (3350, 3350) cm^{-1} in the absorptive 2D spectra of neat water at a temperature of 304 K and of the DNA oligomers at R.H. 92% are shown in Figure 4-15 (a,b). They exhibit a clear broadening and shift towards

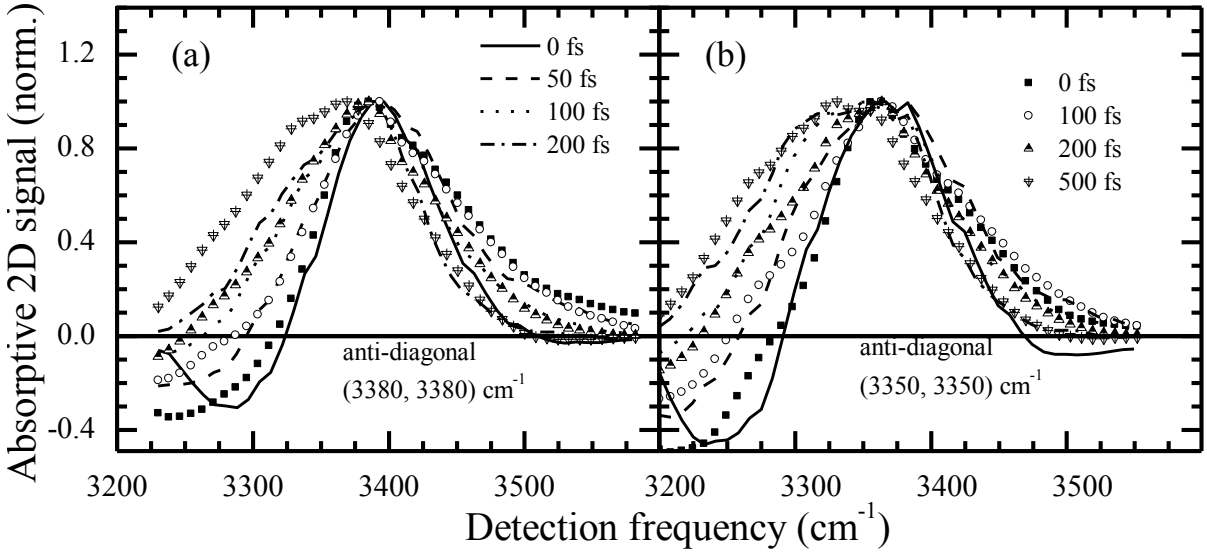

Figure 4-15: (a) Normalized anti-diagonal cross sections through (3380, 3380) cm^{-1} of absorptive 2D spectra of neat water at temperature 304 K (lines, derived from Ref. 47) and of AT oligomer at R.H. 92% (symbols). (b) Normalized anti-diagonal cross sections through (3350, 3350) cm^{-1} of absorptive 2D spectra of neat water at temperature 304 K (lines) and of AT oligomer at R.H. 92% (symbols).

the low frequency direction, as a hallmark of spectral diffusion. In neat water, this broadening and redshift occurs strongly within the first 100 fs and slows down in the next 100 fs. The lineshape approaches its final value after 200 fs when the shape of the corresponding 2D spectrum is essentially round. In contrast, the OH stretching modes in water shell of DNA display a much slower spectral diffusion, which is still unfinished after 500 fs.

In order to have a quantitative analysis, the center lines of the peak were retrieved and shown in Figure 4-14. The center lines were obtained by find the maxima of the cross sections along excitation frequency coordinates. The cuts along ordinate were meant to avoid the interference of excitation frequency and hot ground state absorption located in the left and right of the 2D plots. In principle, the center lines obtained in two different ways are equivalent. The center lines appear to form first a rather small angle with the diagonal, which becomes bigger as a function of the population time T.

The slope of the linear fitting on the center lines were shown in Figure 4-15(c) together with frequency-frequency correlation functions of bulk water from the molecular simulations in Ref. [134]. In contrast to the unchanged slopes of center lines of all peaks from the sample at 0% R.H., the slopes of the center line of the OH stretching modes decay considerably in 500 fs. The results of molecular simulation show that the frequency-frequency correlation functions decay significantly in first 100 fs from 1 to 0.5, due to small-amplitude nuclear

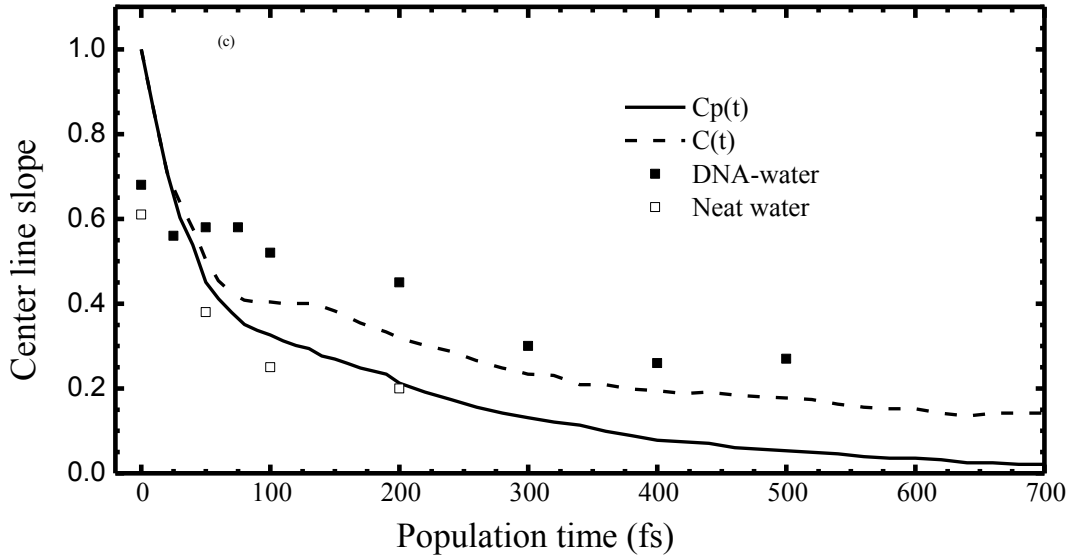

Figure 4-16: Center line slopes extracted by a linear fit of the center lines of DNA-water system (closed square) and neat water (open square, derived from ref. 47) compared with the frequency-frequency correlation function of bulk water from the molecular dynamics simulation of Ref. (134) considering resonant energy transfer (solid line) or not (dash line).

motions. Afterwards it behaves differently depending on whether the resonant energy transfer between OH stretching oscillators are considered ($C_p(t)$, solid line) or not (C(t), dash line). The resonant energy transfer occurs mainly between OH stretching modes from different water molecules, thus, playing a role only when many water molecules are located very close to each other in a network, as would be appropriate for bulk water, because the efficiency decreases greatly with increasing distance, as would be appropriate for HOD in D_2O. When the resonant energy transfer is considered, the FFCF decays quickly to zero in a few hundred femtoseconds, in contrast to the residue of 0.15 after 700 fs when it is not considered. Compared to the molecular simulation, the fast decay during first 100 fs is strongly reduced in the experimental data as it decays from 0.7 only to 0.5. The subsequent time evolution between T=100 and 500 fs is closer to C(t), showing a decay of 0.2 which is much less than $C_p(t)$ but close to C(t). At T=500 fs, the slope of the experimental data has a residue value at 0.3, much higher than the value of $C_p(t)$. Thus, the loss of OH stretching frequency correlation in the water shell of DNA is distinctly slowed down compared to bulk water.

When the population time increases to T>200 fs, the center lines of both water and the DNA-water system start to be bent, i.e., at higher detection frequency part where n_3>3350 cm^{-1} the center lines are diverted to diagonal. The distortion of the center lines is due to the appearance of the spectrally broad negative peak on the right side. The extent of distortion increases with T. The results of fitting the cross section along ordinate with two peaks, one positive corresponding to the original fundamental transition and the other one negative corresponding to the blue shifted transition, show that the maxima of positive peaks extend in agreement with the center line of low frequency part (shown in the 2D spectrum at population time

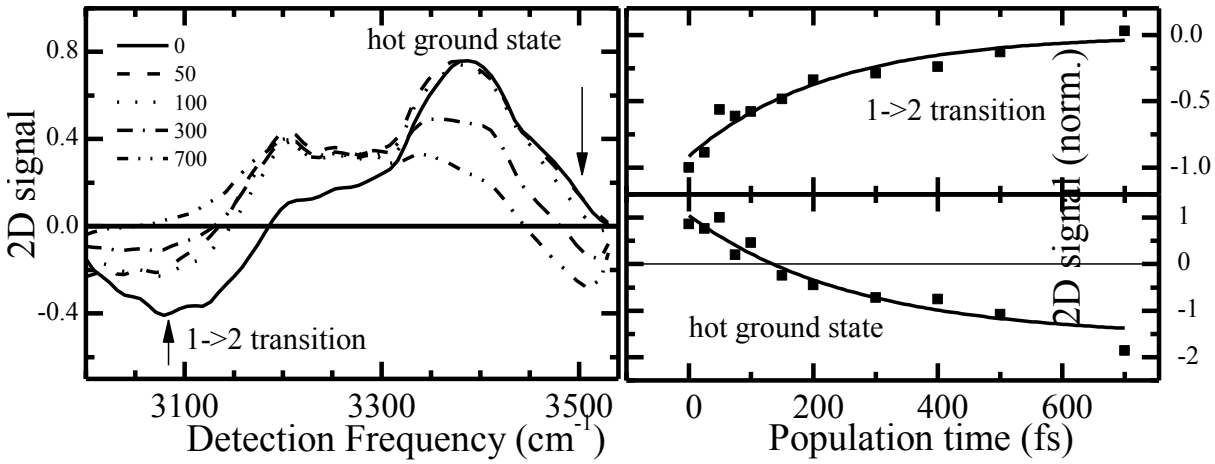

Figure 4-17: (a) Cross sections along ν_3 axis, where ν_1=3400 cm^{-1}. (b) Spectral integration of excited state absorption at low frequency side, compared with hot ground state absorption as function of T. The decay of 1→2 transition was fitted with single exponential decay (solid line).

T=500 fs of DNA-water system in Figure 4-14). A similar behavior is also observed in the neat water spectra when population time T=200 fs.

The negative signal in the right side of the 2D plots, where ν_3>3450 cm^{-1}, is commonly referred to the vibrational hot ground state of the water. The cross sections along ν_3, where ν_1=3400 cm^{-1}, show the decay of the high frequency side at 3500 cm^{-1} and becomes negative at later time, as shown in Figure 4-17 (a).

To analyze the formation of hot ground state in our experiment, the temporal behavior of spectral integration over this area is made and plotted in Figure 4-17 (b), compared with the temporal behavior of excited state absorption. A single exponential fitting of excited state absorption gives a decay time in order of 200 fs, which is combined by decays of both OH and NH stretching modes. A fitting of hot ground state absorption gives a similar time constant. Although the error bars of these fits are big due to too few time points and short evolve time, the building up of hot ground states matches the decay of v=1 states qualitatively.

4.4.2 Interactions between NH Groups and Water Molecules

The 2D spectra display the same pattern of positive diagonal and cross peaks at all hydration levels, i.e., the spectral positions of the peaks remain generally unchanged upon increasing hydration (c.f. Figure 4-7 and Figure 4-11). We, thus, assign the peaks at (3200, 3200) cm^{-1} and (3350, 3350) cm^{-1} to the stretching modes of NH and NH_2 groups in base pairs, according to the assignment made for the 2D spectra at R.H. 0%. When relative humidity increases to 33 and 92%, the OH stretching modes start to play a more important role in the measurements. Compared to the 2D spectra at 0% R.H., the NH stretches are complemented by the spectrally broad contribution, which originated from the OH stretching excitations of the water shell. Because of the increasing contribution from excited OH stretches, the consequently increasing negative ESA of OH stretching around 3400 cm^{-1} weakens the positive off-diagonal peak X1 more and makes it weaker compared to X2 initially.

While the population time T evolves, the cross sections of the 2D spectra at 33 and 92% exhibit a pronounced reshaping compared to those at 0%. In the diagonal cross sections, the reshaping involves the rise of relative intensity in-between the diagonal peaks at 3200 and 3350 cm^{-1}. In the anti-diagonal cross sections, it is mainly contributed by the time-dependent enhancement of the strong shoulder at lower frequency side. It should be noted that the increase of the shoulder of the anti-diagonal cross sections through lower diagonal peak at

3200 cm^{-1} is to much extent affected by the excited state absorption and the relative increase of the broad contribution excited around ν_1=3300 cm^{-1}. The anti-diagonal cross sections of the upper diagonal peak at 3350 cm^{-1} demonstrate that the OH stretch component relative to the NH stretch peak pattern is substantially higher at R.H. 92%. Therefore, we conclude that the 2D spectra are essentially linear superposition of the NH and OH stretching contributions, when we increase the water content in the sample. Meanwhile, the lineshapes of the NH stretching peaks are rather insensitive to an increasing level of hydration, i.e., there is only a moderate spectral broadening around unchanged spectral positions even at fully hydrated data.

At 33 and 92% R.H., the integrated intensities around fundamental NH stretching transitions decay by a factor of less than 2 within the first picosecond (c.f. Figure 4-13). The partial decay is in agreement with pump-probe experiments with perpendicular polarization configuration [32], and attributed to the formation of a hot ground state of water shell hindering the refilling of the ground state which will be discussed later in section 4.4.3. The off-diagonal peaks at (ν_1,ν_3) = (3350, 3200) cm^{-1} and (3200, 3350) cm^{-1} confirms that the coupling and energy transfer exist also in samples at high hydration level. However, the complexity and strong overlapping with OH stretches makes it very difficult to analyze the dynamics of NH stretches quantitatively.

In the 2D spectra, it is very difficult to quantitatively analyze the lineshape of the NH stretching peaks because of their strong overlapping with other NH stretching peaks and also with the OH stretching peaks. In particular, the nodal and/or center lines [48, 49, 51] in such congested 2D spectra have highly complex shape which does not allow a reliable separation of the different components and their spectral dynamics. Nevertheless, the shape and the spectral widths of the diagonal peaks give insight into the broadening mechanisms and the overall time scale of vibrational dephasing of the NH stretching excitations. A lineshape analysis reveals that the anti-diagonal cross sections through (3200, 3200) and (3350, 3350) cm^{-1} for sample at 33% R.H. show linewidths comparable to those at 0% R.H., and an increase of around 40% for data at 92% R.H. (c.f. two lower rows of Figure 4-12). The NH stretching oscillators are subject to fluctuating long-range Coulomb forces exerted by the ionic phosphate groups in the DNA backbone, the counterions, and the water molecules in the hydration shell, and, thus, undergo vibrational dephasing, reflected in the 2D lineshapes. The absolute values of the anti-diagonal width of the NH stretching peaks of 30 to 50 cm^{-1}, corresponding to a Lorentz width from 45 to 70 cm^{-1}, clearly point to a decay component in

the frequency-frequency correlation function on a time scale of a few hundreds of femtoseconds.

The comparable width of the data at 0 and 33% R.H. suggests that, up to this hydration level the water molecules are mostly attached to the phosphate groups and far away from NH groups. When the relative humidity is increased to 92%, the first water shell around the phosphate group is complete and the water molecules start to approach the base pairs and are located relatively close to the NH groups, which is in agreement with the FTIR measurement [87, 88]. The moderate changes of the lineshapes of NH stretching oscillators when the relative humidity goes from 0 to 92% R.H. implies that the fluctuation forces, originating from the DNA structure itself instead of those from the water molecules, play a predominant role in their vibrational dephasing process. Since the translational and rotational motions of the double helix structure are too slow to induce a sub-picosecond dephasing, the frequency spectrum of the fluctuating force is governed by motions along vibrational degrees of freedom. The vibrational spectrum covers a very broad frequency range from 1 cm^{-1} for highly delocalized motions along the helix backbone up to around 3500 cm^{-1} for the NH stretching modes. Both experiments and theory have shown that delocalized vibrations of the backbone and motions of the counterions relative to the DNA helix happen in the frequency range up to 200 cm^{-1}. Such modes involve large-amplitude elongations of the charged counterions and phosphate groups, and should dominate the low-frequency spectrum of the fluctuating Coulomb forces. The different bending and stretching motions of the phosphate ions are of smaller amplitude and occur between approximately 400 and 1300 cm^{-1}, complemented by a large number of fingerprint modes of the sugar groups and base pairs extending up to frequencies of approximately 1750 cm^{-1}. At room temperature (thermal energy kT=200 cm^{-1}), thermally excited modes below 600 cm^{-1} play a key role for the fluctuating Coulomb forces and give rise to the fast dephasing of the NH stretching excitations. A thorough analysis of dephasing by DNA motions requires theoretical calculations of the vibrational force fields in combination with molecular dynamics simulations of the microscopic motions.

It is interesting to see the limited effect of water fluctuation upon the dephasing of NH stretching oscillators. Based on the previous study, the water molecules favor the phosphate group on backbone [87, 92] or the minor groove of base pair[89], both far away from the NH_2 group of adenine in major groove, when the hydration shell is incomplete. For full hydration level, R.H. 92% in our case, the water molecules has completed the first hydration shell and

hydrated both minor and major grooves of the base pair. Therefore, an interaction between water molecules and NH group of the bases is possible. The strongest local interaction of the NH of thymine is the hydrogen bond to the N1 atom of adenine, a structure that is hard to be affected by the water shell and remains unchanged on the time scale we studied. The NH_2 group of adenine forms a second hydrogen bond with CO group of thymine but offers a free NH unit accessible for forming an intermolecular hydrogen bond with a water molecule in the major groove of double helix. The x-ray diffraction data suggested that this interaction is very weak, with N…O distance bigger than 0.35nm, as water molecules interact more strongly with the neighboring N7 position of the adenine structure [11, 89]. Moreover, MD simulations indicated that (i) the reorientation dynamics of water molecules attached to base pairs in the major grooves occur in the picosecond time domain with a 1 ps component representing the fastest decay component of the dipole-dipole time correlation function and averagely 6 ps rotational time, and (ii) the majority of hydrogen bonds between water shell and DNA bases in the major groove have lifetimes more than 4 picoseconds. This suggests that fluctuations of the local water structure around the NH_2 groups are too slow to contribute to the sub-picosecond spectral diffusion.

4.4.3 Vibrational Dynamics of Water Shell around DNA Oligomer

The reshaping of overall lineshapes of the absorptive 2D IR spectra is evident, when the diagonal peak D2 becomes tilt away from the diagonal, and the left side of 2D plots, where ν_3 is smaller than 3300 cm^{-1}, becomes more intense as a function of population time T. The anti-diagonal cross sections through (3350, 3350) cm^{-1} suggest that the reshaping happens mainly to a broad band underneath the asymmetric NH_2 stretch of adenine. This points out that the reshaping of the 2D spectra is dominated by the reshaping of components contributed by OH stretching oscillators, as a behavior of spectral diffusion. In contrast, the NH groups undergo rather limited spectral diffusion at same time. Thus, the different behavior of the overlapping patterns hinders a detailed analysis of the spectral diffusion of the OH stretches.

When the excitation frequency is shifted up to 3400 cm^{-1}, the 2D spectra are strongly dominated by the excitations of OH stretch modes and, thus, give specific insight into spectral diffusion in the hydration shell around DNA. The 2D spectra of neat H_2O measured at a temperature of 304 K are used as a reference [47]. As the population time evolves, we observe a reshaping from an initially elliptic spectral envelope along the diagonal to an essentially

round envelop at late T in both hydrated DNA and neat water. This behavior is typically related to spectral diffusion that randomizes the OH stretching frequencies.

In the hydrated DNA, the reshaping occurs continuously in the measured population time of 500 fs, and probably continues on a longer time scale. In contrast, the spectral diffusion of OH stretching excitations in neat water occurs to major extent within the first 100-200 fs after excitation. The slowing down of the spectral diffusion in the hydrated DNA is evident when comparing spectral cross sections of the two sets of spectra. The cross sections along the anti-diagonal going through (ν_1,ν_3) = (3350, 3350) and (3380, 3380) cm^{-1} exhibit a time dependent broadening towards lower detection frequencies, which is a hallmark of the spectral diffusion of the OH stretching excitation. In neat water, the anti-diagonal width increases strongly in the first 100 fs and the bandwidth changes only slightly from T=100 to 200 fs. In contrast, the water shell of DNA exhibits spectral dynamics slowed down by at least a factor of 2 to 3, with the anti-diagonal width increases considerably after T=300 fs and probably increase further after 500 fs.

For a more quantitative analysis, the slope of the center lines of the 2D spectra of DNA/water is considered and compared to results of the neat water [134]. The slopes of the center lines reflect the frequency-frequency correlation function (FFCF) of the fluctuating ensemble, as we have discussed in section 2.5.4. In Figure 4-15(c), we plot the center line slopes, derived from a linear fit of the center lines of the 2D spectra of the DNA and the neat water with the excitation at 3400 cm^{-1} in Figure 4-14, as a function of T. The values of the slope of both systems start similarly at 0.6 at T=0 fs. While the neat water data exhibit a rapid decay within the first 50 to 100 fs, the DNA/water has a much slower decay process which is dominated by a gradual and incomplete decay extending over a period of 500 fs. The quick decay in the short time has been attributed to the spectral diffusion caused by librational motions of water molecules [47, 135]. For comparison, the FFCFs of OH stretching excitations of bulk water as calculated from molecular dynamics simulations are presented in Figure 4-15(c). The solid line ($C_p(t)$) is the result of a calculation considering resonant energy transfer between OH stretching oscillators while the dashed line (C(t)) neglects this process. The comparison of the neat water results with the calculated correlation functions shows that the slope decay in good agreement with the $C_p(t)$. However, the DNA-water system shows that the amplitude of the sub-100fs component is strongly reduced and the subsequent time evolution between T=100 and 500 fs is closer to C(t) than to $C_p(t)$. In particular, the pronounced decay of $C_p(t)$ between 70 and 600 fs is absent in the DNA/water data.

In contrast to the TRSS studies of chromophores linked to DNA, where different contributions are hard to be separated, our results give specific information on the dynamics of the hydration shell around DNA because the OH stretching excitations probe the water response selectively. The water shell of highly hydrated DNA consists of two different kinds of water molecules, (i) the highly heterogeneous first layer of water molecules attached to the DNA and (ii) the more bulk like water as the second layer of water molecules attached to the first one. In general, water molecules in the hydration shell are different from bulk water in several perspectives. First the concentration of water in our fully hydrated sample is of the order of 10 M compared to 56 M in bulk water. Therefore, resonant energy transfer is strongly hindered at such low concentration. Extrapolating from an experimental results studying resonant energy transfer in diluted OH stretching oscillators (HOD in D_2O, ref [136]), one can estimate energy transfer times in the order of picoseconds within the water shell which are longer than the subpicosecond vibrational lifetime of OH stretching oscillators. As a result, the more or less suppressed resonant energy transfer has limited contribution to the decay of the FFCF. This is particularly relevant for population times between 70 and 600 fs where the decay of the calculated correlation function is strongly influenced by resonant energy transfer.

Secondly, a substantial fraction of the water molecules forming the primary hydration shell, which needs 18-20 water molecules per base pair, is strongly attached to the particular DNA. Thus, such strong bonds can slow down or even suppress orientational and rotational motions of water molecules. For instance, the molecules in the ‘spine of water’ attached to the minor groove of AT base pairs, as identified in x-ray scattering [11], are sterically immobilized and hydrogen bonds have much longer lifetimes than in bulk water, according to NMR measurements and MD simulations of correlation functions of hydrogen bond lifetimes. The partial suppression of low-frequency water motions and the longer hydrogen bond lifetimes directly affect the fluctuating Coulomb forces and result in a slowing down of the different decay components in the frequency fluctuation correlation function of the OH stretching excitations. On the other hand, our results suggest a decay of the FFCF on a time scale between several hundred femtoseconds and a few picosecond, i.e., the extent to which structural fluctuation of water shell are slowed down, is limited.

Such slowing down of spectral diffusion was also found in theoretical simulation of water dynamics at DNA surfaces [107]. An analysis of polar solvation of electronic dipole excitations gives decay times of the FFCF of 0.4 and 2.7 ps in the electronic ground state. The decay time primarily describes the motion of mobile group of water molecules that solvate the

DNA sugar phosphate backbone and the probe itself. A further analysis suggests that solvation is dominated by the water molecules in the first, while the response of the second hydration shell is small but significant. It should be noted that attaching an organic chromophore to DNA changes the structure of both the DNA helix and the hydration shell, thus, affecting hydration dynamics. An analysis of this issue can be found in Ref. [103]. It shows that the replacement of an AT pair by a coumarin chromophore results in a widening of the minor groove, an increased mobility of water molecules, and a shortening of reorientation times. Further theoretical calculations and simulations are required for an in-depth comparison with our experimental results.

The distortion observed at the high frequency side of the center lines, as well as the negative signal on the right side of the 2D spectra with excitation at 3250 cm^{-1}, provides information about the energy dissipation in hydration shell. The distortion is due to the rising of the negative signal which is attributed to the formation of hot ground states. The hot ground state v=0' is usually defined as a state to which the excited vibration, in our case OH stretch as confirmed by the fact that the negative signal peaks at ν_1=3400 cm^{-1} close to the maximum of absorption of OH stretches, relaxes when its excess energy is passed to the immediate environment or its own low frequency modes and then delocalized in the hydrogen bond network. This excess energy in such modes will increase the temperature of the environment, from which the name 'hot' ground state comes from, and leads to an overall increase of the distances between the acceptor and the donor in the hydrogen-bonded systems. After the excitation of OH stretches, they decay not to the original ground state which persist the original v=0→1 transition frequency but to the hot ground state which has different v=0'→1' transition frequency. Thus, the vacancies of the ground state are not refilled and the ground state bleaching signal preserves with the appearing of signal of the hot ground state absorption. As a result, we will observe a reduction of v=0→1 transition and an enhancement of v=0'→1' transition. In bulk water, it has been proven that the coupling between the OH stretches and the v=2 overtone of OH bending is most efficient [137] and the cascaded decay of the OH stretching vibration via the v=2 and v=1 states of the OH bending mode and the concomitant disposal of excess energy into intermolecular modes of the hydrogen-bond network has been demonstrated by femtosecond pump-probe experiment [138]. Some theoretical studies have shown that the v=1 OH bending excitation predominantly decays into a hindered rotation of the bend-excited molecule [139, 140]. Their decay leads to a local weakening of hydrogen bonds around the excited molecules, followed by a slower delocalization of excess energy in the network of the order of 1 ps which results in a hot

ground state. The lifetime of a hot ground state is usually much longer than that of the v=1 excitation. Thus the population at hot ground state is increasing and the vacancies in ground state last for much longer time. As a result, we observe in our experiment that after 700 fs more signal of the diagonal peak residue for samples at higher hydration level compared to lower hydration level and the negative signal is present and increasing in the right side of the 2D spectra. The blue shift of the frequency of v=0'→1' transition compared to v=0→1 transition is due to that the strength of the hydrogen bonds is weakened upon the increased distance between the acceptor and donor [138, 141]. The process can be described by the five-level scheme and double-sided Feynman diagrams in Figure 4-18. As depicted in the five level scheme, the formation of the hot ground state is decided by the population life time of v=1 state. The decay of the hot ground state usually depends on the cooling process of the system, which takes up to hundreds of microseconds to redistribute the energy out of the interrogated volume.

In order to study the dynamics of the hot ground state, the cross sections along ν_3 at ν_1=3400 cm^{-1} are shown in Figure 4-17. They show that while the negative signal at ν_3<3200 cm^{-1} decreases as a function of population time T the negative component at ν_3>3450 cm^{-1} starts to emerge and getting stronger. The integrations of two components show similar dynamics. The single exponential fittings of both dynamics give a time constant of 200 fs. The long term cooling process usually takes much longer time, and thus is out of the scope of our experiment here. The subpicosecond kinetics of the components confirms that the buildup of the hot ground state is initiated by the decay of the OH excitation of water. Considering the spectral position of OH stretching oscillators in hydrated DNA being similar to that in bulk water, the

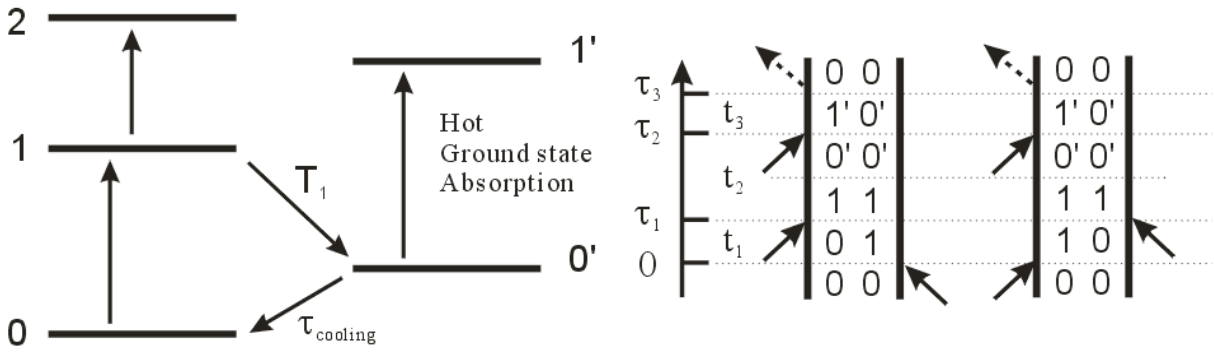

Figure 4-18: (a) 5 level scheme included hot ground states. (b) Feynman diagrams of 3rd order processes depicting the formation of hot ground state. Instead of refilling the ground state, the excited vibration relaxes to hot ground state in population life time T_1, and contributes a hot ground state absorption signal. The life time of a hot ground state is usually of hundreds of microseconds.

energy mismatch to the v=2 overtone of the OH bending vibrations is similar to that of the bulk water too [142]. Thus one would expect that the lifetime of OH stretching oscillators is close to that of bulk water of order of 200 fs [143], which is supported by the experimental results. It is important to note that the buildup of the hot ground state matches the decay of the excitation of the OH stretching oscillators. This time evolution of hydration shell around DNA is close to bulk water, indicating a fast randomization of excess energy. A similar behavior in the water shell has been observed in experiments using the asymmetric stretching vibration of phosphate groups in the DNA backbone as a probe of energy dissipation.

4.5 Conclusions

In this chapter, the ultrafast vibrational dynamics in electronic ground state in 23 mer AT oligomer at different hydration levels were studied. The 2D infrared spectra for a wide range of hydration levels allow for a clear separation of the response of NH stretching vibrations of DNA from the ultrafast dynamics of OH stretching excitations of the water shell.

At 0% R.H., when there are few water molecules in the sample, we were able to dissect the spectrally overlapping NH stretching modes according to their different peak shapes due to their different broadening mechanism. The NH_2 stretching modes of adenine, described as symmetric and asymmetric stretching modes, are mainly inhomogeneously broadened, because the free NH units sticking out of base pairs are sensitive to the structural disorder. The NH stretching mode of thymine is homogeneously broadened, for it is hidden in the base pair and protected from the outside fluctuations. The dominant energy transfer by dipole-dipole coupling favors a transfer from asymmetric NH_2 stretch of adenine to the NH stretch of thymine because of their relative close distance and small angle. The transfer occurs in the time scale of the order of 0.5 ps, corresponding to a coupling strength of the order of 5 cm^{-1}. The energy transfer between base pairs was not observed.

Taking the results of dry sample as a benchmark, the results obtained from samples at higher humidities were analyzed. Regarding the NH stretches, the spectral position and lineshape were not much modified as hydration level increases with the main difference being the moderate broadening of anti-diagonal line width. The energy transfer from the asymmetric NH_2 stretch of adenine to the NH stretch of thymine persists too. These point to the limited influence of the extra water molecules on the NH stretches in AT base pair when the hydration level increases, thus we can suggest that the NH stretching excitation are essentially localized

to the particular base pair that undergoes minor geometry change upon hydration. Moreover, it points to a limited influence of water fluctuations on such modes, a behavior that is in line with the relatively slow structural dynamics of water molecules in the first hydration layer around the thymine NH and adenine NH_2 groups. Instead, fluctuating forces originating from the DNA oligomers and their counterions are considered the main mechanism of the subpicosecond NH stretch dephasing.

Unlike the strongly hydrogen-bonded water molecules in DNA sample at R.H. 0%, which undergo negligible spectral diffusion, the spectral diffusion of the water molecules in DNA sample at higher humidity is significant. This indicates the formation of a network of water molecules when the water content is increased. A quantitative analysis of the center line slopes of the 2D spectra shows that the spectra diffusion is slower than that of neat water by a factor of 2-3. Comparison with the calculated FFCF reveals the strongly reduced amplitude of the sub 100 fs decay, and a slowed down decay in subsequent 500 fs. This behavior is attributed to the reduced resonant energy transfer due to the smaller network in DNA/water system than in bulk water, and the suppression of local interaction such as rotational and translational motion due to the hydrogen bonds with the DNA molecules. The observed limited slowing down of the water response compared to bulk water is in line with molecular dynamics simulations of DNA hydration but rules out a slowing down by orders of magnitude in time.

When the vibrational excited OH stretches in water relax, the excess energy is mostly efficiently redistributed into local environment or its own low frequency mode, resulting in hot ground states. This hot ground state induces a blue shift of fundamental transition, attributed to the increase of distance between water molecules and weakening of hydrogen bonds. The formation of hot ground state is in a time scale on the order of 200 fs, close to that of bulk water. The fast formation of hot ground state points to the fast randomization of excess energy, close to the behavior of neat water.

Such results give rich information about the structure of DNA/water system, which attracts interest for decades, in a timescale of sub-picoseconds. As an oligomer containing only adenine and thymine, it could serve as a model system for people to understand the much more complicated structure of native DNA. The energy transfer process helps to understand the redistribution of excess energy in DNA, and the mechanisms protecting our sophisticated inheriting system from being hurt by external radiation.

5. Ultrafast Ultrafast Vibrational Dynamics of Base Pairs in Solution

5.1 Introduction

Two distinctive supermolecular structural motifs can be distinguished when considering interactions in DNA double helixes: (i) nucleobase stacks, and (ii) nucleobase pairs. By studying 1:1 complexes of the nucleobases, either in gas phase or in weakly interacting solvents, it is possible to specifically investigate the hydrogen-bonded interactions, distinct from the other forces involved in double-strand formation. Thus, the results can serve as a benchmark for further research on more complex systems containing sugar groups or backbones and stacking nucleobases, which bring more interactions. The structures and dynamics of such systems have been investigated with a variety of experimental methods, including NMR [144], IR [145-147], resonant two-photon ionization [148, 149], fluorescence up-conversion [150, 151] spectroscopy as well as theoretical calculations [125, 152-156].

Some femtosecond transient absorption [157, 158] and fluorescence upconversion [159, 160] experiments have shown that the electronic energy from exciting the isolated base pairs to the S_1 state, which can be potentially damaging, is converted into vibrational energy in the S_0 state on a time scale of a few hundred femtoseconds. However, this dynamics is strongly dependent on the base sequence, or even higher structure in double helix[151].

Woutersen et al. have done a time-resolved IR spectroscopic experiment on the adenine and uracil base pairs in solution [161], which showed that the vibrational relaxation of the NH stretching modes is a factor 3 faster in the adenine-uracil base pairs than in the uracil monomers. They also observed that the hydrogen bonds between the pairs accept part of the energy of the NH stretching mode. The first-principles quantum calculations of Yagi on guanine-cytosine base pairs [155] attributed this enhanced relaxation to the Fermi resonance between the NH stretching mode and the overtones and combination tones of the fingerprint modes. However, this is still not proven experimentally. Moreover, the interactions between the different NH stretching modes are not known either.

Here we use the bottom-up approach to studying the structure of the DNA molecules, which starts with the nucleobases themselves as molecular systems [125, 145, 146, 153, 162-167], or

model compounds [168-171], to study the hydrogen bond complexation. By putting nucleobases into the solvent, it is possible to control the molecular design of nucleobases derivatives to some extent [161]. Moreover, the solvent is not necessarily water, which has a broad absorptive band of the OH stretching strongly overlapping with the NH stretching of nucleobases and hinders a reliable analysis of hydrogen bonding induced changes [32, 112, 113]. However, the disadvantage is little controlling on the more possible structures, such as multiple hydrogen-bonded structures [165, 168, 169] and keto-enol tautomerizations [145, 146, 165, 166, 172, 173].

In this chapter, we will study the vibrational dynamics of Guanosine-Cytidine (GC) base pairs in their electronic ground state by a 2D IR experiment.

5.2 Experimental

Sample preparation: The hydroxy groups of the ribose units in guanosine (denoted as G) and in 2'-deoxycytidine (denoted as C) are substituted by *tert*-butyldimethylsilyl (TBDMS). The bulky nonpolar side groups make the modified nucleosides highly soluable in aprotic solvents. The aprotic solvents $CHCl_3$ and $CDCl_3$ are chosen, because they do not interfere with the formation of the hydrogen bonds in base pairs. The solvent was dried by molecular sieves for days before use, to prevent competition at the hydrogen bonding acceptor and donor sites of the bases with unwanted water in the solvent.

Stationary spectroscopy: Linear IR spectra were taken in both $CDCl_3$ and $CHCl_3$. $CDCl_3$ is employed to avoid the very strong peak of CH stretching modes, which dominates the spectral region around 3020 cm^{-1}. On the other hand this solvent has an overtone absorption at ~3150 cm^{-1}, and therefore measurements in $CHCl_3$ are needed for an accurate determination of the spectral shapes in this region. The solution was kept between two 1 mm CaF_2 windows, separated by a Teflon spacer with a thickness of 100μm. The spectra were measured with a Varian 640 FT-IR spectrometer, applying a concentration range of 2-50 mM.

Ultrafast experiments: The solvent $CHCl_3$ was used, because of the overtone transition in $CDCl_3$ that strongly overlaps with the 3145 cm^{-1} peak of GC. The long tail of the strong CH absorption still overlaps with the peak 3145 cm^{-1}. For both G and C the concentration is 100 mM in the solution in photon echo measurements, whereas they have a 50 mM concentration in pump probe measurements. The different concentrations in the photon echo and the pump

probe measurements do not change the ratio of different components in the solution according to FTIR spectra. The solution is kept in the commercial Harrick static sample cell between two 1mm CaF_2 windows, separated by a Teflon spacer with a thickness of 100 μm. The absorption of the sample is around 0.5 OD for the peaks at 3303 cm^{-1} and 3491 cm^{-1}, and around 1 OD for the peak at 3145 cm^{-1} because of the higher extinction coefficient as well as the overlapping with the pronounced tail of the CH absorption of the solvent.

Femtosecond infrared pulses were generated in the light source discussed in section 3.1. The photon echo and the pump probe setup were introduced in section 3.3 and 3.4. The spectrum of the pump pulse was centered at 3250 cm^{-1}, with a bandwidth over 300 cm^{-1} and covering all the studied bands simultaneously, as shown by the dashed line in Figure 5-1. The time resolution is 60 fs according to the FROG measurement.

The coherence time range scanned in photon echo experiments is from -600 fs to +800 fs, resulting in a acceptable lineshape with some little oscillating shoulders for the narrowest peak at 3491 cm^{-1}.

5.3 Results

The steady state spectra of the GC mixture and of solutions of G and C alone are presented in Figure 5-1. All the spectra have been corrected by subtracting the absorption of the solvent. The concentration of the GC mixture in the solution is 50 mM, where they preferentially form GC base pair in the Watson-Crick geometry as established (therefore, we can call it GC base pair in the following). The concentration of the G and C only samples is 2 mM. Even though we call them G and C monomer in the following, G already dimerizes significantly at these low concentrations. For C on the other hand the monomer does dominate the spectrum at 2 mM.

In the spectrum of C monomer, which has only one NH_2 group, there are two narrow bands at 3418 cm^{-1} and 3534 cm^{-1}. The bundle of peaks between 2800 cm^{-1} and 3000 cm^{-1} are assigned to the CH stretching bands of the TBDMS side groups. The two narrow bands correspond to the symmetric and asymmetric stretching vibrations of the non-hydrogen-bonded NH_2 group in solution, reflecting the dominating role of monomers in the solution. In the spectrum of G monomer, which has one NH_2 group and one free NH, the symmetric and asymmetric stretching bands are still observable, located at 3411 cm^{-1} and 3521 cm^{-1}. In addition, two

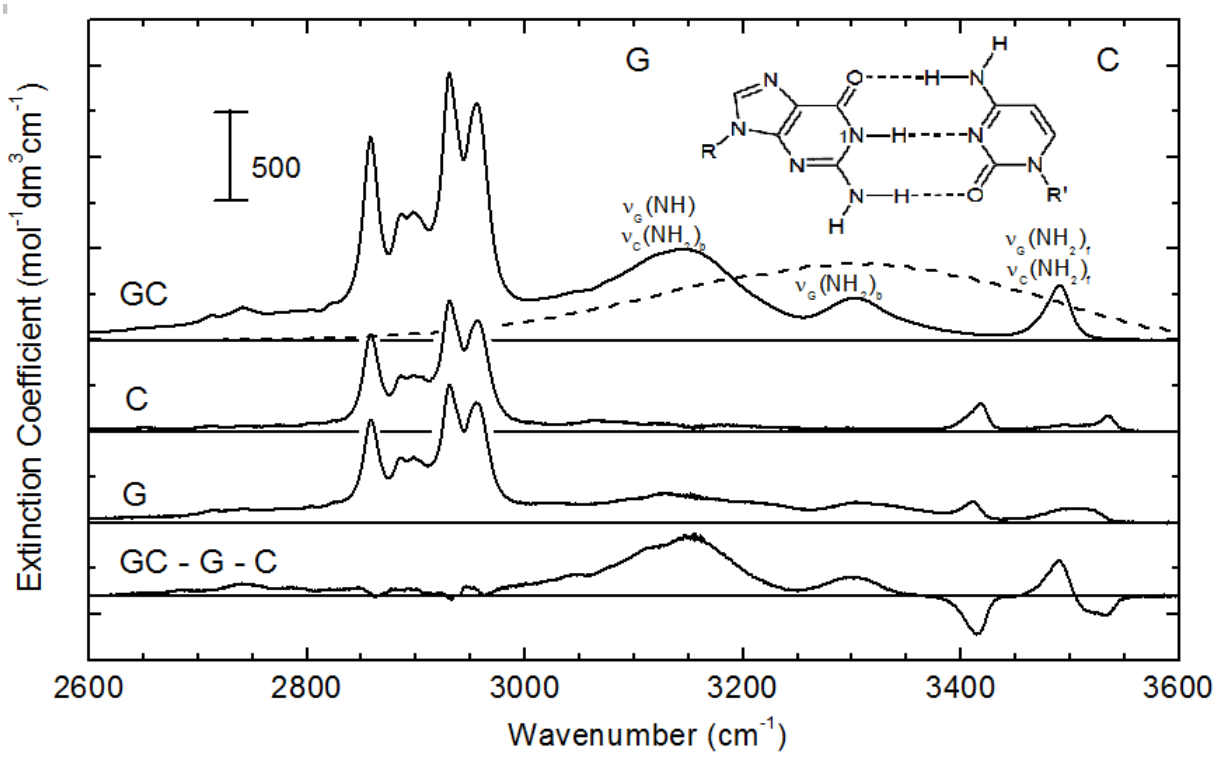

Figure 5-1: Linear infrared spectra of GC base pair and C and G monomers dissolved in $CDCl_3$ (from top to bottom). The extinction coefficient is plotted as a function of wavenumber, the sample concentration were 50 mM (GC base pairs), 2 mM (C) and 2 mM (G). The bottom-most panel shows the difference spectrum GC-G-C. Inset: structure of the GC base pair in Watson-Crick geometry. Dashed line: spectrum of the excitation pulses in the 2D experiments.

broad bands between 3000 cm^{-1} and 3400 cm^{-1} appear, indicating that the formation of GG dimers is not negligible. The secondary amino NH stretching band, suggested to be located in the gas phase at 3340 cm^{-1} [150], may be located underneath the broad bands of GG dimer and is not observable. In the spectrum of GC base pairs, three pronounced peaks are observed in the range 3000 cm^{-1} to 3600 cm^{-1}. They center at 3145 cm^{-1}, 3303 cm^{-1} and 3491 cm^{-1}, with bandwidth of 174 cm^{-1}, 84 cm^{-1} and 27 cm^{-1} respectively, and point out the formation of hydrogen bonds in NH group in GC base pairs. All these bands exhibit asymmetric lineshapes.

There could still be hydrogen-bonded NH stretching bands potentially hidden under the strong CH stretching bands between 2800 cm^{-1} and 3000 cm^{-1}. As the same CH stretching bands patterns are also observed in G and C monomer solutions, we can subtract the contribution from the monomers to see if there is anything left which can be attributed to the dimers. In doing so we assume that the spectral position, cross section and lineshape of the CH stretches are not affected by the dimer formation, since they are far away from the hydrogen bond sites. It turns out that there is no significant other IR absorbance in this range. Therefore, we

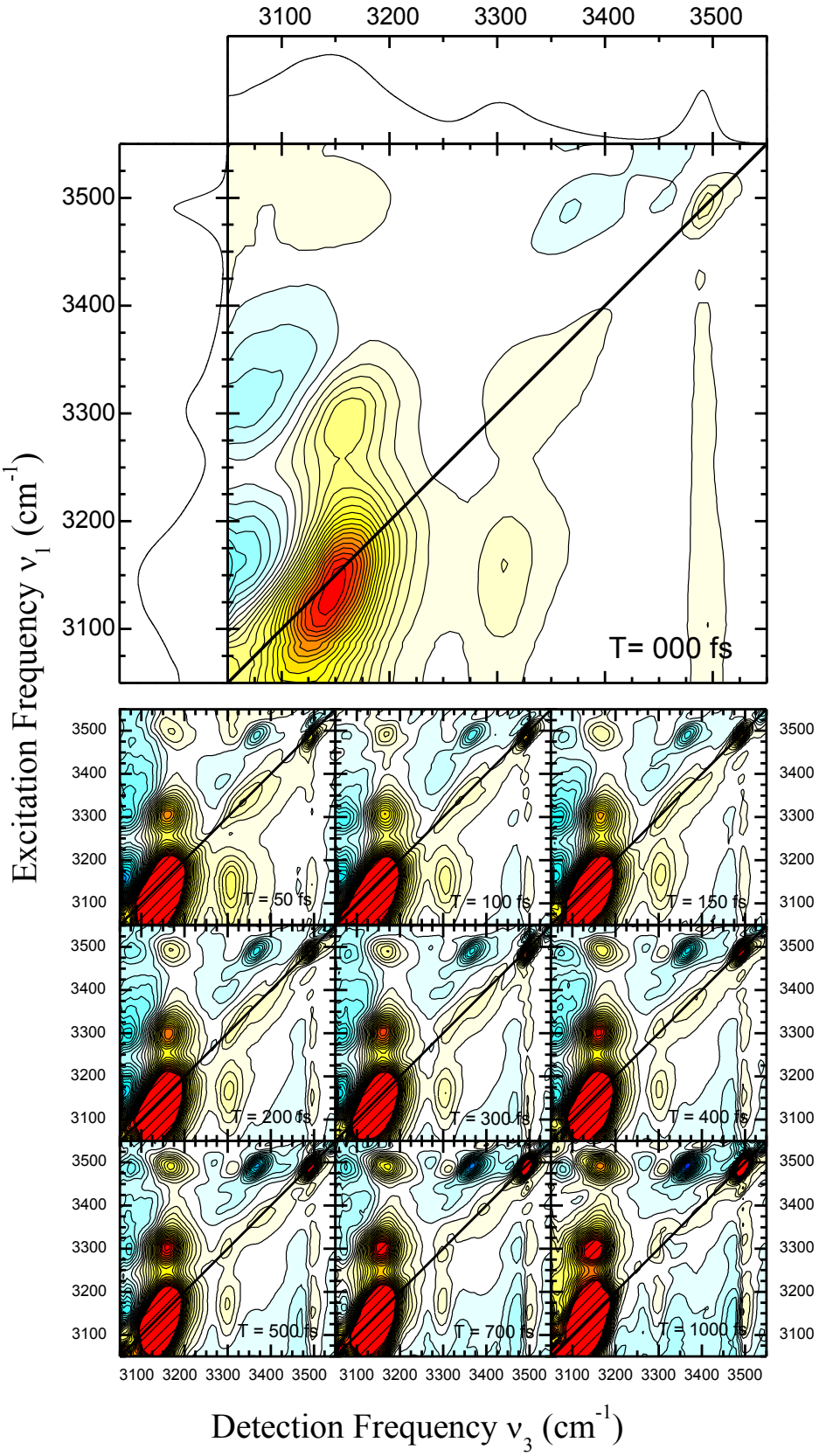

Figure 5-2: The absorption part of the 2D IR spectra recorded for different population waiting times T. The plots are scaled for one third of the maximal signal strength for each value of T. For comparison with the locations of IR-activate NH stretching transitions, the FTIR spectra of the sample (100mM GC in $CHCl_3$), corrected for solvent contribution, are plotted on the left and the top of 2D spectra for T = 0 fs.

conclude that the five NH stretching bands contribute mostly to the spectral range between 3000 cm^{-1} and 3600cm^{-1}, with three absorption band maxima at 3145, 3303 and 3491 cm^{-1}.

The real parts, i.e. absorption parts, of the 2D-IR measurements on GC base pairs are presented in Figure 5-2, and are arranged in order of increasing population time from 0 fs to 1000 fs. The left and top panels of T=0 fs show the solvent corrected linear spectrum of the solution studied in the experiment. Several peaks are observed with different intensities and lineshapes. The scale of the plot at T=0 fs is normalized to the highest intensity of the peaks and each contour represents a 5% change in intensity. In contrast, the scales of the results when T>0 fs are truncated at one third of the highest intensity of the peaks in order to give more details of the signals which are much weaker. The saturated signal is denoted as striated red area.

On the diagonal of the 2D spectra, where the excitation frequency equals the detection frequency, three pronounced positive peaks are observed in red and yellow. They are located at ($\nu_1[cm^{-1}]$, $\nu_3[cm^{-1}]$) = (3145, 3145), (3303, 3303), (3491, 3491) cm^{-1}, corresponding nicely to the three peaks observed in the linear spectrum. When T=0 fs, the peaks at (3145, 3145) and (3491, 3491) cm^{-1} exhibit a shape slightly elongated along the diagonal, while the peak (3303, 3303) has a rounder maximum with a tail elongating along the diagonal at higher frequency. The lineshapes of peaks (3145, 3145) and (3491, 3491) do not change significantly when time evolves within the accuracy of the measurements while the peak (3303, 3303) becomes distorted and seems to split into two, one staying at (3303, 3303) and being rounder whereas the other with a broad maximum fluctuating around (3375, 3375) appears elliptical. All the plots are scaled to the intensity of the peak at (3145, 3145), and therefore the apparent increase in relative magnitude of peak (3491, 3491) with increasing population time T, and decrease of (3303, 3303) indicates longer and shorter population lifetimes for these two transitions, repectively.

In the off-diagonal area, there are two kinds of signals appearing, which differ in sign (positive or negative). In contrast to the positive peaks, the negative peaks, which are shown in blue, represent enhanced absorptions such as excited state absorption. The positive off-diagonal peaks are located at ($\nu_1[cm^{-1}]$, $\nu_3[cm^{-1}]$) = (3145, 3303), (3303, 3145), (3145, 3491) (3491, 3170), (3303, 3491) and (3491, 3303), as the positive components of the cross peaks between two different frequencies; the negative peaks are located at ($\nu_1[cm^{-1}]$, $\nu_3[cm^{-1}]$) =(3145, 3040), (3145, 3462), (3303, 3062), (3303, 3462), (3385, 3300), (3491, 3074), (3491,

3272) and (3491, 3360), as the excited state absorption signals or the negative components of the cross peaks. The negative or positive contributions spreading around 3491 cm^{-1} along ν_1 are attributed to the truncation effect of the long-lived peak. The strong absorbing band of CH of the solvent $CHCl_3$ at 3020 cm^{-1}, as well as the strong overlap of the positive (3303, 3145) with the negative (3303, 3062), prevent us from studying the enhanced absorptions in full detail. The lineshapes of all the off-diagonal peaks stay unchanged with time too within the accuracy of the measurement. The off-diagonal peaks along ν_1=3491 cm^{-1} all appear to be increasing in relative magnitude with increasing population time T, similarly to the diagonal peak (3491, 3491). The theoretical calculation [125] predicted peak (3491, 3360) to be the excited state absorption of unbound NH peak at 3491 cm^{-1}, and the big anharmonic frequency shift of 130 cm^{-1} is not uncommon as the experimental observation for free NH stretching transitions of uracil [161] and 7-azaindole [170] showed a similar magnitude. In contrast, while the peak (3303, 3145) increases in relative magnitude for increasing population time, the other peaks with same ν_1 do not change dramatically.

For more detailed analysis of the peaks in the 2D plots, center lines were made by connecting the maxima of the cross sections along ν_1 as shown in Figure 5-3. In general, the slopes of peaks do not change significantly, indicating negligible spectral diffusion on a picosecond time scale.

The diagonal peaks at (3145, 3145) and (3491, 3491) cm^{-1} show considerable inhomogeneity with their center lines parallel to the diagonal at all population time. In contrast, the diagonal peak at (3303, 3303) cm^{-1} shows interesting dynamics. At T=0 fs, the lower part of the peak shows a flat center line parallel to ν_3 while the higher part has a center line parallel to the diagonal. Then the inconsistence of the center line disappears from T=50 to 200 fs and reappears again at T=400 fs. This suggests that the diagonal peak (3303, 3303) consists of actually two different peaks, with the lower one homogeneous and the upper part dominated by inhomogeneous broadening instead; the changing of the center lines is due to the different dynamics of the two components. Thus, we separate the peak (3303, 3303) into two peaks (3303, 3303) and (3380, 3380) respectively. This separation is corroborated by the center line of the off-diagonal peak at (3303, 3145) cm^{-1}, which exhibits relative flat slope with its maxima at ν_1=3303 cm^{-1} except at T=0 fs where it tilts due to the overlap with the negative peak at lower frequency side. Its flatness and the relatively narrow bandwidth of the cross section along ν_1 indicate that it corresponds to the lower part of the 3303 cm^{-1} diagonal peak.

The cross sections of the 2D-IR along the diagonal are shown in panel (a) of Figure 5-4 as a function of T. The positions of the three peaks are the same as those of the three absorption peaks in the linear spectrum, corresponding to the $\upsilon = 0 \rightarrow 1$ bleach. The peaks at 3145 and

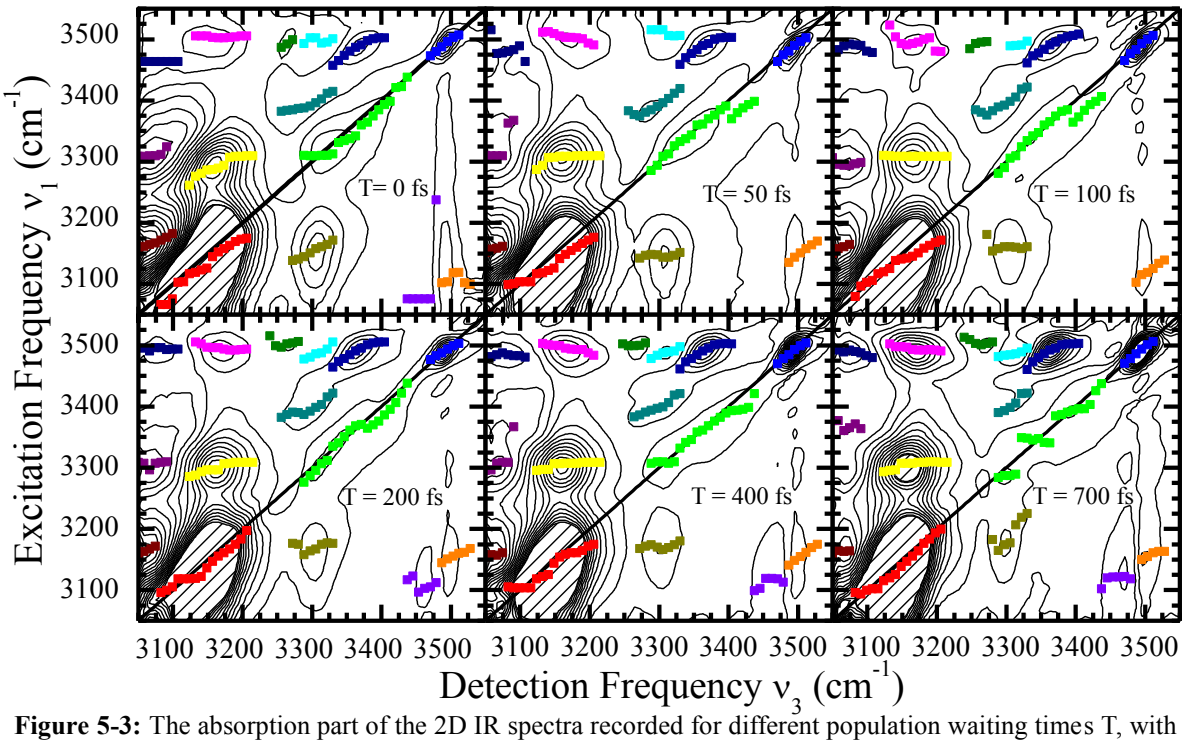

Figure 5-3: The absorption part of the 2D IR spectra recorded for different population waiting times T, with the center lines made from the maxima of the cross sections along ν_1. The different color indicate maxima of different peaks which may differ in sign.

3303 cm^{-1} decay significantly with the population time T, whereas the peak at 3491 cm^{-1} decays only slightly. The transient spectra attained in the pump-probe experiment are shown in Figure 5-4 (b) for comparison. The peak positions are noticeably identical considering the shift due to the overlap with the excited state absorption. Similar to the behavior of peaks in the 2D plot, the bleaching of the peak at 3145 cm^{-1} recovers relatively fast, whereas the recovery of the peak at 3491 cm^{-1} is much slower. The spectral range between 3250 and 3450 cm^{-1} is rather complex because of the overlap of broader bleaching signal of peak 3303 cm^{-1}, which recovers in 1 ps, with a narrow excited state absorption of peak 3491 cm^{-1} at 3360 cm^{-1}, which changes not as much on this time scale.

In the pump-probe experiment we derive effective time constants of the time evolutions at different frequency components contributing to the signals using multi-exponential fittings. The fitting curves are shown in panel (a) of Figure 5-5 and the results are summarized in Table 5-1. The bleach recovery at 3145 cm^{-1} occurs mostly with an ultrafast time constant of 0.34 ps, and then continues with a slower time constant of 2.4 ps. In the region between 3110 cm^{-1} and 3180 cm^{-1} the femtosecond component gradually increases from ~0.15 ps to ~0.5 ps

with increasing frequency and the slow picosecond component appears more prominent in low frequency end. The peak at 3491 cm^{-1} recovers with a single exponential component only, with the time constant 2.9 ps. From 3470 cm^{-1} to 3500 cm^{-1} the recovery time increases

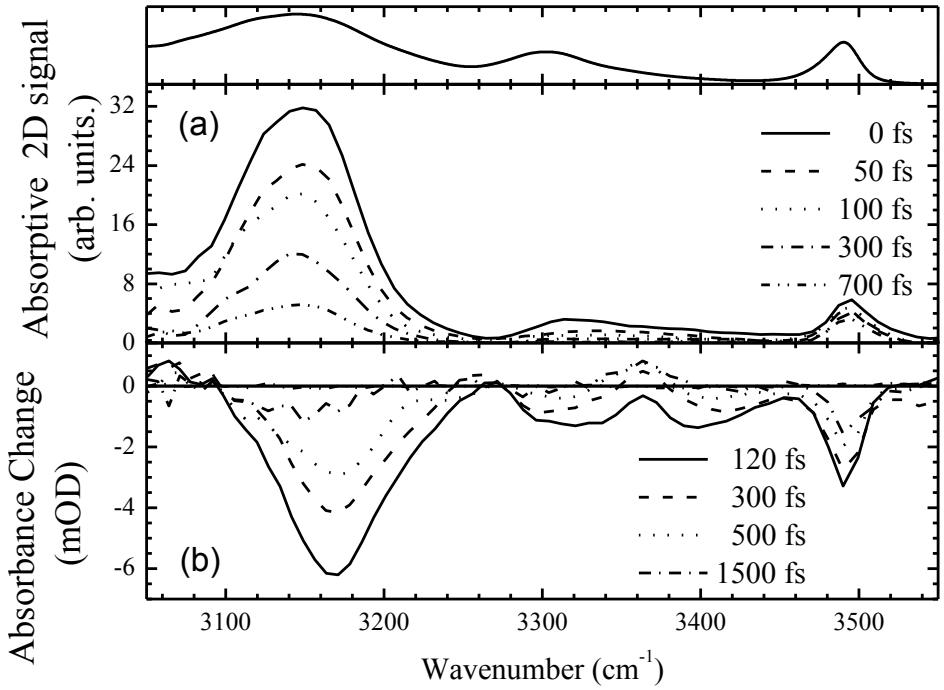

Figure 5-4: (a) The diagonal cross section of 2D spectra with x axis showing the detection frequencies, as a function of population waiting time T. (b) The transient spectra of pump-probe spectra, as a function of delay time between the pump and probe. To compare with the locations of IR-activate NH stretching transitions, the FTIR spectra of the sample (100mM GC in $CHCl_3$), corrected for solvent contribution, are plotted on the top.

monotonously from 1.1 ps to 3.6 ps, resulting in an average life time of ~2.4 ps. In the region between 3250 and 3450 cm^{-1}, it is difficult to disentangle the different spectral components from the complex overlapping. The kinetics of two spectral positions are fitted, which are at spectral position 3303 cm^{-1}, corresponding to the maximum of the linear absorption band, and 3360 cm^{-1}, which appears to be dominated by the excited state absorption of the band at 3491 cm^{-1}. The peak 3303 cm^{-1} recovers roughly with the single exponential component 0.27 ps, however the very low signal noise ratio makes it unreliable and the fittings at nearby positions give rather inconsistent results. Therefore what we can conclude is that the recovery occurs on a subpicosecond time scale. The dynamics of the peak 3360 cm^{-1} can be separated into two periods, the rise of the absorption due to the recovery of broad background bleach occurs with a 0.4 ps time constant, while the decay of the enhanced absorption due to the recovery of the narrow feature occurs in time scale of 2.5 ps. This complexity shows the limitation of the transient IR pump-probe spectroscopy, when the substantial overlap of spectral features

originating from different transitions hinders a more detailed study of the dynamics of the system. In contrast, 2D IR spectroscopy gives a much better view, as it separates different signals in a two-dimensional space according to their Liouville space pathways.

Table 5-1: Relaxation times and signal amplitudes determined by single or dual exponential fittings of the transient pump-probe and 2D FTIR spectra

$\nu(cm^{-1})$ Fundmental transition	A_1	T_1(ps)	A_2	T_2(ps)	Type of measurement
3145	-0.8	0.34	-0.2	2.4	Pump-probe
	0.9	0.27	0.1	Longer than 1 ps	2D FTIR
3303	-1	0.27	-	-	Pump-probe
	0.9	0.2	0.1	Longer than 1 ps	2D FTIR
3360	-1	0.4	1	2.5	Pump-probe
3380	1	0.3	-	-	2D FTIR
3491	-1	2.9	-	-	Pump-probe
(ν_1, ν_3) Cross peaks or ESA					
(3303, 3145)	1	0.8			
(3145, 3303)	1	0.2			

To quantify the temporal behavior of the peaks in 2D spectra, we integrated over the peaks in the 2D-IR spectra. The dynamics of the integrated intensities are summarized in Table 5-1. The integration of diagonal peaks (3145, 3145), (3303, 3303), (3380, 3380), and (3491, 3491) are shown in the panel (c) of Figure 5-5, and the off-diagonal peaks (3380, 3300) and (3491, 3360) are shown in the panel (d), as a function of population time T. The different excitation frequencies of the peak (3491, 3360) from (3380, 3380) help us to separate them nicely, in contrast to the pump-probe spectra. While the diagonal peaks (3145, 3145) and (3303, 3303) decay significantly in magnitude for population time up to1 ps, the peaks (3491, 3491) and (3491, 3360) has reduced only to 40 and 65% of their values at T=150 fs. By doing single exponential fitting, we can extract the time constants of 0.3 ps for the peak (3145, 3145) and 0.2 ps for the peak (3303, 3303), both with offsets which decay in a time much longer than the population time we have sampled in the 2D experiments. In contrast, the peak (3380, 3380) decays to 0 with a 0.3 ps time constant, which is slower than the 0.2 ps of (3303, 3303). The short lifetime of the diagonal peak at 3303 causes the disappearing of the flat center line at 50

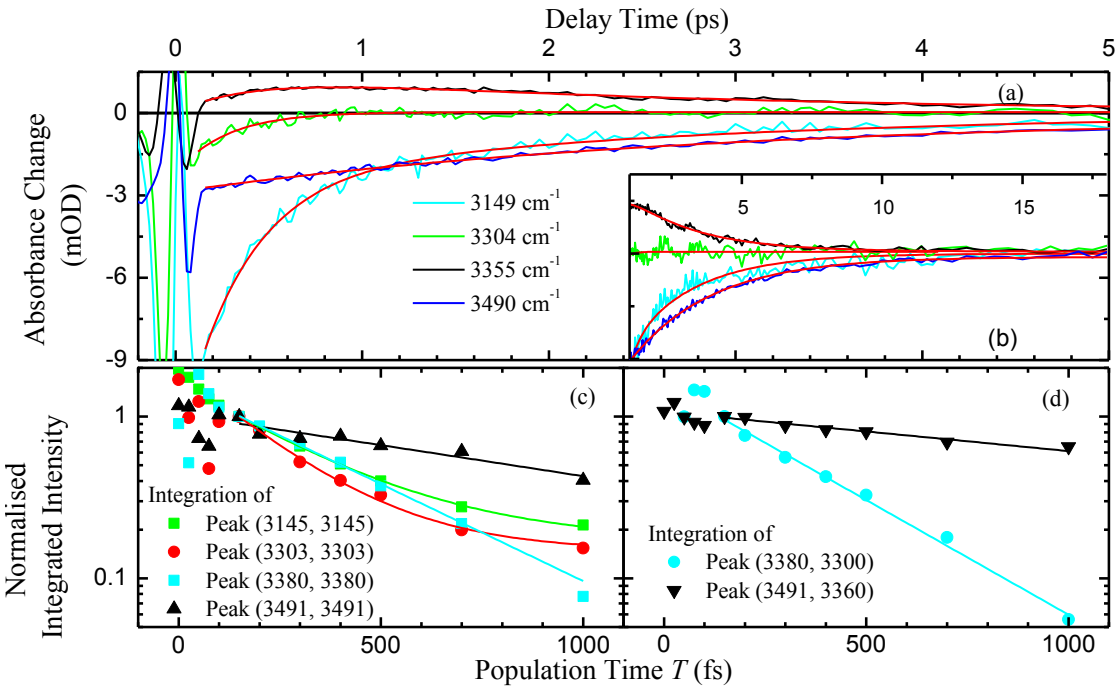

Figure 5-5: Panel (a) shows frequency-resolved pump-probe data as a function of pump-probe pulse delay time between -0.2 ps to 5 ps as to show the fast decays, while (b) shows the pump-probe pulse delay range from 1 ps to 18 ps to show the slow decays. Red curves are the (bi)exponential fitting results. (c) The temporal behaviors of diagnoal peaks (3145, 3145), (3303, 3303), (3380, 3380) and (3491, 3491) cm^{-1} and (d) The temporal byhaviors of off-diagonal peaks (3380, 3300) and (3491, 3360) cm^{-1} in the 2D spectra, obtained by integrating over the peaks, shown on a logarithmic scale. The solid lines are fitting results with single exponential decay.

fs, and the long-lived offset makes it reappear again at a later time. As the life times of the peaks (3491, 3491) and (3491, 3360) are clearly much longer than the sampling time, the fitting results would be anyway unreliable. And what we can conclude is that the life times of the peaks (3491, 3491) and (3491, 3360) area picosecond or longer.

The integrated intensity of off-diagonal peaks (3303, 3145), (3145, 3303) and (3491, 3170) are presented in Figure 5-6 (a) as the function of population time T. The first two off-diagonal peaks decay in a similar way in the first 150 fs, and differ thereafter. The peak (3145, 3303) keeps decaying very fast, while the peak (3303, 3145) slows down significantly. The time constants we derive from the second period using single exponential fitting are 0.8 and 0.22 ps respectively. It should be noted that the normalized integration of the entire peak (3303,3145) shows almost identical behavior as the integrals over higher or lower halves of the peak, meaning the tail of diagonal peak (3145, 3145) does not affect the decay kinetics of the off-diagonal peak (3303, 3145). However, the left half of the peak decays within a time of 1.1 ps while the right half decays in 0.6 ps. This indicates that the negative signal (3303, 3062) is overlapping with the peak (3303, 3145) and influences the kinetics of it. For the peak

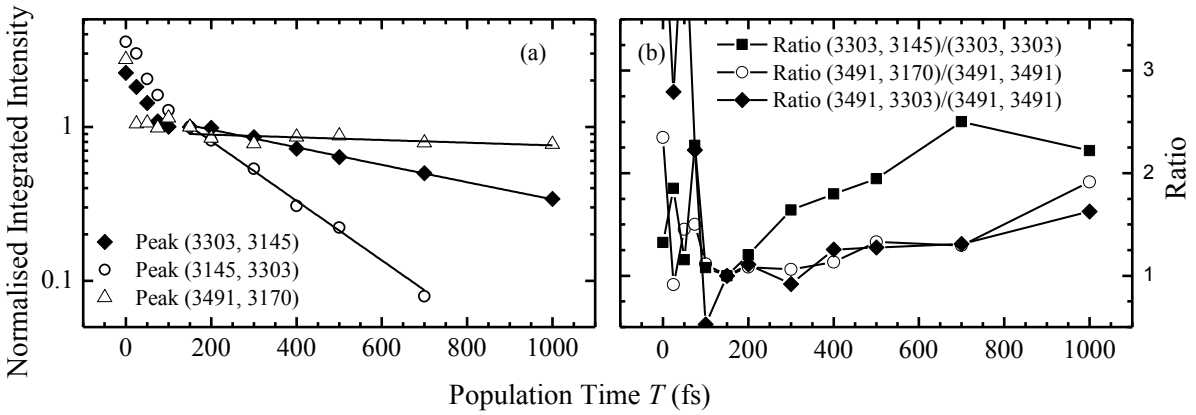

Figure 5-6: (a) Temporal behavior of off-diagnoal peaks (3303, 3145), (3145, 3303) and (3491, 3170) in the 2D spectra, obtained by integrating over the peaks, shown on a logarithmetic scale. The solid lines are fitting results with single exponential decay. (b) Ratio of the off-diagona peaks over corresponding diagonal ones shown in a linear scale.

(3491, 3170), a single exponential decay gives the time constant of several picoseconds, beyond the sampled population time in our 2D experiment. The ratio of the off-diagonal peak (3303, 3145) over the diagonal peak (3303, 3303) is shown in panel (b) of Figure 5-6 as well as the ratio of the off-diagonal peaks (3491, 3170) and (3491, 3303) over the diagonal peak (3491, 3491). While the ratio of (3303, 3145) over (3303, 3303) rises in 300 fs, both two latter ratios increase considerably only after waiting times T = 700 fs.

5.4 Assignments of NH stretches

In the weakly polar solvent like $CHCl_3$ and $CDCl_3$, the GC base pair is expected to adopt the Watson-Crick geometry, wherein the cytosine and guanine moieties adopt a planar structure [153, 154, 174] (Figure 5-1). This picture is supported by the concentration dependent infrared spectra discussed by the Temps group [150]. As shown in Figure 5-1, a GC base pair embeds five NH units, three of which are hydrogen bonded and two are left free. One of the NH units of the NH_2 groups from both G and C is hydrogen bonded to the CO group of the other base, while the other NH units of the NH_2 left free, and the secondary amine group of G is bound to the N of C. According to the results of density functional theory (DFT) calculations at the BP86/TZ2P level of the theory [154], the N···O distance is much shorter for the C(N-H)···G(O=C) hydrogen bond than for the G(N-H)···C(O=C), i.e., 2.73Å vs 2.87Å. This suggests that the C(N-H)···G(O=C) hydrogen bond is significantly stronger. This result is corroborated by DFT calculations by Wang et al. [125] on guanine-cytosine *in vacuo*. Wang et al. also calculated the vibrational stretching transition frequencies (shown as DFT[a] in Table 5-2). Nir et al.[166] made DFT Hartree-Fock calculations with the 6-31G(d,p) basis set

and a scaling factor 0.893, which are shown as DFT[b] in Table 5-2. A comparison of their calculation results with the experimental results is presented in Table 5-2. Both publications implemented the notation symmetric and asymmetric NH_2 stretching modes for the NH_2 groups. For the three highest vibrational NH stretching frequencies, both calculations gave reasonable results corresponding well to the bands at 3303 and 3491 cm^{-1} (Figure 5-1), allowing for solvent induced frequency shifts of about 30-40 cm^{-1}. On the other hand, the band at 3145 cm^{-1} falls in between the values predicted by Nir and Wang. It should be noted that the peak at 3380 cm^{-1} suggested by the 2D spectra is supposed to be the overtone or combination tone of fingerprint modes because of the much smaller diagonal anharmonicity of the order of 50 cm^{-1} compared to the 130 cm^{-1} of NH stretching mode of free NHs.

Table 5-2: Comparison of Vibrational Mode Assignment for the GC Base Pair (a: DFT at the level of B3LUP/6-311++G, no scaling. b: DFT Hartree-Fock calculations with 6-31G(d,p) basis set, and scaling factor 0.893)**

Vibrational modes	Anharmonic frequencies from DFT[a] (cm^{-1})	Anharmonic frequencies from DFT[b] (cm^{-1})	Experimental absorption maximum (cm^{-1})
$\nu_C(NH_2)_s$	2905.3	3243	3145
$\nu_G(NH)$	3055.3	3264	
$\nu_G(NH_2)_s$	3347.9	3343	3303
$\nu_C(NH_2)_a$	3515.0	3526	3491
$\nu_G(NH_2)_a$	3522.9	3538	

We first focus on G and C monomers, for the well-defined structure of them suggests a certain picture of describing the vibration modes. C contains one NH_2 group only, while in G there are one NH_2 group and one free NH bond. The free NH_2 group adopts a delocalized picture where the two NH units couple with each other and can be described as the symmetric and asymmetric stretch vibrations, which are linear "+" and "–" combination of two individual local NH oscillators. In the experimental data, the symmetric and asymmetric stretching vibrations can be easily assigned to the pronounced peaks at 3418 and 3534 cm^{-1} for C, and at 3411 and 3521 cm^{-1} for G, which are only slightly downshifted from the gas phase experiment results of cytosine (3451.7 and 3572.7 cm^{-1} for $\nu(NH_2)_a$ and $\nu(NH_2)_a$ respectively [145]) and guanine (3444.5 and 3544.5 cm^{-1} for $\nu(NH_2)_a$ and $\nu(NH_2)_a$ respectively [146, 175]) because of the effect of the solvent. From this we can extract that the decoupled frequencies of NH unit in NH_2 group are located at 3476 cm^{-1} and 3466 cm^{-1} in C and G respectively, with

mechanical couplings |V| of 58 cm^{-1} and 55 cm^{-1}. Upon the formation of the GC base pairs, the hydrogen bonds shift the vibrational NH stretching modes to lower frequency. Thus, the downshifted peaks at 3145 cm^{-1} and 3303 cm^{-1}, compared to more than 3400 cm^{-1} in the monomer, are attributed to the hydrogen-bonded NH units. Based on the structure of the GC base pair suggested by the DFT calculations, dipole-dipole coupling or columbic interaction are much smaller than the NH_2 mechanical coupling of 58 cm^{-1} or 55 cm^{-1}. As the downshift is more than 100 cm^{-1}, it is scarcely due to the coupling between NH stretching modes but the diagonal frequency shifts. With more than 2 times more shift than the coupling, a simple calculation shows that the NH stretches are more than 90% localized. The narrow peak at 3491 cm^{-1} confirms the approaching of free NH stretching modes to the decoupled frequencies of NH units in NH_2 group at 3476 cm^{-1} and 3466 cm^{-1}. The asymmetric absorption lineshape may hint at the overlap of two decoupled NH stretching mode absorption bands from the NH_2 group of C and G respectively. Therefore, we adopt a localized picture of NH_2 group in GC dimers with a hydrogen-bonded NH (denoted as $\upsilon_G(NH_2)_b$ and $\upsilon_C(NH_2)_b$ respectively) and unbound NH stretching (denoted as $\upsilon_G(NH_2)_f$ and $\upsilon_C(NH_2)_f$ respectively), instead of symmetric and asymmetric combination. Meanwhile, the secondary amino NH stretching band of G, which is hydrogen-bonded to C, is denoted as $\upsilon_G(NH)$.

As we have noticed all the three absorption bands appear asymmetric, for which the half-width at half-maximum (HWHM) is a reliable indicator. For the peak at 3491 cm^{-1}, the HWHM of low frequency side is more than two times that of the high frequency side when Gaussian fits are applied. In the meantime, for peak 3145 cm^{-1}, the low frequency side is 80% broader than the high frequency side. It is difficult and unreliable to fit the peak 3303 cm^{-1} in the same way because the extending tail of peak 3145 cm^{-1} is not negligible, as well as the existence of the second peak at 3380 cm^{-1} suggested by 2D spectra. However, the asymmetric lineshape of the peak 3145 cm^{-1} gives no unambiguous information about the component of the absorption bands except the peak 3491 cm^{-1}, where the two unbound NH stretching modes are obviously located. As it is not uncommon for a symmetric distribution around an equilibrium structure to result in an asymmetric distribution in interactions [176], they may reflect a small variation in GC base pair hydrogen bond geometry around equilibrium structure, or hint at one band consisting of two bands in different bandwidth.

Iogansen[177] has investigated the relationship between the formation enthalpy of hydrogen bonds and the intensity of the absorbance of the stretching mode of the general hydrogen bonded systems XH. He derived an empirical relationship given by

$$-\Delta H = 12.2\Delta\left(A^{\frac{1}{2}}\right) \quad (5.1)$$

where ΔH is the enthalpy change upon hydrogen bonding in kJ/mol and $A^{1/2}$ is the square root of the integration over whole vibrational band and corresponds to the change of the transition dipole moment of the hydrogen bonded stretching oscillator. Although this equation cannot be understood with a theoretical model or explanation, it is widely proven to be accurate in different systems. However, he claimed that a general relation between absorption change and the frequency shift does not exist.

Spencer and coworkers studied hydrogen bonded NH systems, where the absorption change and the frequency shift were investigated[178]. After correcting for the heat of solution, a linear correlation between hydrogen bond enthalpies and frequencies shift due to the hydrogen bonds was discovered for N-H⋯O=C and N-H⋯N as following,

N-H…N system: $-\Delta H = (0.0107 \pm 0.0005)\Delta\upsilon + (1.33 \pm 0.14)$ (5.2)

N-H…O=C system: $-\Delta H = (0.0133 \pm 0.0011)\Delta\upsilon + (1.87 \pm 0.16)$ (5.3)

Where ΔH is the enthalpy change upon hydrogen bonding in kcal/mol and $\Delta\upsilon$ is the frequency shift due to the formation of hydrogen bond in cm^{-1}.

Combining the results of Iogansen and Spence, we can obtain the relation between frequency shift and the ratio of hydrogen bonded NH stretching strength over free NH oscillator strength $R(\Delta\upsilon)$.

N-H…N system: $R(\Delta\upsilon) = (1 + \Delta\upsilon/272.5)^2$ (5.4)

N-H⋯O=C system: $R(\Delta\upsilon) = (1 + \Delta\upsilon/219.2)^2$ (5.5)

with $\Delta\upsilon$ in cm^{-1}.

As we have assigned the unbound NH of NH_2 group of G and C ($\upsilon_G(NH_2)_f$ and $\upsilon_C(NH_2)_f$) to the narrow peak at 3491 cm^{-1}, the red shift of the hydrogen bonded NH stretching oscillators are 188 cm^{-1} and 346 cm^{-1}. Applying these shifts to the equations (5.4) and (5.5), the resulting intensity enhancement will be 2.86/3.45 and 5.15/6.65 for N-H⋯N/N-H⋯O=C system. The DFT calculation has indicated that the C(N-H)⋯G(O=C) is significantly stronger than G(N-H)⋯C(O=C). We can therefore allocate the C(N-H)⋯G(O=C) to the most red shifted band at

3145 cm^{-1} and G(N-H)···C(O=C) to the less shifted band at 3303 cm^{-1}. Consequently, when we assume that the absorption of the two unbound NH oscillator are equal, which is in line with the fact that they are very similar in diagonal frequency, the integrated intensity of the three bands should be 2:3.45:6.65 from high to low frequency. The actual integration of them turns out to be 2:3.2:13.5, when integrating over the following regions: 3431-3600 cm^{-1}, 3255-3350 cm^{-1}, and 3050-3255 cm^{-1}. By comparing the two ratios, it is clear that the N-H···N goes likely to lower band 3145 cm^{-1} to form the final ratio 2:3.45:11.8 rather than 2:6.31:6.65 when it goes to middle band at 3303 cm^{-1}. The experimental data agree with the empirical equation in a reasonable degree. Therefore we can assign the peak 3491 cm^{-1} to the combination of two unbound NH oscillators of NH_2 group of G and C ($\upsilon_G(NH_2)_f$ and $\upsilon_C(NH_2)_f$), peak 3303 cm^{-1} to the hydrogen bonded NH oscillator of NH_2 group of G ($\upsilon_G(NH_2)_b$) and peak 3145 cm^{-1} to the overlapping of hydrogen bonded NH oscillator of G ($\upsilon_G(NH)$), and hydrogen bonded NH oscillator of NH_2 group of C ($\upsilon_C(NH_2)_b$).

The peak at 3380 cm^{-1} is assigned to the overtone of CO stretching mode in guanine, which is located at 1700 cm^{-1}. Thus the anharmonicity is ~20 cm^{-1}, agreeing with the 80 cm^{-1} difference between the 0→2 transition and the 2→4 transition.

5.5 Dynamics of NH Stretching Modes

When a molecular is excited, it will lose its equilibrium and starts to respond to the non-equilibrium by redistributing the excess energy and returning to the ground state. There are usually two ways of redistribution, one is to the other modes of the molecule (intramolecular vibration energy redistribution, IVR), the other one is the surrounding solvent molecules (vibrational energy relaxation, VER). Normally, the IVR occurs previous to the VER, therefore VER is mainly reflected in the cooling process where the vibration is said to decay from the hot ground state to refill the thermal equilibrium ground state.

When the hydrogen bond is formed, additional low frequency modes will provide more ways for the excess energy to be redistributed [179], or/and the anharmonic coupling can be enhanced with combination/overtone levels of fingerprint vibrations by reducing the energy mismatch [137, 180]. These appear to dramatically shorten the lifetime of NH/OH stretching vibrations from picoseconds scale when they are free to a few hundred femtoseconds when they become hydrogen-bonded.

This shortening is also observed in our experiments (cf. Figure 5-5), as the peak at 3491 cm^{-1}, assigned to a combination of the free NH stretching vibrations $\upsilon_G(NH_2)_f$ and $\upsilon_C(NH_2)_f$, has a lifetime of ~2.4 ps. The asymmetric lineshape of the peak 3491 cm^{-1} suggests that the two free NH stretching vibrations $\upsilon_G(NH_2)_f$ and $\upsilon_C(NH_2)_f$ absorb at different frequencies. A possible lifetime difference cannot be effectively resolved in the current situation, because of the overlap of two oscillators as well as their overlap with potential existing hot ground states during the recovery which absorb at slightly different frequencies. For the bound $\upsilon_C(NH_2)_b$, and $\upsilon_G(NH)$ stretching vibrations, located at 3145 cm^{-1}, the ~0.3 ps component, in the bleach recovery suggests a pronounced vibrational lifetime shortening. The few picosecond component corresponds to the cooling dynamics. The lifetime of $\upsilon_G(NH_2)_b$ stretching vibration, located at 3303 cm^{-1}, is also shortened to ~0.2 ps, with a pronounced slow dynamics observed pointing to a slow refilling of the ground state. For the overtone of CO stretching mode, the excitation decays all the way to 0 with a time constant 0.3 ps. This makes the flat center line disappear very quickly in the first 50 fs, and then reemerge from 0.4 ps onwards.

We conclude that the lifetimes of free NH stretch oscillators are a few picoseconds, whereas the hydrogen-bonded NH stretch oscillators are governed by the population decay on a subpicosecond time scale. Exponential fitting of the decay of the peak at 3491 cm^{-1} results in a 2.4 ps average decay time for the non-hydrogen-bonded NH oscillators $\upsilon_G(NH_2)_f$ and $\upsilon_C(NH_2)_f$. The decay time of the hydrogen-bonded NH oscillator of the NH_2 group of G, $\upsilon_G(NH_2)_b$ at 3303 cm^{-1}, is 0.2 ps according to the 2D-IR measurement, and could not be extracted from the pump-probe data. The hydrogen-bonded NH of G and hydrogen-bonded NH oscillator of NH_2 group of C $\upsilon_G(NH_2)_b$ and $\upsilon_G(NH)$, located at 3145 cm^{-1}, decays with a 0.3 ps time constant. As the peak at 3145 cm^{-1} was assigned to the combination of two stretching modes in last section, the lifetime 0.3 ps may be a weighted average value for the population relaxation of these two.

The cross peaks represent the coupling between different excitations. This coupling may be either anharmonic coupling or population transfer, as has been discussed in section 2.5.5. The different mechanisms result in different temporal behaviors and lineshapes. For a cross peak exclusively depending on the anharmonic coupling, it should have identical temporal behavior as the excited oscillator as the signal exists only when it is excited. The distance between the negative and positive components is usually small because the off-diagonal anharmonicity is usually of the order of 10 cm^{-1}. For a cross peak originating from the population transfer, the

temporal behavior will be determined by both donating and accepting oscillators as the signal comes from the excitation of the acceptor which is the consequence of the deactivation of the donor. The distance between the negative and positive components is much larger in our system, because it is decided by the diagonal anharmonicity of the acceptor which is more than 100 cm^{-1} for the hydrogen-bonded NH stretching mode. However, the lineshape difference is very often unclear in our 2D spectra, because of the strong overlap of many different peaks. For the off-diagonal peak (3303, 3145), the donor is the band 3303 cm^{-1} and the acceptor is the band 3145 cm^{-1}, and the band 3491 and 3145 cm^{-1} for the off-diagonal peak (3491, 3145).

The comparison of the temporal characteristics of the (3303, 3145) and (3303, 3303) peaks reveals that the signal intensity of the cross peak is not solely contributed by the instantaneous anharmonic coupling between the hydrogen-bonded NH stretching modes. The ratio of the magnitude, shown in Figure 5-6, exhibits a pronounced rise with the increasing population time T and gives evidence of vibrational population transfer from the $\upsilon_G(NH_2)_b$ mode at 3303 cm^{-1} to the $\upsilon_C(NH_2)_b$ and/or $\upsilon_G(NH)$ at 3145 cm^{-1}. As a result, the measured decay rate (1/0.24) ps^{-1} of the mode $\upsilon_G(NH_2)_b$ at 3303 cm^{-1} is the sum of the population transfer rate and the relaxation rate back to the $\upsilon = 0$ state. As Figure 5-6 shows, the ratio of the intensity of (3303, 3145)/(3303, 3303) rises on a time scale of 1 ps. This time evolution is determined by the relaxation of the oscillators at 3303 cm^{-1} and 3146 cm^{-1} and the population transfer between them. An exact transfer rate is hard to be extracted, because it would require independent information on the lifetime of the peak (3145, 3303), which is hard to acquire because of the spectral overlap of different $\upsilon = 0 \rightarrow 1$ and $\upsilon = 1 \rightarrow 2$ transitions, and also on the detailed relaxation of the two stretching modes at 3145 cm^{-1} which is not feasible in this situation. Thus, we can only derive a lower limit of the transfer time of 0.24 ps, by assuming that the energy transfer dominates the decay of the diagonal peak at 3303 cm^{-1}, and an upper limit of approximately 1.3 ps, which would be about 3 times longer than the decay time of peak 3145 cm^{-1}. A corresponding vibrational coupling V is estimated to be $|V| \approx 2.3 - 12$ cm^{-1}, again much smaller than the coupling of the NH oscillators of the NH_2 group.

However, the rise of the intensity ratio of the (3491, 3170) or (3491, 3303) peaks over the (3491, 3491) peak does not necessarily indicate energy transfer from the upper oscillators at 3491 cm^{-1} to the lower oscillator at 3145 and 3303 cm^{-1}. In part, this is because there are two oscillators located at 3491 cm^{-1} and the ratio cannot be regarded as the comparison between an off-diagonal peak and a single diagonal one. Nevertheless these cross peaks indicate a

coupling between the oscillator at 3491 cm^{-1} and those at 3145 or 3303 cm^{-1}, whereas an energy transfer, if existing, should be very slow. Thus the distances between the positive and negative components are dictated by the off-diagonal anharmonicity, which is of the order of 10 cm^{-1}. Note that the maximum of the off-diagonal peak (3491, 3145) is located at ν_3=3170 instead of 3145 cm^{-1}. The increase of the frequency may result from cancellation effects due to overlap with the spectrally broad negative cross peak. The blue shift of the detection frequency is less for the peak (3491, 3303) due to the narrower lineshape of the lower oscillator, and overlap with the negative peak on the high frequency side. These overlaps also make it difficult to accurately estimate the splitting distances between the positive and negative components, which can help to tell the off-diagonal anharmonicity of the coupling. What we can conclude is that the off-diagonal anharmonicities are much smaller than the diagonal anharmonicity. In the meantime, the lack of efficient energy transfer suggests that the coupling strengths for the two mode pairs are very small too.

If we assume a vibrational excitation transfer mechanism reminiscent of Förster dipole-dipole coupling with an r^{-6} dependence on the dipole separation r for the population transfer rate, likely candidates involved in the energy transfers can be derived according to the structure of the GC dimer. For the energy transfer from 3303 to 3145 cm^{-1}, while the upper oscillator is $\upsilon_G(NH_2)_b$, the lower oscillator is likely the $\upsilon_G(NH)$ mode as it is closer than $\upsilon_C(NH_2)_b$. For the coupling between the modes at 3491 and 3170 cm^{-1}, where the upper transition can be associated with either one of the two free NH stretching modes $\upsilon_G(NH_2)_f$ and $\upsilon_C(NH_2)_f$, the corresponding lower oscillator is likely the $\upsilon_C(NH_2)_b$, as the $\upsilon_G(NH)$ is far from both free NH units. Thus, the upper oscillator involved in the coupling is likely the $\upsilon_C(NH_2)_f$. Based on the same deduction, the modes contributing to the coupling between 3491 and 3303 cm^{-1} are $\upsilon_G(NH_2)_f$ and $\upsilon_G(NH_2)_b$. The small coupling strength between the two NH units in the same NH_2 group supports the picture that the NH stretching modes of the NH_2 group become significantly localized upon the formation of hydrogen bond.

5.6 Conclusions

In this chapter, the vibrational dynamics in the electronic ground state of guanosine-cytidine dimers in $CHCl_3$ were studied with ultrafast 2D IR spectroscopy and linear spectroscopy.

According to concentration dependent infrared spectra, the guanosine and the cytidine in chloroform solution prefer to form dimers with WC structure. Upon the formation of three hydrogen bonds between G and C, the involved NH stretching modes are red shifted and broadened, leading to a congested spectrum. Comparison of the linear spectrum of the GC solution with those of the G or C solution shows that the GC base pairs in the solution have only IR-active transitions of NH stretching vibrations above 3000 cm^{-1}, in contradiction to quantum calculations based on density functional theory by Wang et al.

For the monomers of G and C, the vibrational couplings between the NH stretching oscillators in the NH_2 groups are about 55 and 58 cm^{-1}, which justifies descriptions in terms of symmetric and asymmetric stretching modes. In contrast, when the GC base pairs are formed, the hydrogen bonds between bases induce frequency downshifts of the participating NH stretching modes of about 163 cm^{-1} (for the NH_2 group in G) and 332 cm^{-1} (for the NH_2 group in C), which are much bigger than the coupling of the two NH stretching modes within the NH_2 groups. Thus, a description based on a localized mode basis for the N-H stretching vibrations is more appropriate for the GC base pairs in chloroform solution. The assignment of different bands was supported by arguments based on empirical relations between the red shift and transition strength of hydrogen bonded NH stretching modes. In contrast, the bond length is different in helix structure because of the interaction of the backbones.

Based on the assignment and description of the GC base pairs, we analyzed the ultrafast spectroscopic experimental results. Due to its long measured time range, the pump-probe experiment gave a more accurate value of the population decay of free NH modes in the NH_2 groups of around 2.9 ps, whereas extensive spectral overlap of bleaches and increased absorptions prevents an accurate determination of the population kinetics between 3280 and 3450 cm^{-1}. Ultrafast 2D IR experiments gave more insight into the energy transfer and vibrational coupling within the GC base pair by better resolving the frequencies of excitations. The different broadening mechanisms separate the CO stretching overtone, which is inhomogeneous, from $\upsilon_G(NH_2)_b$, which is mostly homogeneously broadened. The lifetime is around 0.3 ps for the overtone of CO stretching, and 0.2 ps for $\upsilon_G(NH_2)_b$. Compared to the free NH stretching modes, the lifetime of hydrogen-bonded NH stretching modes are greatly shortened. The lifetimes of the oscillators $\upsilon_G(NH)$ and $\upsilon_C(NH_2)_b$, that make up the 3145 cm^{-1} absorption band, are about 0.3 ps, again much shorter than those of the free NH stretching modes $\upsilon_G(NH_2)_f$ and $\upsilon_C(NH_2)_f$. The shortening of the vibrational lifetime upon the formation of hydrogen bonds is ascribed to the reduction of the energy mismatch from the overtone or

combination tone of finger print modes. Energy transfer between NH stretching oscillators is also observed. The time constant of the energy transfer from $\upsilon_G(NH_2)_b$ to $\upsilon_G(NH)$ is of the order of 0.5 ps, corresponding to a coupling strength of about 5 cm^{-1}. Between the free and hydrogen-bonded NH stretching modes of the two NH_2 groups, off-diagonal peaks are also observed that indicate the existence of coupling between them. However, a proof of energy transfer between them is lacking. Thus, the energy transfer, if existing, is very inefficient. This is in agreement with the long life time of the free NH stretching modes. The small coupling strength corresponding to the slow energy transfer corroborates the local mode picture we employed to depict the NH_2 group.

6. Summary

Among various interactions between atoms, hydrogen bonds are moderate in terms of strength, but have extreme importance. In defining structures and dynamical behavior of molecular systems, hydrogen bonds play a vital role due to their moderate strength and flexibility. The hydrogen bonds define structures of base pairs and affect pathways of energy exchange. Thus, in order to study non-equilibrium processes, such as the dissipation of the excess energy originating from the decay of electronic excitation which could be potentially damaging, the information of hydrogen bonds are eagerly needed. In this thesis, ultrafast IR spectroscopy is employed to pursue a deeper understanding of the intra- and inter-molecules interactions introduced by the formation of hydrogen bonds, i.e., interactions in DNA base pairs, and between base pairs and water molecules.

The interactions between the DNA double helix and the surrounding water shell were studied by investigating a short oligomer (a 23-mer) containing only alternating adenine-thymine base pairs. The sugar group and phosphate groups in the backbone are involved, and all interactions are considered. In order to understand the interactions between the DNA double helix and the surrounding water shell, we perfomed a series of humidity-dependent experiments.

When the relative humidity is 0%, there are only few water molecules surrounding the double helix. With our 2D spectroscopy results, we are able to dissect the spectral overlapping NH stretching modes with a delocalized model. We found that the NH_2 group of adenine is rather sensitive to its environment. As a result the symmetric and asymmetric NH_2 stretching modes present a peak shape characteristic of inhomogeneous broadening. The hydrogen-bonded NH of thymine, in contrast, is shielded in the base pair and less sensitive to the environment. An energy transfer was observed from the asymmetric NH_2 stretching mode of adenine to the NH stretching mode of thymine, with a coupling strength of the order of 5 cm^{-1}. As the few water molecules are located close to the phosphate group and form strong hydrogen bonds with the backbones, they are undergoing negligible spectral diffusion.

By increasing the relative humidity to 33 and 92%, the number of water molecules surrounding the double helix was raised to 6 and 20, respectively. Upon the increased hydration, no pronounced change of the NH stretching modes was observed. This indicates that the extra water molecules have a limited influence on the NH stretching oscillators,

suggesting that the NH stretching excitations are essentially localized to the particular base pair that undergoes minor geometry changes upon hydration. This behavior is in line with the relatively slow structural dynamics of water molecules in the first hydration layer around the thymine NH and adenine NH_2 groups. Thus, fluctuating forces originating from the DNA oligomers and their counterions are considered the main mechanism of the subpicosecond NH stretch dephasing.

The extra water molecules brought with the increased relative humidity start to build a second hydration shell after having finished the first one. Unlike the strong hydrogen bonds between the first hydration shell and the DNA molecule existing in the 0% relative humidity sample, the hydrogen bonds in the second hydration shell are weaker and more flexible. As a result, we now observed a spectral diffusion on a picosecond time scale indicated by the drop of the slope of the peak center lines. Compared to bulk water, the drop of the slope of the center lines is not as dramatic within the first 100 fs, and the remaining value is about five times higher after 500 fs. The slowing down of the drop is due to the small network in the DNA/water system, that reduces the rate of resonant energy transfer. Moreover, the hydrogen bonds with the DNA molecules suppress local perturbations such as rotational and translational motion of water molecules. The observed slowing down of the spectral diffusion compared to bulk water agrees with the MD calculation of DNA hydration, but the experiments do not support a slowing down by orders of magnitude in time.

When the vibrationally excited OH stretches in water relax, the excess energy is mostly efficiently redistributed into the local environment or its own low frequency mode, resulting in hot ground states. Such hot ground states cause a blue shift of the fundamental transitions, due to the increasing of distances between water molecules and weakening of hydrogen bonds. The building up of the hot ground state has a time constant of 200 fs, similar to bulk water. The fast formation of a hot ground state points to the fast randomization of excess energy, similar to the behavior in bulk water.

In order to understand the interaction inside the base pair, we studied the guanosine-cytidine base pair in chloroform, adopting the Watson-Crick geometry, with three hydrogen bonds between them. With no water surrounding the base pair, and weak interaction between the solute and solvent, we can focus on the interactions within the base pairs. The vibrational stretching modes of free NH_2 groups in G and C monomers are depicted by symmetric and asymmetric stretching modes, which are the “+” and “-” combinations of free NH stretching

modes. In contrast, the hydrogen bonds lower the Eigen-frequencies of the hydrogen-bonded NH stretching vibrations by ~150-350 cm^{-1}, which is much more than the coupling within the NH_2 group, and effectively decouples the free and hydrogen-bonded NH stretching modes. Thus, they become fairly localized free NH stretching modes and hydrogen-bonded NH stretching modes. Furthermore, we have observed energy transfer between the hydrogen-bonded NH stretching modes $\upsilon_G(NH_2)_b$ and $\upsilon_G(NH)$, and coupling between the free NH stretching mode $\upsilon_C(NH_2)_f$, $\upsilon_G(NH_2)_f$ and the corresponding hydrogen-bonded NH stretching mode $\upsilon_C(NH_2)_b$, $\upsilon_G(NH_2)_b$. The absence of efficient energy transfer between hydrogen-bonded and free NH stretching modes in the same NH_2 group indicates that both NH stretching modes are fairly localized. The lacking of an efficient path for energy redistribution is corroborated by the long lifetime of free NH stretching oscillators.

These results have given rich information about the interactions within the base pair and with the hydration shells. However, in order to understand native DNA, AT base pairs in solution and GC oligomers should be studied as well. Meanwhile, to observe directly the energy redistribution to fingerprint modes, two-color pump probe or two-color 2D spectroscopy will be helpful. On the other hand, the 2D FTIR spectroscopy will be a powerful tool in more researches, such as the structural transitions of RNA, folding kinetics of protein, and drug-binding interactions.

Bibliography

1. Pauling, L., *The shared-electron chemical bond.* Proceedings of the National Academy of Sciences of the United States of America, 1928. 14: p. 359.

2. Schuster, P., G. Zundel, and C. Sandorfy, *The hydrogen bond: Recent developments in theory and experiments*. The Hydrogen Bond: Recent developments in theory and experiments, ed. P. Schuster, G. Zundel, and C. Sandorfy. Vol. I-III. 1976, Amsterdam, the Netherlands: North Holland.

3. Pauling, L., *The Structure and Entropy of Ice and of Other Crystals with Some Randomness of Atomic Arrangement.* Journal of the American Chemical Society, 1935. 57(12): p. 2680-2684.

4. Watson, J.D. and F.H.C. Crick, *Molecular Structure of Nucleic Acids: A Structure for Deoxyribose Nucleic Acid.* Nature, 1953. 171(4356): p. 737-738.

5. Taylor, J.H., P.S. Woods, and W.L. Hughes, *THE ORGANIZATION AND DUPLICATION OF CHROMOSOMES AS REVEALED BY AUTORADIOGRAPHIC STUDIES USING TRITIUM-LABELED THYMIDINE.* Proceedings of the National Academy of Sciences of the United States of America, 1957. 43(1): p. 122-128.

6. Eisenberg, D. and W. Kauzmann, *The structure and properties of water*. 1969, Oxford: Oxford University Press.

7. Franks, F., ed. *Water, a comprehensive treatise*. 1972, Plenum: New York.

8. Dennison, D.M., *The Crystal Structure of Ice.* Physical Review, 1921. 17(1): p. 20-22.

9. Jorgensen, W.L. and J.D. Madura, *Temperature and size dependence for Monte Carlo simulations of TIP4P water.* Molecular Physics, 1985. 56(6): p. 1381-1392.

10. Franklin, R.E. and R.G. Gosling, *Evidence for 2-Chain Helix in Crystalline Structure of Sodium Deoxyribonucleate.* Nature, 1953. 172(4369): p. 156-157.

11. Drew, H.R. and R.E. Dickerson, *Structure of a B-DNA dodecamer , : III. Geometry of hydration.* Journal of Molecular Biology, 1981. 151(3): p. 535-556.

12. Umrania, Y., H. Nikjoo, and J.M. Goodfellow, *A KNOWLEDGE-BASED MODEL OF DNA HYDRATION.* International Journal of Radiation Biology, 1995. 67(2): p. 145-152.

13. Libowitzky, E., *Correlation of O-H stretching frequencies and O-H···O hydrogen bond lengths in minerals.* Monatshefte für Chemie, 1999. 130(8): p. 1047-1059.

14. Novak, A., *Hydrogen bonding in solids. Correlation of spectroscopic and crystallographic data.* Structure and Bonding (Berlin), 1974. 18: p. 177-216.

15. Mikenda, W., *Stretching frequency versus bond distance correlation of O---D(H)···Y (Y= N, O, S, Se, Cl, Br, I) hydrogen bonds in solid hydrates.* Journal of Molecular Structure, 1986. 147(1-2): p. 1-15.

16. Mikenda, W. and S. Steinböck, *Stretching frequency vs. bond distance correlation of hydrogen bonds in solid hydrates: a generalized correlation function.* Journal of Molecular Structure, 1996. 384(2-3): p. 159-163.

17. Rey, R., K.B. Møller, and J.T. Hynes, *Hydrogen bond dynamics in water and ultrafast infrared spectroscopy.* Journal of Physical Chemistry A, 2002. 106(50): p. 11993-11996.

18. Mukamel, S., *Principles of nonlinear optical spectroscopy*. Oxford Series in Optical and Imaging Sciences, ed. M. Lapp, et al. Vol. 6. 1995, Oxford: Oxford University Press. 543.

19. Shen, Y.R., *Optical Second Harmonic Generation at Interfaces.* Annual Review of Physical Chemistry, 1989. 40(1): p. 327-350.

20. Shen, Y.R., *Surface Second Harmonic Generation: A New Technique for Surface Studies.* Annual Review of Materials Science, 1986. 16(1): p. 69-86.

21. Kubo, R., *A stochastic theory of line shape.* Advances in Chemical Physics, 1969. 15: p. 101-126.

22. Schmidt, J.R., N. Sundlass, and J.L. Skinner, *Line shapes and photon echoes within a generalized Kubo model.* Chemical Physics Letters, 2003. 378(5-6): p. 559-566.

23. Yan, Y.J. and S. Mukamel, *Electronic dephasing, vibrational relaxation, and solvent friction in molecular nonlinear optical line shapes*. Vol. 89. 1988: AIP. 5160-5176.

24. Mukamel, S., *Multidimensional femtosecond correlation spectroscopies of electronic and vibrational excitations.* Annual Review of Physical Chemistry, 2000. 51: p. 691-729.

25. Stenger, J., et al., *Ultrafast vibrational dephasing of liquid water.* Physical Review Letters, 2001. 87(2): p. 027401.

26. Scheurer, C., A. Piryatinski, and S. Mukamel, *Signatures of beta-peptide unfolding in two-dimensional vibrational echo spectroscopy: A simulation study.* Journal of the American Chemical Society, 2001. 123(13): p. 3114 -3124.

27. Joo, T., et al., *Third-order nonlinear time domain probes of solvation dynamics.* Journal of Chemical Physics, 1996. 104(16): p. 6089-6108.

28. de Boeij, W.P., M.S. Pshenichnikov, and D.A. Wiersma, *On the relation between the echo-peak shift and Brownian-oscillator correlation function.* Chemical Physics Letters, 1996. 253(1-2): p. 53-60.

29. Oh, M.H.J., et al., *Three-Pulse Photon-Echo Peak Shift Spectroscopy and Its Application for the Study of Solvation and Nanoscale Excitons.* ChemPhysChem. 12(1): p. 88-100.

30. Chachisvilis, M., H. Fidder, and V. Sundstr 鯧, *Electronic coherence in pseudo two-colour pump-probe spectroscopy.* Chemical Physics Letters, 1995. 234(1-3): p. 141-150.

31. Dwyer, J.R., et al., *Ultrafast Vibrational Dynamics of Adenine-Thymine Base Pairs in DNA Oligomers.* The Journal of Physical Chemistry B, 2008. 112(36): p. 11194-11197.

32. Szyc, Ł., et al., *Ultrafast dynamics of N-H and O-H stretching excitations in hydrated DNA oligomers.* Chemical Physics, 2009. 357(1-3): p. 36-44.

33. Cho, M., *Two-Dimensional Optical Spectroscopy*. 2009, Boca Raton: CRC Press.

34. Hamm, P., M. Lim, and R.M. Hochstrasser, *Structure of the amide I band of peptides measured by femtosecond nonlinear-infrared spectroscopy.* Journal of Physical Chemistry B, 1998. 102(31): p. 6123-6138.

35. DeCamp, M.F., et al., *Single-shot two-dimensional infrared spectroscopy.* Opt. Express, 2007. 15(1): p. 233-241.

36. DeCamp, M.F. and A. Tokmakoff, *Single-shot two-dimensional spectrometer.* Opt. Lett., 2006. 31(1): p. 113-115.

37. Cervetto, V., et al., *Double-resonance versus pulsed Fourier transform two-dimensional infrared spectroscopy: An experimental and theoretical comparison.* The Journal of Chemical Physics, 2004. 121(12): p. 5935-5942.

38. Aue, W.P., E. Bartholdi, and R.R. Ernst, *2-dimensional spectroscopy - Application to nuclear magnetic resonance.* Journal of Chemical Physics, 1976. 64(5): p. 2229-2246.

39. Ge, N.-H., M.T. Zanni, and R.M. Hochstrasser, *Effects of vibrational frequency correlations on two-dimensional infrared spectra.* Journal of Physical Chemistry A, 2002. 106(6): p. 962-972.

40. Gnanakaran, S. and R.M. Hochstrasser, *Conformational preferences and vibrational frequency distributions of short peptides in relation to multidimensional infrared spectroscopy.* Journal of the American Chemical Society, 2001. 123(51): p. 12886 - 12898.

41. Hamm, P. and R.M. Hochstrasser, *Structure and dynamics of proteins and peptides: Femtosecond two-dimensional infrared spectroscopy*, in *Ultrafast infrared and Raman spectroscopy [Practical Spectroscopy Series Vol. 26]*, M.D. Fayer, Editor. 2001, Marcel Dekker, Inc.: New York. p. 273-347.

42. Zanni, M.T., M.C. Asplund, and R.M. Hochstrasser, *Two-dimensional heterodyned and stimulated infrared photon echoes of N-methylacetamide-D.* Journal of Chemical Physics, 2001. 114(10): p. 4579-90.

43. Zanni, M.T., et al., *Two-dimensional IR spectroscopy can be designed to eliminate the diagonal peaks and expose only the crosspeaks needed for structure determination.*

Proceedings of the National Academy of Sciences of the United States of America, 2001. 98(20): p. 11265-11270.

44. Khalil, M., N. Demirdöven, and A. Tokmakoff, *Obtaining absorptive line shapes in two-dimensional infrared vibrational correlation spectra.* Physical Review Letters, 2003. 90(4): p. 047401.

45. Khalil, M., N. Demirdöven, and A. Tokmakoff, *Coherent 2D IR spectroscopy: Molecular structure and dynamics in solution.* Journal of Physical Chemistry A, 2003. 107(27): p. 5258-5279.

46. Lazonder, K., M.S. Pshenichnikov, and D.A. Wiersma, *Easy interpretation of optical two-dimensional correlation spectra.* Opt. Lett., 2006. 31(22): p. 3354-3356.

47. Kraemer, D., et al., *Temperature dependence of the two-dimensional infrared spectrum of liquid H2O.* Proceedings of the National Academy of Sciences, 2008. 105(2): p. 437-442.

48. Kwak, K., et al., *Frequency-frequency correlation functions and apodization in two-dimensional infrared vibrational echo spectroscopy: A new approach.* The Journal of Chemical Physics, 2007. 127: p. 124503.

49. Kwak, K., D.E. Rosenfeld, and M.D. Fayer, *Taking apart the two-dimensional infrared vibrational echo spectra: More information and elimination of distortions.* The Journal of Chemical Physics, 2008. 128: p. 204505.

50. Fenn, E.E., et al., *Dynamics of Water at the Interface in Reverse Micelles: Measurements of Spectral Diffusion with Two-Dimensional Infrared Vibrational Echoes.* The Journal of Physical Chemistry B, 2011. 115(40): p. 11658-11670.

51. Hamm, P. and M. Zanni, *Concepts and Methods of 2D Infrared Spectroscopy*. 2011, Cambridge: Cambridge University Press.

52. Maiman, T.H., *STIMULATED OPTICAL RADIATION IN RUBY.* Nature, 1960. 187(4736): p. 493-494.

53. Collins, R.J., et al., *Coherence, Narrowing, Directionality, and Relaxation Oscillations in the Light Emission from Ruby.* Physical Review Letters, 1960. 5(7): p. 303-305.

54. Mourou, G. and T. Tajima, *More Intense, Shorter Pulses.* Science, 2011. 331(6013): p. 41-42.

55. Fork, R.L., B.I. Greene, and C.V. Shank, *Generation of optical pulses shorter than 0.1 psec by colliding pulse mode locking.* Applied Physics Letters, 1981. 38(9): p. 671-672.

56. Strickland, D. and G. Mourou, *Compression of amplified chirped optical pulses.* Optics Communications, 1985. 56(3): p. 219-221.

57. Kaindl, R.A., et al., *Generation, shaping, and characterization of intense femtosecond pulses tunable from 3 to 20 mu m.* Journal of the Optical Society of America B, 2000. 17(12): p. 2086-94.

58. Ventalon, C., et al., *Generation and complete characterization of intense mid-infrared ultrashort pulses.* J. Opt. Soc. Am. B, 2006. 23(2): p. 332-340.

59. Imahoko, T., et al., *Tunable mid-infrared, high-energy femtosecond laser source for glyco-protein structure analysis.* Applied Physics B: Lasers and Optics, 2007. 87(4): p. 629-634.

60. Chalus, O., et al., *Six-cycle mid-infrared source with 3.8 μJ at 100 kHz.* Opt. Lett., 2010. 35(19): p. 3204-3206.

61. Backus, S., et al., *0.2-TW laser system at 1kHz.* Opt. Lett., 1997. 22(16): p. 1256-1258.

62. Boyd., R.W., *Nonlinear Optics*. 1992, San Diego, U.S.A: Academic press. inc.

63. Midwinter, J.E. and J. Warner, *The effects of phase matching method and of uniaxial crystal symmetry on the polar distribution of second-order non-linear optical polarization.* British Journal of Applied Physics, 1965. 16(8): p. 1135.

64. Alfano, R.R. and S.L. Shapiro, *Observation of Self-Phase Modulation and Small-Scale Filaments in Crystals and Glasses.* Physical Review Letters, 1970. 24(11): p. 592.

65. Maier, M., W. Kaiser, and J.A. Giordmaine, *Intense Light Bursts in the Stimulated Raman Effect.* Physical Review Letters, 1966. 17(26): p. 1275.

66. Kane, D.J. and R. Trebino, *CHARACTERIZATION OF ARBITRARY FEMTOSECOND PULSES USING FREQUENCY-RESOLVED OPTICAL GATING.* Ieee Journal of Quantum Electronics, 1993. 29(2): p. 571-579.

67. Tian, P., et al., *Femtosecond Phase-Coherent Two-Dimensional Spectroscopy.* Science, 2003. 300(5625): p. 1553-1555.

68. Shim, S.-H. and M.T. Zanni, *How to turn your pump-probe instrument into a multidimensional spectrometer: 2D IR and Vis spectroscopies via pulse shaping.* Physical Chemistry Chemical Physics, 2009. 11(5): p. 748-761.

69. de Boeij, W.P., M.S. Pshenichnikov, and D.A. Wiersma, *ULTRAFAST SOLVATION DYNAMICS EXPLORED BY FEMTOSECOND PHOTON ECHO SPECTROSCOPIES.* Annual Review of Physical Chemistry, 1998. 49(1): p. 99-123.

70. Helbing, J. and P. Hamm, *Compact implementation of Fourier transform two-dimensional IR spectroscopy without phase ambiguity.* J. Opt. Soc. Am. B, 2011. 28(1): p. 171-178.

71. Asplund, M.C., M.T. Zanni, and R.M. Hochstrasser, *Two-dimensional infrared spectroscopy of peptides by phase-controlled femtosecond vibrational photon echoes.* Proceedings of the National Academy of Sciences, 2000. 97(15): p. 8219-8224.

72. Khalil, M., N. Demirdöven, and A. Tokmakoff, *Coherent 2D IR Spectroscopy: Molecular Structure and Dynamics in Solution.* The Journal of Physical Chemistry A, 2003. 107(27): p. 5258-5279.

73. Volkov, V., R. Schanz, and P. Hamm, *Active phase stabilization in Fourier-transform two-dimensional infrared spectroscopy.* Optics Letters, 2005. 30(15): p. 2010-2012.

74. Dorrer, C., et al., *Spectral resolution and sampling issues in Fourier-transform spectral interferometry.* J. Opt. Soc. Am. B, 2000. 17(10): p. 1795-1802.

75. Cowan, M.L., J.P. Ogilvie, and R.J.D. Miller, *Two-dimensional spectroscopy using diffractive optics based phased-locked photon echoes.* Chemical Physics Letters, 2004. 386(1-3): p. 184-189.

76. Lepetit, L., G. Chéiaux, and M. Joffre, *Linear techniques of phase measurement by femtosecond spectral interferometry for applications in spectroscopy.* J. Opt. Soc. Am. B, 1995. 12(12): p. 2467-2474.

77. Asbury, J.B., T. Steinel, and M.D. Fayer, *Vibrational echo correlation spectroscopy probes of hydrogen bond dynamics in water and methanol.* Journal of Luminescence, 2004. 107(1-4): p. 271-286.

78. Wang, A.H.J., et al., *Molecular structure of a left-handed double helical DNA fragment at atomic resolution.* Nature, 1979. 282(5740): p. 680-686.

79. Saenger, W., *Principles of Nucleic Acid Structure*. 1984, New York: Springer-Verlag.

80. Krummel A T, P. Mukherjee, and M.T. Zanni, *Inter and Intrastrand Vibrational Coupling in DNA Studied with Heterodyned 2D-IR Spectroscopy.* J. Phys. Chem., 2003. 107(35): p. 9165.

81. Falk, M., A.G. Poole, and C.G. Goymour, *Infrared study of the state of water in the hydration shell of DNA.* Canadian Journal of Chemistry, 1970. 48(10): p. 1536-1542.

82. Edelhoch, H., et al., *The Thermodynamic Basis of the Stability of Proteins, Nucleic Acids, and Membranes*, in *Advances in Protein Chemistry*. 1976, Academic Press. p. 183-250.

83. Nikjoo, H., D.E. Charlton, and D.T. Goodhead, *Monte Carlo track structure studies of energy deposition and calculation of initial DSB and RBE.* Advances in Space Research, 1994. 14(10): p. 161-180.

84. Nibbering, E.T.J. and T. Elsaesser, *Ultrafast vibrational dynamics of hydrogen bonds in the condensed phase.* Chemical Reviews, 2004. 104(4): p. 1887 -1914.

85. Laage, D. and J.T. Hynes, *A Molecular Jump Mechanism of Water Reorientation.* Science, 2006. 311(5762): p. 832-835.

86. Bakker, H.J. and J.L. Skinner, *Vibrational Spectroscopy as a Probe of Structure and Dynamics in Liquid Water.* Chemical Reviews, 2009. 110(3): p. 1498-1517.

87. Falk, M., K.A. Hartman, and R.C. Lord, *Hydration of Deoxyribonucleic Acid. I. a Gravimetric Study.* Journal of the American Chemical Society, 1962. 84(20): p. 3843-3846.

88. Falk, M., K.A. Hartman, and R.C. Lord, *Hydration of Deoxyribonucleic Acid. II. An Infrared Study.* Journal of the American Chemical Society, 1963. 85(4): p. 387-391.

89. Kopka, M.L., et al., *Ordered water structure around a B-DNA dodecamer : A quantitative study.* Journal of Molecular Biology, 1983. 163(1): p. 129-146.

90. Schneider, B., et al., *A SYSTEMATIC METHOD FOR STUDYING THE SPATIAL-DISTRIBUTION OF WATER-MOLECULES AROUND NUCLEIC-ACID BASES.* Biophysical Journal, 1993. 65(6): p. 2291-2303.

91. Schneider, B. and H.M. Berman, *Hydration of the DNA bases is local.* Biophysical Journal, 1995. 69(6): p. 2661-2669.

92. Schneider, B., K. Patel, and H.M. Berman, *Hydration of the Phosphate Group in Double-Helical DNA.* Biophysical journal, 1998. 75(5): p. 2422-2434.

93. Phan, A.T., J.-L. Leroy, and M. Guéron, *Determination of the residence time of water molecules hydrating B ' -DNA and B -DNA, by one-dimensional zero-enhancement nuclear overhauser effect spectroscopy.* Journal of Molecular Biology, 1999. 286(2): p. 505-519.

94. Halle, B. and V.P. Denisov, *Water and monovalent ions in the minor groove of B-DNA oligonucleotides as seen by NMR.* Biopolymers, 1998. 48(4): p. 210-233.

95. Liepinsh, E., G. Otting, and K. Wüthrich, *NMR observation of individual molecules of hydration water bound to DNA duplexes: direct evidence for a spine of hydration water present in aqueous solution.* Nucleic Acids Research, 1992. 20(24): p. 6549-6553.

96. Schreiner, L.J., et al., *NMR spin grouping and correlation exchange analysis. Application to low hydration NaDNA paracrystals.* Biophysical journal, 1991. 59(1): p. 221-234.

97. Sunnerhagen, M., et al., *Water molecules in DNA recognition I: hydration lifetimes of trp operator DNA in solution measured by NMR spectroscopy.* Journal of Molecular Biology, 1998. 282(4): p. 847-858.

98. Duan, Y., et al., *Molecular dynamics simulation study of DNA dodecamer d(CGCGAATTCGCG) in solution: conformation and hydration.* Journal of Molecular Biology, 1997. 272(4): p. 553-572.

99. Bonvin, A.M.J.J., et al., *Water molecules in DNA recognition II: a molecular dynamics view of the structure and hydration of the trp operator.* Journal of Molecular Biology, 1998. 282(4): p. 859-873.

100. Pal, S., P.K. Maiti, and B. Bagchi, *Exploring DNA groove water dynamics through hydrogen bond lifetime and orientational relaxation.* The Journal of Chemical Physics, 2006. 125(23): p. 234903-11.

101. Pal, S.K., L. Zhao, and A.H. Zewail, *Water at DNA surfaces: Ultrafast dynamics in minor groove recognition.* Proceedings of the National Academy of Sciences, 2003. 100(14): p. 8113-8118.

102. Andreatta, D., et al., *Power-Law Solvation Dynamics in DNA over Six Decades in Time.* Journal of the American Chemical Society, 2005. 127(20): p. 7270-7271.

103. Furse, K.E. and S.A. Corcelli, *Effects of an Unnatural Base Pair Replacement on the Structure and Dynamics of DNA and Neighboring Water and Ions.* The Journal of Physical Chemistry B, 2010. 114(30): p. 9934-9945.

104. Sen, S., et al., *Dynamics of Water and Ions Near DNA: Comparison of Simulation to Time-Resolved Stokes-Shift Experiments.* Journal of the American Chemical Society, 2009. 131(5): p. 1724-1735.

105. Nilsson, L. and B. Halle, *Molecular origin of time-dependent fluorescence shifts in proteins.* Proceedings of the National Academy of Sciences of the United States of America, 2005. 102(39): p. 13867-13872.

106. Li, T., et al., *Hydration Dynamics and Time Scales of Coupled Water-Protein Fluctuations.* Journal of the American Chemical Society, 2007. 129(11): p. 3376-3382.

107. Furse, K.E. and S.A. Corcelli, *The Dynamics of Water at DNA Interfaces: Computational Studies of Hoechst 33258 Bound to DNA.* Journal of the American Chemical Society, 2008. 130(39): p. 13103-13109.

108. Zhong, D., S.K. Pal, and A.H. Zewail, *Biological water: A critique.* Chemical Physics Letters, 2011. 503(1-3): p. 1-11.

109. Halle, B. and L. Nilsson, *Does the Dynamic Stokes Shift Report on Slow Protein Hydration Dynamics?* The Journal of Physical Chemistry B, 2009. 113(24): p. 8210-8213.

110. Krummel, A.T. and M.T. Zanni, *DNA Vibrational Coupling Revealed with Two-Dimensional Infrared Spectroscopy: Insight into Why Vibrational Spectroscopy Is Sensitive to DNA Structure.* The Journal of Physical Chemistry B, 2006. 110(28): p. 13991-14000.

111. Heyne, K., G.M. Krishnan, and O. Kühn, *Revealing Anharmonic Couplings and Energy Relaxation in DNA Oligomers by Ultrafast Infrared Spectroscopy.* The Journal of Physical Chemistry B, 2008. 112(26): p. 7909-7915.

112. Szyc, Ł., M. Yang, and T. Elsaesser, *Ultrafast Energy Exchange via Water-Phosphate Interactions in Hydrated DNA.* The Journal of Physical Chemistry B, 2010. 114(23): p. 7951-7957.

113. Szyc, Ł., et al., *Ultrafast Vibrational Dynamics and Local Interactions of Hydrated DNA.* Angewandte Chemie International Edition, 2010. 49(21): p. 3598-3610.

114. Tanaka, K. and Y. Okahata, *A DNA-Lipid Complex in Organic Media and Formation of an Aligned Cast Film1.* Journal of the American Chemical Society, 1996. 118(44): p. 10679-10683.

115. Yang, C., D. Moses, and A.J. Heeger, *Base-Pair Stacking in Oriented Films of DNA–Surfactant Complex.* Advanced Materials, 2003. 15(16): p. 1364-1367.

116. Yang, C.Y., et al., *DNA alignment and characterization.* Synthetic Metals, 2003. 137(1-3): p. 1459-1460.

117. Yetzbacher, M.K., et al., *Propagation, beam geometry, and detection distortions of peak shapes in two-dimensional Fourier transform spectra.* Journal of Chemical Physics, 2007. 126: p. 044511-30.

118. Leslie, A.G.W., et al., *Polymorphism of DNA double helices.* Journal of Molecular Biology, 1980. 143(1): p. 49-72.

119. Lipanov, A.A., D.B. Beglov, and V.P. Chuprina, *DNA B to D transition can be explained in terms of hydration economy of the minor groove atoms.* Journal of Molecular Biology, 1989. 210(2): p. 399-409.

120. Mazur, A.K., *Electrostatic Polymer Condensation and the A/B Polymorphism in DNA: 鈥?Sequence Effects.* Journal of Chemical Theory and Computation, 2005. 1(2): p. 325-336.

121. Bram, S. and P. Tougard, *Polymorphism of natural DNA.* Nature: New biology, 1972. 239(92): p. 128-31.

122. Pilet, J. and J. Brahms, *Investigation of DNA structural changes by infrared spectroscopy.* Biopolymers, 1973. 12(2): p. 387-403.

123. Taillandier, E., J. Liquier, and J.A. Taboury, *Advances in Infrared and Raman Spectroscopy*, ed. R.J.H. Clark and R. Hester. 1985, New York: John Wiley and Sons.

124. Plützer, C., et al., *Pairing of isolated nucleobases: Double resonance laser spectroscopy of adenine-thymine.* ChemPhysChem, 2003. 4(8): p. 838-842.

125. Wang, G.X., X.Y. Ma, and J.P. Wang, *Anharmonic Vibrational Signatures of DNA Bases and Watson–Crick Base Pairs* Chinese Journal of Chemical Physics, 2009. 22(6): p. 563-568.

126. Colarusso, P., et al., *The infrared spectra of uracil, thymine, and adenine in the gas phase.* Chemical Physics Letters, 1997. 269(1-2): p. 39-48.

127. Cringus, D., et al., *Ultrafast Energy Transfer in Water-AOT Reverse Micelles.* The Journal of Physical Chemistry B, 2007. 111(51): p. 14193-14207.

128. Tan, H.S., et al., *Dynamics of water confined on a nanometer length scale in reverse micelles: Ultrafast infrared vibrational echo spectroscopy.* Physical Review Letters, 2005. 94(5): p. 057405.

129. Cringus, D., et al., *Femtosecond water dynamics in reverse-micellar nanodroplets.* Chemical Physics Letters, 2005. 408(1-3): p. 162-168.

130. Urabe, H., et al., *Collective vibrational modes in molecular assembly of DNA and its application to biological systems. Low frequency Raman spectroscopy.* The Journal of Chemical Physics, 1985. 82(1): p. 531-535.

131. Kozich, V., J. Dreyer, and W. Werncke, *Mode-selective vibrational redistribution after spectrally selective N-H stretching mode excitation in intermolecular hydrogen bonds.* Journal of Chemical Physics, 2009. 130(3).

132. Kozich, V., et al., *Ultrafast redistribution of vibrational energy after excitation of NH stretching modes in DNA oligomers.* Chemical Physics Letters, 2009. 473(1-3): p. 171-175.

133. Khalil, M., N. Demirdöven, and A. Tokmakoff, *Vibrational coherence transfer characterized with Fourier-transform 2D IR spectroscopy.* Journal of Chemical Physics, 2004. 121(1): p. 362-373.

134. Jansen, T.l.C., et al., *Two-dimensional infrared spectroscopy and ultrafast anisotropy decay of water.* Journal of Chemical Physics, 2010. 132: p. 224503.

135. Cowan, M.L., et al., *Ultrafast memory loss and energy redistribution in the hydrogen bond network of liquid H2O.* Nature, 2005. 434(7030): p. 199-202.

136. Woutersen, S. and H.J. Bakker, *Resonant intermolecular transfer of vibrational energy in liquid water.* Nature, 1999. 402(6761): p. 507-509.

137. Deàk, J.C., et al., *Vibrational Energy Relaxation and Spectral Diffusion in Water and Deuterated Water.* The Journal of Physical Chemistry A, 2000. 104(21): p. 4866-4875.

138. Ashihara, S., et al., *Ultrafast Structural Dynamics of Water Induced by Dissipation of Vibrational Energy.* The Journal of Physical Chemistry A, 2007. 111(5): p. 743-746.

139. Ingrosso, F., et al., *Ultrafast Energy Transfer from the Intramolecular Bending Vibration to Librations in Liquid Water.* The Journal of Physical Chemistry A, 2009. 113(24): p. 6657-6665.

140. Rey, R., et al., *Pathways for H(2)O Bend Vibrational Relaxation in Liquid Water.* Journal of Physical Chemistry A, 2009. 113(31): p. 8949-8962.

141. Lock, A.J., S. Woutersen, and H.J. Bakker, *Ultrafast energy equilibration in hydrogen-bonded liquids.* Journal of Physical Chemistry A, 2001. 105(8): p. 1238-1243.

142. Rey, R., K.B. Møller, and J.T. Hynes, *Ultrafast vibrational population dynamics of water and related systems: A theoretical perspective.* Chemical Reviews, 2004. 104(4): p. 1915-1928.

143. Ashihara, S., et al., *Vibrational couplings and ultrafast relaxation of the O-H bending mode in liquid H2O.* Chemical Physics Letters, 2006. 424(1-3): p. 66-70.

144. Iwahashi, H. and Y. Kyogoku, *Direct proton exchange between complementary nucleic acid bases.* Nature, 1978. 271(5642): p. 277-278.

145. Choi, M.Y., F. Dong, and R.E. Miller, *Multiple tautomers of cytosine identified and characterized by infrared laser spectroscopy in helium nanodroplets: probing structure using vibrational transition moment angles.* Philosophical Transactions of the Royal Society of London Series a-Mathematical Physical and Engineering Sciences, 2005. 363(1827): p. 393-412.

146. Choi, M.Y. and R.E. Miller, *Four tautomers of isolated guanine from infrared laser spectroscopy in helium nanodroplets.* Journal of the American Chemical Society, 2006. 128(22): p. 7320-7328.

147. Choi, M.Y. and R.E. Miller, *Infrared Laser Spectroscopy of Uracil and Thymine in Helium Nanodroplets: Vibrational Transition Moment Angle Study.* The Journal of Physical Chemistry A, 2007. 111(13): p. 2475-2479.

148. Müller, A., F. Talbot, and S. Leutwyler, *S_1/S_2 exciton splitting in the (2-pyridone)$_2$ dimer.* Journal of Chemical Physics, 2002. 116(7): p. 2836-2847.

149. Müller, A., F. Talbot, and S. Leutwyler, *Hydrogen Bond Vibrations of 2-Aminopyridine;2-Pyridone, a Watson-Crick Analogue of Adenine-Uracil.* Journal of the American Chemical Society, 2002. 124(48): p. 14486-14494.

150. Schwalb, N.K., T. Michalak, and F. Temps, *Ultrashort Fluorescence Lifetimes of Hydrogen-Bonded Base Pairs of Guanosine and Cytidine in Solution.* Journal of Physical Chemistry B, 2009. 113(51): p. 16365-16376.

151. Schwalb, N.K. and F. Temps, *Base Sequence and Higher-Order Structure Induce the Complex Excited-State Dynamics in DNA.* Science, 2008. 322(5899): p. 243-245.

152. Yan, Y.-a. and O. Kuhn, *Geometric correlations and infrared spectrum of adenine-uracil hydrogen bonds in CDCl3 solution.* Physical Chemistry Chemical Physics. 12(48): p. 15695-15703.

153. Fonseca Guerra, C., et al., *Hydrogen Bonding in DNA Base Pairs: Reconciliation of Theory and Experiment.* Journal of the American Chemical Society, 2000. 122(17): p. 4117-4128.

154. Fonseca Guerra, C., T. van der Wijst, and F.M. Bickelhaupt, *Supramolecular Switches Based on the Guanine–Cytosine (GC) Watson–Crick Pair: Effect of Neutral and Ionic Substituents.* 2006. 12: p. 3032-3042.

155. Yagi, K., et al., *First-Principles Quantum Calculations on the Infrared Spectrum and Vibrational Dynamics of the Guanine-Cytosine Base Pair.* ChemPhysChem, 2009. 10(9-10): p. 1442-1444.

156. Yan, Y.-a. and O. Kühn, *Unraveling the Correlated Dynamics of the Double Hydrogen Bonds of Nucleic Acid Base Pairs in Solution.* The Journal of Physical Chemistry B, 2011. 115(18): p. 5254-5259.

157. Pecourt, J.-M.L., J. Peon, and B. Kohler, *Ultrafast Internal Conversion of Electronically Excited RNA and DNA Nucleosides in Water.* Journal of the American Chemical Society, 2000. 122(38): p. 9348-9349.

158. Pecourt, J.-M.L., J. Peon, and B. Kohler, *DNA Excited-State Dynamics:鈥?Ultrafast Internal Conversion and Vibrational Cooling in a Series of Nucleosides.* Journal of the American Chemical Society, 2001. 123(42): p. 10370-10378.

159. Peon, J. and A.H. Zewail, *DNA/RNA nucleotides and nucleosides: direct measurement of excited-state lifetimes by femtosecond fluorescence up-conversion.* Chemical Physics Letters, 2001. 348(3-4): p. 255-262.

160. Onidas, D., et al., *Fluorescence Properties of DNA Nucleosides and Nucleotides: A Refined Steady-State and Femtosecond Investigation.* The Journal of Physical Chemistry B, 2002. 106(43): p. 11367-11374.

161. Woutersen, S. and G. Cristalli, *Strong enhancement of vibrational relaxation by Watson-Crick base pairing.* Journal of Chemical Physics, 2004. 121(11): p. 5381-5386.

162. Nir, E., K. Kleinermanns, and M.S. de Vries, *Pairing of isolated nucleic-acid bases in the absence of the DNA backbone.* Nature, 2000. 408(6815): p. 949-951.

163. Nir, E., et al., *On the photochemistry of purine nucleobases.* Journal of Physical Chemistry A, 2001. 105(21): p. 5106-5110.

164. Nir, E., et al., *Properties of isolated DNA bases, base pairs and nucleosides examined by laser spectroscopy.* European Physical Journal D, 2002. 20(3): p. 317-329.

165. Abo-Riziq, A., et al., *Photochemical selectivity in guanine-cytosine base-pair structures.* Proceedings of the National Academy of Sciences of the United States of America, 2005. 102(1): p. 20-23.

166. Nir, E., et al., *Pairing of the nucleobases guanine and cytosine in the gas phase studied by IR-UV double-resonance spectroscopy and ab initio calculations.* Physical Chemistry Chemical Physics, 2002. 4(5): p. 732-739.

167. Hobza, P. and J. Šponer, *Structure, energetics, and dynamics of the nucleic acid base pairs: Nonempirical ab initio calculations.* Chemical Reviews, 1999. 99(11): p. 3247-3276.

168. Yang, M., et al., *The Hydrogen-Bonded 2-Pyridone Dimer Model System. 2. Femtosecond Mid-Infrared Pump-Probe Study.* Journal of Physcial Chemistry A, 2010. 114(46): p. 12195–12201.

169. Szyc, Ł., et al., *The Hydrogen-Bonded 2-Pyridone Dimer Model System. 1. Combined NMR and FT-IR Spectroscopy Study.* The Journal of Physical Chemistry A, 2010. 114(29): p. 7749-7760.

170. Dwyer, J.R., et al., *Ultrafast dynamics of vibrational N-H stretching excitations in the 7-azaindole dimer.* Chemical Physics Letters, 2006. 432(1-3): p. 146-151.

171. Heyne, K., et al., *Coherent low-frequency motions of hydrogen bonded acetic acid dimers in the liquid phase.* Journal of Chemical Physics, 2004. 121(2): p. 902-913.

172. Mons, M., et al., *Tautomerism of the DNA Base Guanine and Its Methylated Derivatives as Studied by Gas-Phase Infrared and Ultraviolet Spectroscopy.* The Journal of Physical Chemistry A, 2002. 106(20): p. 5088-5094.

173. Bakker, J.M., et al., *The mid-IR absorption spectrum of gas-phase clusters of the nucleobases guanine and cytosine.* Physical Chemistry Chemical Physics, 2004. 6(10): p. 2810-2815.

174. van der Wijst, T., et al., *Performance of various density functionals for the hydrogen bonds in DNA base pairs.* Chemical Physics Letters, 2006. 426(4-6): p. 415-421.

175. Nachtigallova, D., P. Hobza, and V. Spirko, *Assigning the NH Stretches of the Guanine Tautomers Using Adiabatic Separation: CCSD(T) Benchmark Calculations.* The Journal of Physical Chemistry A, 2008. 112(9): p. 1854-1856.

176. Fidder, H., J. Knoester, and D.A. Wiersma, *Optical properties of disordered molecular aggregates: A numerical study.* The Journal of Chemical Physics, 1991. 95(11): p. 7880-7890.

177. Iogansen, A.V., *Direct proportionality of the hydrogen bonding energy and the intensification of the stretching υ(XH) vibration in infrared spectra.* Spectrochimica Acta Part A: Molecular and Biomolecular Spectroscopy, 1999. 55(7-8): p. 1585-1612.

178. Spencer, J.N., et al., *The nitrogen-hydrogen bond. 2. Models for nucleic acid bases.* The Journal of Physical Chemistry, 1979. 83(20): p. 2615-2621.

179. Nienhuys, H.-K., et al., *Mechanism for vibrational relaxation in water investigated by femtosecond infrared spectroscopy.* The Journal of Chemical Physics, 1999. 111(4): p. 1494-1500.

180. Rey, R., K.B. Møller, and J.T. Hynes, *Ultrafast Vibrational Population Dynamics of Water and Related Systems:A Theoretical Perspective.* Chemical Reviews, 2004. 104(4): p. 1915-1928.

Acknowledgement

It was my good fortune having an opportunity to spend years in Max-Born-Institut für Nichtlineare Optik und Kurzzeitspektroskopie as a PhD student. Here I have learned the novel optical techniques in the cutting edge field, and used it to explore the fascinating unknown world. I also met many nice people helping me in my work and life. Hereby, I wish to thank them all.

First, I would like to thank Prof. Dr. Thomas Elsässer for he generously offered me this opportunity. During numerous discussions and email exchanging with him in these years, I have learned a lot from him about how to understand experimental data and to interpret them with mechanisms behind in a deep level. Without his help, I would never finish this thesis. Moreover, his kindly advices and help about my future are greatly appreciated.

I also want to express many thanks to the two Dutch in our group, Dr. Erik T.J. Nibbering and Dr. Henk Fidder, for their broad knowledge and patience. Their understandings of theory and experiment helped me to solve many scientific questions, especially during the time when Henk shared the office with me. They also exposed me to the wide European culture and history and opened my eyes to a broad range of interesting knowledge.

In the lab, it was really nice having Dr. Lukasz Syzc and René Costard accompanying. Through uncounted discussions with them, I have learned a lot of chemistry and enlightened by many brilliant ideas from them. Prof. Dr. Nils Huse helped a lot as well, although he is away from our institute. Without hours of telephone call and tens of emails exchanged with him, I would have to spend much more time to make the 2D experiment run.

I feel lucky to meet and work with Dr. Katrin Admaczyk, Mirabella Prémont-Schwarz, Prof. Jason Dwyer, Christian Greve and Dr. Jens Dreyer for their friendliness and valuable discussions.

Many thanks to the staff of the insitute, who has contributed to the nice atmosphere here and helped me with my experiment. Frau Regina Goleschny, Frau Brigitte Steinert and Frau Regina Lendt supported me in the chemistry lab, Herr Peter Scholze supported in the mechanics shop and Helmut Walz did a lot of work with computers and electronics.

I am grateful to Frau Margaret Lehmann and Frau Alexandra Wettstein for their kindly help in sloving numerous problems in many aspects.

At last but not the least, I would offer my special thanks to my mum, my uncle and his family who treats me as an member of them, my brother and his family, and my wife and my daughter, for their supports all the time. I owe them much more than I can pay.